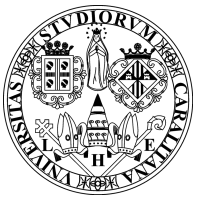

Università degli Studi di Cagliari

DOTTORATO DI RICERCA
IN INGEGNERIA DEL TERRITORIO
Ciclo XXV

Seismic Reflection Imaging of Near Surface Structures Using the Common Reflection Surface (CRS) Stack Method

Settore scientifico disciplinare di afferenza:
GEO/11 Geofisica Applicata

Presentata da: Dott. Enzo Battaglia

Coordinatore Dottorato: Prof. Roberto Deidda

Tutor/Relatore: Prof. Gian Piero Deidda

Esame finale anno accademico 2012-2013

Abstract

This PhD thesis aims to evaluate whether the Common-Reflection-Surface (CRS) stack method can be considered as a more cost efficient processing alternative to the conventionally used Common Midpoint (CMP) stack method for processing of shallow and ultrashallow reflection data.

The CRS stack is a seismic imaging method established for oil and gas exploration that is similar in concept to the conventional CMP stack method. Unlike the CMP stack, the CRS stack process is not confined to single CMP gathers (offset direction), but also includes neighbouring CMPs (midpoint direction) into the so-called CRS supergathers. The use of CRS supergathers enables stable "data-driven", i.e. without human interactions, velocity analysis and residual static corrections, avoiding the poorly-automated and time-consuming processing steps that are instead required when implementing conventional CMP processing. This makes the seismic imaging process more compatible with budgets available for near-surface geophysical investigations. Improving seismic imaging of near-surface reflection data, while at the same time reducing processing costs and human interaction during processing was the principal objective which guided my work.

To investigate the advantages and limitations of exporting the CRS stack from the hydrocarbon exploration field to the near-surface scale, I have firstly analysed and adapted the characteristics of the CRS to the requirements of near-surface reflection data. Then, I have compared the results (seismic sections and velocity fields) obtained by processing with the CMP and the CRS stack methods for two real field datasets (P- and SH-wave) and two synthetic datasets that exhibited very large vertical velocity changes. Finally, I have proposed some original solutions that overcome several of the issues encountered when using CRS stack with near-surface data.

The P-wave dataset was collected as part of a hydrogeological investigation with the aim of delineating the hydrogeological framework of a paleolake environment to a depth of few hundred metres. Using the CMP method, several nearly horizontal reflectors with onsets from 60 to about 250 ms were imaged. The CRS stack produced a stacked section with greater coherency and lateral continuity than the CMP section, but also spurious alignments of seismic energy which hinder interpretation. Weighing the CRS stacked section with the corresponding CRS coherence and number of CRS stacked traces leads to a considerable reduction of the spurious alignments, resulting in a seismic section more suited to delineate the aquifer and its confining units.

The SH-wave ultrashallow dataset was collected to support a geotechnical study to a depth of 10 m. The obtained CMP stacked section imaged a dipping bedrock interface below four horizontal reflectors in unconsolidated, very low velocity sediments. The vertical and lateral resolution was very high, so that despite the very shallow depth the resulting CMP stacked section showed the well-defined pinchout of two layers at less than 10 m depth. The CRS stack improved the continuity of the shallowest reflector but showed an excessive smearing effect with some reflector portions, including the pinchout, unresolved and not as well defined as in the (very detailed) CMP counterpart. Restricting the CRS stack process to single CMP gathers, preserving the CRS-supergather for

the search of stacking parameters, produced a time section very similar to the CMP counterpart.

In both cases, I swiftly obtained the CRS stacked sections in a fully automatic way, so with a cost/benefit ratio considerably more advantageous than that of the CMP sections, which required time-consuming prestack velocity analysis as well as residual static corrections. Moreover, using the kinematic wavefield attributes determined for each stacking operation I reconstructed velocity fields matching the ones estimated with the CMP processing, even if this required a greater amount of work than that required to produce the CRS stacked sections.

Finally, using two synthetic datasets, I addressed the issue of the crossing reflection events that appear in data acquired in soils characterized by strong vertical velocity gradients. Although a matter debate for decades, this is an issue still unresolved by use of the conventional CMP method. Using the first synthetic dataset I showed that unlike in conventional CMP processing which cannot accurately process crossing reflection events without generating distortions and artefacts, the data-driven CRS stack imaging process considerably restricts their generation, limiting the reduction of signal-to-noise ratio and of temporal resolution in stacked traces. With the second synthetic dataset I simulated a data acquisition reproducing a case history with a high-velocity contrast in the first 5 m depth. The CRS results that I obtained from the modelled data demonstrated that the CRS stack method may be a reliable alternative for processing crossing reflection events, definitely easier and faster than the construction of complicated velocity functions and/or the separated processing of the crossing events. By comparing these results with those obtained using the CMP method I obtained other interesting results, which, however, to validate would necessitate the use of real datasets.

The findings of this present study demonstrates that the CRS stack could represent a significant step forward for the reduction of the costs involved in shallow and ultrashallow seismic reflection data processing, one which does not compromise the quality of results. Both these conditions being essential to the increased acceptance of the seismic reflection method as a routine investigation method for use in shallow and ultrashallow seismics.

Keywords = 2D seismic imaging, near-surface, data-diven methods, P-wave, shear wave (SH-wave), intersecting reflections.

Sommario

Questa tesi di dottorato valuta se l'impiego del metodo di elaborazione denominato Common Reflection Surface (CRS) stack può essere un'alternativa più conveniente rispetto al convenzionale Common Midpoint (CMP) stack per l'elaborazione dei dati di sismica a riflessione superficiale ed ultra-superficiale.

Il CRS stack è un processo di imaging sismico sviluppato per le indagini di esplorazione petrolifera, concettualmente simile al convenzionale metodo del CMP stack. Tuttavia, a differenza del CMP, il CRS stack non agisce su una singola famiglia CMP (direzione offset), ma si estende anche alle famiglie CMP vicine (direzione midpoint), l'insieme delle quali costituisce la cosiddetta CRS supergather. L'uso della CRS supergathers permette di eseguire l'analisi di velocità e le correzioni statiche residue in modo accurato e del tutto automatico, evitando così i lunghi e laboriosi processi di elaborazione che sono invece richiesti nell'elaborazione CMP. Ciò rende il processo di imaging sismico compatibile con i budget disponibili per la geofisica negli ambiti delle indagini superficiali. Migliorare la qualità dei risultati, riducendo i costi di lavorazione e l'interazione umana durante la lavorazione è stato l'obiettivo generale del mio lavoro.

Per valutare i vantaggi e i limiti dell'esportare il CRS dal campo esplorativo alla scala delle indagini superficiali, in primo luogo ho analizzato e adattato le caratteristiche del CRS ai requisiti della sismica a riflessione superficiale. Successivamente, ho confrontato i risultati (sezioni sismiche e campi di velocità) ottenuti elaborando con il CMP e con il CRS due set di dati sperimentali (uno per onde P l'altro per onde SH) e due set di dati sintetici con forti variazioni verticali di velocità, e ho proposto soluzioni originali per superare alcune delle difficoltà emerse nell'impiego del CRS per l'elaborazione dei dati di sismica a riflessione superficiale.

Il data set per onde P è stato acquisito nell'ambito di un'indagine idrogeologica con lo scopo di migliorare le conoscenze delle strutture idrogeologiche fino alla profondità di alcune centinaia di metri. Utilizzando il metodo CMP, ho ottenuto una sezione sismica con vari riflettori pressoché orizzontali con tempi di arrivo compresi tra 60 e 250 ms circa. Con il metodo CRS ho ricavato una sezione sismica con maggiore coerenza e continuità laterale rispetto alla sezione CMP, ma anche con alcuni falsi allineamenti di energia sismica che ostacolano l'interpretazione della sezione sismica. Pesando la sezione CRS con i valori di coerenza e con il numero di tracce utilizzate dal CRS ho ottenuto una sezione sismica con una notevole riduzione dei falsi allineamenti, e quindi più adatta per delineare le strutture idrogeologiche dell'acquifero.

Il data set per onde SH, invece, è stato acquisito con l'obiettivo di caratterizzare dal punto di vista geotecnico i primi 10 m di terreno. La sezione sismica CMP mostra un basamento roccioso inclinato, e al di sopra un deposito di sedimenti in cui si distinguono quattro riflettori orizzontali con velocità sismiche molto basse. Le risoluzioni laterale e verticale sono elevatissime, e nonostante la bassa profondità si distinguono chiaramente due strati sedimentari che si appoggiano sul basamento roccioso. L'elaborazione CRS ha migliorato la continuità del riflettore più superficiale, ma ha prodotto anche un'eccessiva levigatura della sezione sismica con alcune porzioni di riflettori, compreso l'appoggio dei

due strati sedimentari sul basamento roccioso, non ben definiti come nella sezione CMP. Limitando lo stack CRS alle singole famiglie di CMP, ma preservando l'uso della CRS supergather per la ricerca dei parametri di stack, ho ottenuto, invece, una sezione sismica molto simile a quella (estremamente dettagliata) del CMP.

In entrambi i casi, con il CRS ho rapidamente ottenuto le sezioni sismiche in modo completamente automatico, e quindi con un rapporto costi/benefici vantaggioso rispetto a quello del metodo CMP che invece ha richiesto laboriose e lunghe analisi di velocità e correzioni statiche residue. Inoltre, utilizzando i parametri cinematici del campo d'onda valutati durante il processo di CRS stack, ho ricostruito campi di velocità sismiche simili a quelli stimati con l'elaborazione CMP, anche se con più fatica rispetto a quella necessaria per produrre le sezioni sismiche.

Con i due set di dati sintetici, infine, ho affrontato il problema delle iperboli di riflessione incrociate che compaiono nei dati acquisti in terreni caratterizzati da forti gradienti verticali di velocità. Si tratta di un problema dibattuto da decenni e ancora non completamente risolto. Con il primo set di dati sintetici ho documentato che a differenza del convenzionale CMP, che non può elaborare accuratamente le iperboli di riflessione incrociate senza generare distorsioni e artefatti, l'implementazione "data-driven" del CRS limita fortemente la loro generazione, e quindi la riduzione del rapporto segnale/rumore e della risoluzione temporale nelle tracce stack. Con il secondo set di dati sintetici ho simulato un'acquisizione che riproduce un caso di studio con forti gradienti di velocità verticali nei primi 5 metri di profondità. La sezione CRS che ho ottenuto dai dati modellati dimostra che il CRS stack può essere una valida opzione per risolvere il problema delle riflessioni incrociate, decisamente più facile e più rapida da implementare rispetto alla costruzione di complicate funzioni di velocità e/o all'elaborazione separata delle riflessioni incrociate. Dal confronto di questi risultati con quelli ottenuti con il CMP, sono emersi altri interessanti risultati, che tuttavia sarebbe opportune validare con set di dati sperimentali.

I risultati del presente studio dimostrano che il CRS stack può essere un significativo passo in avanti per ridurre i costi di elaborazione dei dati di sismica a riflessione superficiale ed ultrasuperficiale senza compromettere la qualità dei risultati. Il raggiungimento di entrambe queste condizioni è necessario per far diventare la sismica a riflessione una tecnica di routine anche nelle indagini sismiche superficiali.

Parole chiave = 2D imaging, near-surface, metodi data-diven, onde P, onde di taglio (onde SH), riflessioni incrociate.

Acknowledgements

I would like thank to all those who have helped me during these intensive years, both in the academic and personal environment.

My sincere gratitude goes to my advisor **Prof. Gian Piero Deidda** for his guidance, support and encouragement given throughout these years. Thank you for teaching me a critical and pragmatic approach to scientific research.

Thanks to **Prof. Gaetano Ranieri** for the opportunity of this doctoral research.

Thanks to **Prof. Dirk Gajewski** for the opportunity to study in the Institute of Geophysics at the University of Hamburg, which I really enjoy.

Many thanks to **Dr. Zeno Heilmann** for his help during the accomplishment of my project. He always gave me support and useful tips on various research problems.

Thanks to **Prof. Ranajit Ghose** Professor in Applied Geophysics at the Department of Geoscience and Engineering of the Delft University, **Prof. Stéphane Garambois** Professor at the Institut des Sciences de la Terre of the Joseph Fourier University of Grenoble and **Dr. Mahjoub Himi** of the Departament de Geoquímica, Petrologia i Prospecció Geològica at the University of Barcelona for their critical, accurate, and constructive remarks which helped to improve this thesis.

Thanks to the **Imaging and Numerical Geophysics group of CRS4** for the research training period during which I felt like at home.

Thanks to the **Wave Inversion Technology (WIT) consortium** for providing the codes for CRS processing.

Most of all I thank for the her patience and support my partner, **Maria Domenica**.

Contents

Chapter 1

Introduction

1.1 Motivation and general objectives

Detailed information concerning the near-surface geology is necessary to address a wide variety of engineering and environmental issues. A traditional approach implies the use information extrapolated from boreholes and outcrops which however has the main drawback of often being insufficient in providing a comprehensive analysis of the geological subsurface structures and their properties. A more comprehensive approach instead can be obtained using geophysical techniques. These include a variety of electrical, electromagnetic and seismic methods. Over the past 30 years these techniques have become an increasingly key component in many non-invasive investigations including estimating soil stiffness, mapping layer geometries, interpreting lithologies and in measuring material proprieties. Nowadays, besides traditional applications such as groundwater investigations, natural-hazard mitigation and mining, the field of the near-surface geophysics, once referred to as "environmental and engineering geophysics", has broadened out to include other applications as polluted site management, precision-agriculture and archaeological prospecting. Numerous special sections published in relevant geophysical journals document this trend [see e.g. First Break, 2011; Geophysics, 1998; Near Surface Geophysics, 2009; The Leading Edge, 2009, 2011, 2012, 2013].

This thesis focuses on the shallow seismic reflection method, which is a geophysical method based on the propagation of elastic waves into the ground. Compared to other near-surface seismic techniques such as refraction or surface wave methods, the shallow reflection method offers higher spatial resolution and better imaging ability. It is therefore the preferable option in engineering and environmental applications that are required to detect small-scale features at shallow depths. In these cases, ground-penetrating radar (GPR) is probably the most reliable non-destructive tool. Near-surface materials however often exhibit physical properties (e.g. high electrical conductivity) that can severely restrict its depth of penetration. When this occurs, the ultrashallow seismic reflection tool could be a viable high-resolution imaging alternative. In any case, even when GPR works well, seismic and electromagnetic imaging together can provide an additional degree of constraint to the resulting model of the subsurface.

Over the last decades the use of shallow seismic reflection method has became fairly commonplace in the geosciences community. This is evident from the large number of successful applications in the imaging of near-surface structures, from a few meters to a few hundred meters depth. Both P- and S-wave (usually SH-wave) reflection methods have proven useful in many engineering, geotechnical, environmental, and hydrogeological studies [see e.g. Benjumea et al., 2003; Bradford et al., 2006; Ghose et al., 1998; Goforth and Hayward, 1992; Guy et al., 2003; Liberty, 1998; Pugin et al., 2009; Woorely et al., 1993]. Nonetheless, up until now engineers, hydrogeologists and geotechnicians still have not considered them as a viable tool for near-surface investigations, but have preferred to use borehole drilling or other geophysical techniques such as seismic refraction and surface wave methods, or electrical resistivity and electromagnetic methods. Compared to the reflection method these generally involve lower costs for acquisition and data processing which when considering budgets of typical near-surface investigations, are requisites that make them generally preferred in the commercial communities even at the expense of the quality of the results. This is why at present the general research trends regarding shallow seismic reflection methods are aimed at the possibility of developing acquisition and data processing strategies that acquire large volume of high-quality near-surface reflection data over a short time and at reduced costs. Any improvement in this direction will definitely boost the success and spread of shallow seismic reflection methods in the engineering and environmental contexts.

To decrease costs of seismic reflection data acquisition without reducing the quality of the survey it is essential to acquire high-fold coverage data in fast and efficient ways. Acquiring high-fold data is always advantageous because it allows improvement in the trace-to-trace coherency and the S/N ratios of seismic sections, avoiding spatial aliasing and enabling the retrieval of more accurate and stable velocity information [e.g. Lanz et al., 1996; Steeples and Miller, 1998]. This however requires performing numerous closely spaced shots with hundreds of receivers densely spaced which inevitably, result in increased survey costs. Seismic recording systems which have from hundreds to up tens of hundreds of channels (see Figure 1.1a), which enable rapid area coverage and the collection of large data volume (true 3D data acquisition), are currently available for near-surface geophysics at relatively low costs and there is no doubt that this trend will continue to grow (see Figure 1.1b). However, the planting by hand of a high number of geophones, their connection to the cable takeouts, the picking up and moving back and forth of geophones and cables between many closely spaced positions are still laborious and very time-consuming procedures that exponentially increase the logistical complexity of the survey and consequently costs. Data-acquisition rate, data-quality and consequently data-acquisition costs are also highly dependent on the type of seismic source used. Ideally this should ensure adequate depth of penetration of seismic energy, efficiency, high reproducibility, safety and cost-effectiveness [e.g. Miller et al., 1994; van der Veen et al., 2000]. Recently, technological advancements in survey instrumentation offer the possibility of acquiring with high acquisition rates and reduced costs large volumes of data, either P- or SH-wave, that are densely spaced.

Van der Veen and Green [1998] and van der Veen et al. [2001] proposed acquiring seismic data using a land-streamer, namely a short array (mostly less than 200 meters) of gimballed geophones fixed on sleds or within a high-strength sleeve that allows the acquisition of reflection data without the need of planting the geophones into the ground

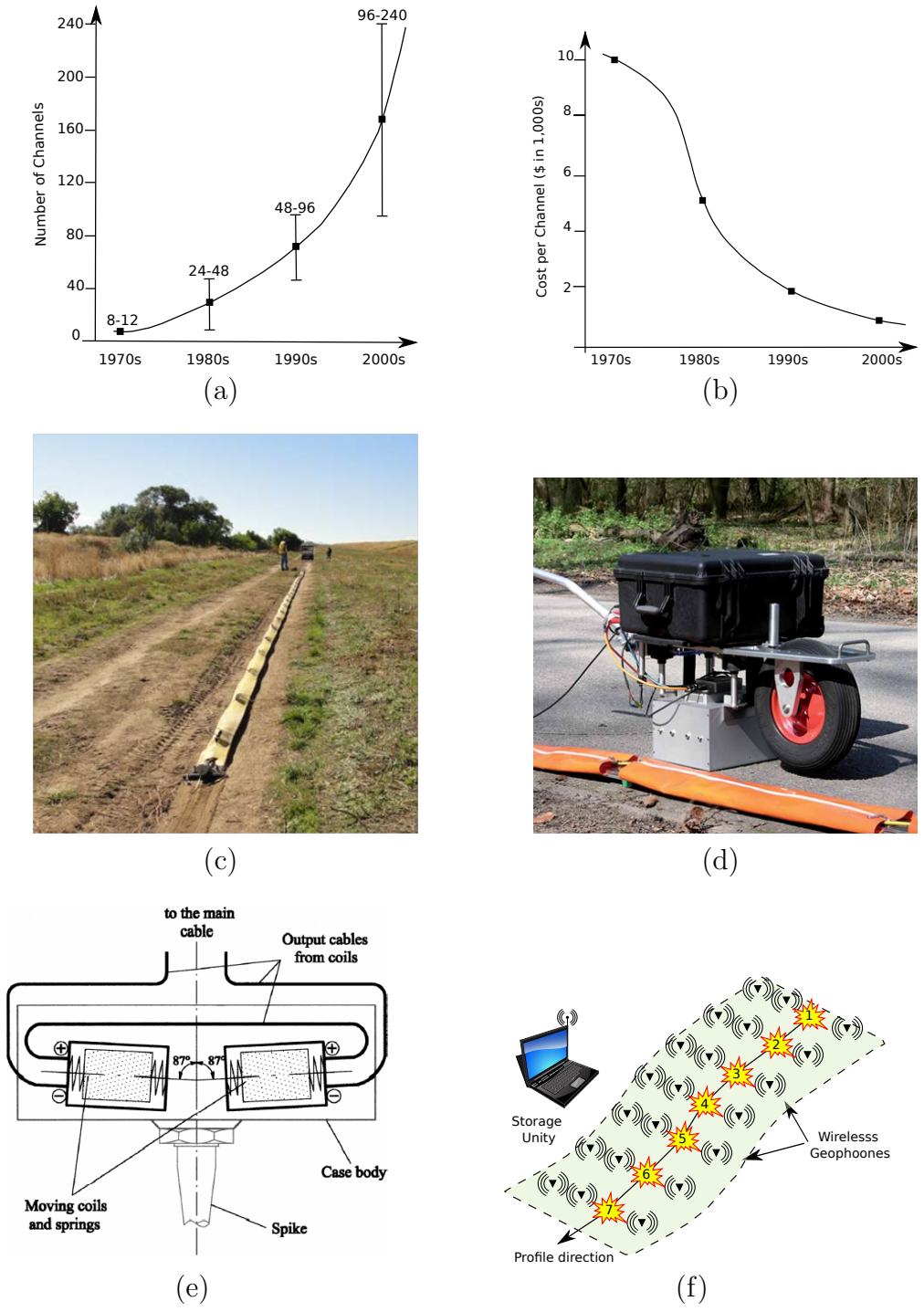

Figure 1.1: Technological advancements in acquisition equipments. (a) Typical number of recording channels on engineering seismographs as a function of decade of manufacture, from Steeples and Miller [2007]; (b) cost per recording channel for engineering seismographs since about 1970 (no effects of inflation were added) from Steeples and Miller [2007]; (c) land streamer; (d) Electro-dynamic Vibrator System (Elvis) patent from the Geomatrix for generation of P or S wave; (e) Schematic of the special horizontal velocity detector described by Sambuelli et al. [2001]; (f) sketch of a "cable-less geophones network".

and of connecting them to the cables (see Figure 1.1c). Towing the land-streamer between many shortly spaced shot positions offers the possibility of acquiring a large quantity of densely spaced data in efficient and easy way, similar to what is done in marine surveys where special vessels tow a large number of receivers connected by cables (marine-streamers). Performing several tests on different recording environments such as meadows, asphalt roads and gravel tracks, the authors showed that they were able to collect shallow and ultrashallow P-wave data of a quality similar to those acquired with traditional spiked geophones, but at faster rates, with fewer field personnel and consequently reduced costs. They also showed that by towing the land-streamer along the survey line with a vehicle, they were able to increase the acquisition speed by a factor of between 50-100%, while reducing the field personnel by 30-40%. New streamer technologies have proven to be efficient tools when recording SH-wave reflection data [Inazaki, 1999, 2004; Kurahashi and Inazaki, 2006; Pugin et al., 2007, 2004, 2006], and in three-dimensional (3D) shallow seismic reflection surveys [Dolena et al., 2008].

Steeples et al. [1999] and Schmeissner et al. [2001] built and field-tested a hydraulic device able to plant in automatic and rapid way 72 closely spaced geophones (15 cm intervals), maintaining a good coupling with the ground and without significant loss in data quality. They proved that in many recording environments this device substantially decreases the time and costs of data acquisition, especially when the use of closely-spaced geophones is required.

Ghose et al. [1998], Haines [2006] and Polom et al. [2010] have developed highly portable and relatively inexpensive vibratory sources specifically designed for shallow and ultra-shallow seismic reflection surveys (e.g. see Figure 1.1d). These generate vertical and horizontal controlled pulse and sweep signals at high repetition rates over a broad range of frequencies (up to 600 Hz) with sufficient energy to provide adequate depth penetration and high signal-to-noise (S/N) ratios in many noisy recording conditions (e.g. wind, traffic, etc.). Compared to impulsive sources such as sledgehammer, shotgun, explosive or weight drops, the vibrating sources also avoid traditional drawbacks, such as limited bandwidth, insufficient high-frequency energy (i.e. poor resolution), cumbersome field logistics, source-generated noise and heavy physical efforts.

Sambuelli et al. [2001] developed and tested special horizontal receivers specifically designed for shallow and ultrashallow SH-wave reflection surveys (see Figure 1.1e). In near-surface surveys these waves are mostly generated using an impact source like a sledgehammer that hits, in two opposite directions perpendicular to the survey line, the sides of an object coupled with the ground by spikes or a large mass. The resulting two records are then subtracted to remove the unavoidable P- and SV-wave contaminations and enhance only SH-wave reflections [Hasbrouck, 1991; Helbig, 1987]. This commonly used procedure requires similarity between each pair of opposite shots, and consequently entails additional processing steps as adjusting amplitudes (rescaling) and removing time-break variations (determined by cross-correlation) before the trace-to-trace subtraction taking place [e.g. McCormack and Tatham, 1986]. The special horizontal receiver described in Sambuelli et al. [2001] detects horizontal movements better than standard horizontal geophones and requires only one shot for each source position. Consequently, extra processing steps are avoided and acquisition of SH-wave reflection data is no more complicated than normal P-wave data acquisition.

Looking towards the future, new ideas that are coming onto the marketplace will further reduce the cost and field work now needed in the acquisition of near-surface reflection data. For example, in recent years in hydrocarbon industry there have been significant advances in the use of wireless, i.e. cable-less, land-acquisition systems [see e.g. Brice and Deere, 2008, and references therein]. As these systems will become commercially available at relatively low cost it is likely that the use of "cable-less geophones network"(see Figure 1.1f) will become routine also in the field of the near-surface investigations. These, high-portability acquisition systems will allow the acquisition of densely spaced data by simply moving the seismic source along the line (or around the surveyed area for 3D acquisitions), greatly reducing survey time and so cost.

Thus it seems reasonable to conclude that these new acquisition systems will be increasingly used in the future. This will result in the possibility of acquiring large amounts of data at lower cost. For example using a Minivib/land-streamer acquisition system Pugin et al. [2009] showed that they routinely acquire P- and S-wave data from around 1000 shot-point/day, gaining production rates from two to ten times the rates usually expected using traditional spiked geophones and sources.

Unfortunately, the success of shallow seismic reflection surveys greatly depends on the processing, and in particular on the detail with which velocity analysis and residual static corrections are carried out. The reason mainly lies in unpredictable vertical and horizontal changes over small distances induced by the high degree of heterogeneity of the near-surface materials. In the near surface, seismic velocities have large and sometimes unexpected variations; e.g., they may change from as low as 100 m/s [e.g. Bachrach et al., 1998; Bachrach and Nur, 1998] to more than 2000 m/s within only few meters both in vertical and/or horizontal directions. Large vertical velocity gradients most often occur at the transition between unsaturated/saturated sediments, or at the interface between bedrock and overlying sediments. Large lateral velocity variations may instead be caused by lithology, porosity, water content variations, thin layers of higher (lower) velocities, different moisture conditions or anomalous compaction [see e.g. Jefferson et al., 1998; Robertsson et al., 1996b]. Such pronounced velocity variations, uncommon at the typical depths of conventional seismic reflection surveys, lead to complex reflection traveltime distortions [Marsden, 1993a,b], large time shifts, phase wavelets variations with offset and intersection of reflection traveltimes [Miller and Xia, 1998]. Consequently, laborious and time-consuming velocity analysis and residual static corrections are necessary, which inevitably increase the complexity of data processing and thus its costs. These may amount to double the costs of data acquisition itself. In such cases, picking stacking velocity values from few a selected CMP gathers as well as the use of residual static correction routines alone, are unable or insufficient to obtain detailed CMP stacked sections correctly interpretable from both structural and stratigraphic point of view. Most often the required velocity information and residual static corrections must be carefully derived CMP-by-CMP with a high quality control.

In areas with rapid lateral and vertical velocity changes prestack depth migration (PSDM) may be considered a valuable option to the conventional CMP stack method to achieve successful seismic imaging [see e.g. Bradford et al., 2006; Bradford and Sawyer, 2002; Bruno et al., 2010; Pasasa et al., 1998]. However, whatever the imaging procedure

used, the stacking velocities and residual static corrections must always be determined with extraordinary emphasis to obtain good stacked sections.

Theoretically, as with exploration data, this could be done automatically by setting appropriate parameters in conventionally used processing routines. In practice although the physical principles are the same irrespective of the depth of investigations, for near-surface reflection data, standard automatic procedures generally produces very poor and unsatisfactory results. In general the relative importance of some near-surface aspects require something more than just a simple scaling down of the techniques and processing procedures developed for the exploration field.

It is a matter of fact, that to image geological structures at the depth of several kilometres, the typical two-way traveltimes (twt) for compressional P-waves reflecting from a horizon of interest, generally half a second or more, is usually enough to separate the reflection event from other propagating waveforms as guided waves or ground roll (Rayleigh waves). Conversely, in shallow and ultrashallow seismic reflection data these and other events, such as refracted waves, air wave and air-coupled waves arrive at about the same twt as the weaker shallow reflections, interfere with and break down the trace-to-trace continuity of the reflections. Additionally, in near-surface surveys erratic blocks and boulders often have dimensions comparable to that of the dominant periods of the seismic signal and they can act as source of diffracted and scattered waves leading to an increase of coherent noise [e.g. Robertsson et al., 1996a]. Moreover, compared to deeper surveys near-surface investigations target materials with high-attenuation proprieties, which may induce abrupt inelastic attenuations and/or unexpected amplitude changes. Finally near-surface acquisitions must frequently respect economical limitations that dictate use of instrumentation and acquisition strategies which are less than ideal. Typically these may give rise to low fold data, poor S/N ratios, spatially aliased ground roll and/or shot-receiver spacing insufficient to determine optimal stacking velocities values from CMP reflections curvatures.

Under the above mentioned conditions, the automatic implementation of conventional velocity analysis and residual static corrections algorithms tends to fail because they are less robust against noise interference. For example, the semblance measure of Taner and Koehler [1969], conventionally used in velocity spectra algorithms, does not take into account amplitude variations with offset. As a result this might be expected to perform poorly in events with strong wavelet changes and/or with polarity reversals. Likewise, the statistical correlation routines which automatically try to compensate for small time shifts by improving the coherence of the existing reflections, are only reliable on data with a fairly high S/N ratio, otherwise their application may generate coherent artefacts leading to stacked sections without any correlation to the real subsurface structure. An efficient way to support the processing algorithms may be improving the S/N ratio of records by stacking two or more adjacent CMP gathers. However, this doesn't take into account any possible structural complexity of reflectors (i.e. dipping reflectors in faulting areas) neither any possible time shifts and therefore may lead to less than optimal stacking results. Neither the dip moveout (DMO) correction [e.g. Deregowski, 1986] nor residual static corrections would provide specific benefits as both must be applied to CMP gathers NMO-corrected with a previously determined velocity model. On the other hand, multichannel processing procedures like band-pass filtering or gain functions

do not remove refractions, ground roll, or air waves but merely suppress some of their characteristics as apparent velocities and frequency contents. Therefore, since these often are the same as the reflected events, they are frequently ineffective in enhancing the reflection signals at the expense of source-generated noises.

Due to all these processing related difficulties, the operator must identify and progressively refine by hand, CMP-per-CMP, the stacking velocities and residual static corrections that produce the best stack response. Additionally, since traditional NMO-correction techniques in the processing of near-surface seismic reflection data can produce detrimental stretch-related artefacts, the operator has to choose the percentages of allowable stretch mute which best represents the compromise among spectra integrity and S/N ratio. In doing this, he must rely on his intuition using a"trial-and-error" approach which although capable of producing excellent results, is usually very time-consuming and consequently involves high processing costs. For shallow and ultra-shallow seismic reflection data all these processing steps are usually poor automated, time-consuming and costly. Accordingly any processing strategy able to make velocity analysis, residual static and NMO corrections faster, more accurate and less user interactive would greatly reduce the costs of processing shallow and ultrashallow seismic reflection data.

To help fulfil this need I analyse and discuss a possible solution to these processing-related difficulties, namely replacing the conventional Common Midpoint (CMP) stack method [Mayne, 1962] with the Common-Reflection-Surface (CRS) stack method [e.g. Jäger et al., 2001; Mann et al., 1999]. During the last decade the CRS stack has established itself as a new and promising approach for time domain imaging in oil and gas exploration. This method is based on a generalized velocity analysis and stacking procedure that, unlike the NMO/DMO method which is based on planar or dipping reflector segments, assumes reflector-segments of arbitrary curvature, including diffraction points and planar reflectors [Hertweck et al., 2007]. This implies a stacking process which is not confined to single CMP gathers (offset direction) as the classical CMP stack method, but one that included neighbouring CMPs (midpoint direction) to form a so-called CRS supergather. Such supergather covers all traces that contain energy reflected from a certain common-reflector-segment in depth, centred on the theoretical reflection point of the zero-offset ray, i.e. the ray with normal incidence angle. The corresponding CRS spatial stacking operator is a time-offset-midpoint surface which allows for a more stable data-driven imaging process for targets such as flat-layered or steeply dipping reflectors, diffractors and fault as well as higher levels of noise and the use of sparser surveys without loss in imaging quality [Gierse et al., 2009]. Additionally, since the CRS stack imaging process needs only minimal a-priori information concerning the unknown velocity model, it avoids the conventional velocity analysis and related artefacts, so it is therefore faster, less user-interactive and, consequently, more cost-efficient then the conventional CMP stack method. Moreover, the CRS stacking parameters or kinematic wavefield attributes which are automatically determined through coherence (semblance) analysis for the stacking of prestack data can be used to derive surface-consistent residual static corrections as well as retrieving stacking velocity information. All these without the need of performing the traditional CMP-based stacking velocities analysis [e.g. Perroud and Tygel, 2005]. If interval velocities are instead required to be

used for other tasks such as poststack and/or prestack time or depth migration, time-to-depth conversion and/or geotechnical site characterization, they can be derived with a 2D tomographic inversion approach [Duveneck, 2004] which may be used to replace the 1D Dix velocity conversion [Dix, 1955].

1.2 Structure of the thesis

This thesis has eight chapters organized into a theoretical part, from Chapters 1 to 4, and into a practical part, from Chapters 5 to 7.

In this Chapter I have illustrated the general motivations and purposes behind my research.

In Chapter 2 I will summarize the basic principles of the seismic reflection method and the techniques for data acquisition and data processing that are commonly used. An overview on the shallow and ultrashallow seismic reflection methods and on the difficulties and pitfalls that may be encountered during the phases of data acquisition and data processing is also given.

In Chapter 3 I will present the conventional CMP stack method, with special emphasis on its processing steps, such as velocity analysis and residual static corrections, which play a major role in CMP imaging of near-surface reflection data. With this in mind I will point out the practical and technical aspects that due to the strong heterogeneity of the near-surface materials, often entails laborious and time-consuming velocity analysis and residual static corrections, which inevitably increase the complexity of data processing and thus its costs. Replacing the conventional CMP stack method with the CRS stack method provide a means of overcoming these CMP-processing related difficulties.

In Chapter 4 initially I provide a descriptive explanation to show that, compared to the well-known CMP stack, the CRS stack is neither a radically new concept nor a "magic box" but nothing more than an extension of the former, which has the relevant advantage of stacking traces from multiple CMP gathers within so-called CRS apertures. In this way the CRS stack achieves stacked sections with better S/N and reflection continuity than a CMP stack. Afterwards, I provide the theoretical background to derive by means of the geometrical optics the CRS stack operator for inhomogeneous media. I complete Chapter 4 with a description of the nonstretch NMO effect of the CRS stack, of the NIP-wave tomography method for velocity model building, of CRS-based surface consistent residual static corrections and of event-consistent smoothing for the CRS parameters. These are CRS-based processing tools relevant for the CRS processing of near-surface reflection data. If combined with the CRS stack process, they allow for fully data-driven implementation of processing chains entirely based on the same CRS assumptions. These do not necessitate manual picking in velocity spectra nor a priori information concerning the unknown macrovelocity model. This make the CRS stack a very attractive cost-effective alternative to the CMP stack in the field of near-surface investigations.

In Chapter 5 I will compare the CMP and CRS results obtained for the time imaging of a shallow (few hundred meters depth) P-wave dataset collected to delineate the hydrogeological framework of a paleolake environment. The CRS stack that I obtained without any preliminary formal and time-consuming velocity analysis, shows a large number of false alignments of seismic energy which hinder its interpretation. Conversely, the CRS stacked section that I obtained weighing each sample with the corresponding value of CRS coherence and number of CRS appear more suited for interpretation than either the CMP and or the CRS stacked sections. Using the NIP-wave tomography method [Duveneck, 2004] I also estimated the interval velocity field from the CRS wavefield attributes and I compared the result with the interval velocity field obtained applying the Dix equations [Dix, 1955] to the stacking velocity field computed by the standard CMP velocity analysis.

Chapter 6 deals with illustrating the results obtained applying the CMP and CRS stack process to an ultrashallow SH-wave dataset characterized by very high vertical and lateral resolution. Using the CMP stack method with a extremely detailed, but also very time-consuming, stacking velocity analysis I image a dipping bedrock interface below four horizontal reflectors in unconsolidated, very low velocity sediments, with a well-defined pinch-out at less than 10 m depth. Conversely, I quickly implemented the CRS stack process avoiding any interactive procedure on the pre-stack data obtaining a CRS stacked section that, despite the improved continuity of the shallowest reflector, appears excessively smoothed (i.e. smeared) and unable to well-image the pinch-out as its CMP counterpart. By restricting the stack process to only the traces within single CMP gathers I obtained a stacked section very similar to the one obtained through the conventional CMP, but in few minutes and without any processing related effort. Using the kinematic wavefield attributes determined for each stacking operation, I retrieved also a velocity field fitting the stacking velocities I had estimated in the CMP processing.

Chapters 5 and 6 have both been published under the following citation: Deidda, G. P., E. Battaglia, and Z. Heilmann, 2012, Common-reflection-surface imaging of shallow and ultrashallow reflectors: Geophysics, **77**, B177–B185.

In Chapter 7 I tested the CRS stack method using synthetic datasets with intersecting reflection traveltimes, such as those generated by the strong velocity gradients, which are often found in near-surface surveys. Compared with those of the conventional CMP stack method, the obtained results show that the CRS stack can be helpful to process data exhibiting strong velocity gradients. The results from this study are going to be submitted for publication.

In Chapter 8, I will make some concluding remarks and discuss further the perspectives of the CRS stack for near-surface applications.

Chapter 2

The seismic reflection method

The seismic reflection method is a powerful geophysical technique which uses the reflection of seismic waves to obtain an image of the Earth's interior [Yilmaz, 1987]. Seismic waves are mechanical perturbations that propagate into the ground as compressional (P-) and shear (S-) body waves, at velocities governed by the elastic properties of the medium in which they are travelling. At geological interfaces where the elastic properties of the medium change sharply, seismic waves are reflected, refracted and diffracted. According to Snell's law and to Huygens and Fermat's principles a portion of their seismic energy returns back towards the surface as refracted, reflected and/or diffracted waves. The aim of the seismic reflection method is to use a controlled seismic source to start the propagation of seismic energy into the ground, and to record the reflected waves at the surface, using an array of seismic receivers positioned along straight profiles at known distances from the seismic source.

For every source event, each receiver records a seismogram, also called seismic trace, which is a time series representing the subsurface response at the receiver location. Each trace has a zero reference time, corresponding to the time of the source event. Processing all the seismograms of a survey allows one to obtain an image of the Earth's interior as well as a set of helpful attributes as stacking and interval velocities, quality factors (e.g. the Q parameter) and changes of 'amplitude versus offset (AVO) which play an important role in the interpretation of seismic data. When the subsurface geological structures are separated by well-defined contrasts of density, seismic velocity or both, the reflection method can provide results that closely resemble a true geological section of the subsurface. For this reason the reflection method is often defined as an "imaging" technique.

The reflection method was developed in the early 30's by the petroleum industry to search for geological traps in sedimentary rock environments. The commercial importance of hydrocarbons and their economic rewards have generate immense amounts of financial investments into the research and development of aspects related to the acquisition and processing of seismic reflection data. It is no surprise therefore, if today the seismic reflection method is the most advanced and widespread geophysical technique. It is routinely employed for oil and gas explorations both on land and at sea, using arrays of thousands of receivers to investigate depths of up to several kms. Since the

early 80s the acquisition and processing techniques established for deep seismic surveys have alos been successfully adapted and applied to shallow seismic studies. However, it is only in recent years that the widespread availability of multi-channel engineering seismographs with wide dynamic range combined with adavanced computer facilities on hand at a relatively low price, have made the reflection method a viable option also for near-surface investigations.

In the following sections I will provide a short summary of the main techniques and strategies used for the acquisition and processing of seismic reflection data, together with an overview on the seismic reflection method for near-surface investigations.

2.1 The seismic reflection method problem

The main purpose of the techniques used for the acquisition and processing of seismic reflection data is to extract from the field records the reflected signals from which the information about the subsurface can be obtained. For seismic reflection imaging only the reflected body waves of a specified wave type, either compressional or shear waves, are considered as signal, while everything else is to be considered noise. However, a seismic source generates not only the desired downgoing travelling waves, but also other events such as horizontally travelling waves (direct-waves), high amplitude surface waves (e.g. Rayleigh and Love waves), diffracted and critically refracted waves, which interfere with the reflected signals (see Figure 2.1). Additionally, field records always contain incoherent noise, i.e. random noise, caused, for instance, by traffic, industry, or wind. Both coherent and incoherent noise, whose magnitude can be predominant to that of the reflections, may lead to records with poor signal-to-noise (S/N) ratios, namely with low signal energy levels compared to those of the surrounding noise. To remove or at least to attenuate all the waveform components which are not intended to be imaged, it is necessary to use specific acquisition and processing strategies. A first step in this direction is the so-called preprocessing, which aims at enhancing the reflections at the expense of the other events using a number of signal processing routines such as filtering, muting, scaling and removing of bad or noisy traces [see e.g. Yilmaz, 1987]. However, the most important noise removal process is the stack, i.e. the sum of traces which sample the same subsurface location. Assuming to stack N traces, the amplitude of the signals stacked constructively is proportional to N, while that of everything else, including the unwanted noise, is reduced of a factor equal to $\sqrt{N}$. The stack process thus results in a S/N ratio improvement equal to $\sqrt{N}$ [e.g. Yilmaz, 1987].

The stacking techniques that were initially used tended to obscure details because they stacked the reflections from portions of reflectors too large. To overcome this intrinsic limitation Mayne [1962] proposed the common midpoint (CMP) stack method. The general idea of CMP stack is to acquire a series of traces which reflect from the same common subsurface midpoint, and then to sum them up in order to obtain a S/N ratio superior to that of the single prestack traces. With the increase in available computing power more sophisticated stacking strategies have been developed. Some of these such as the dip moveout (DMO) correction and/or the poststack migration are able to integrate and improve the CMP stack method; others as the pre-stack imaging either

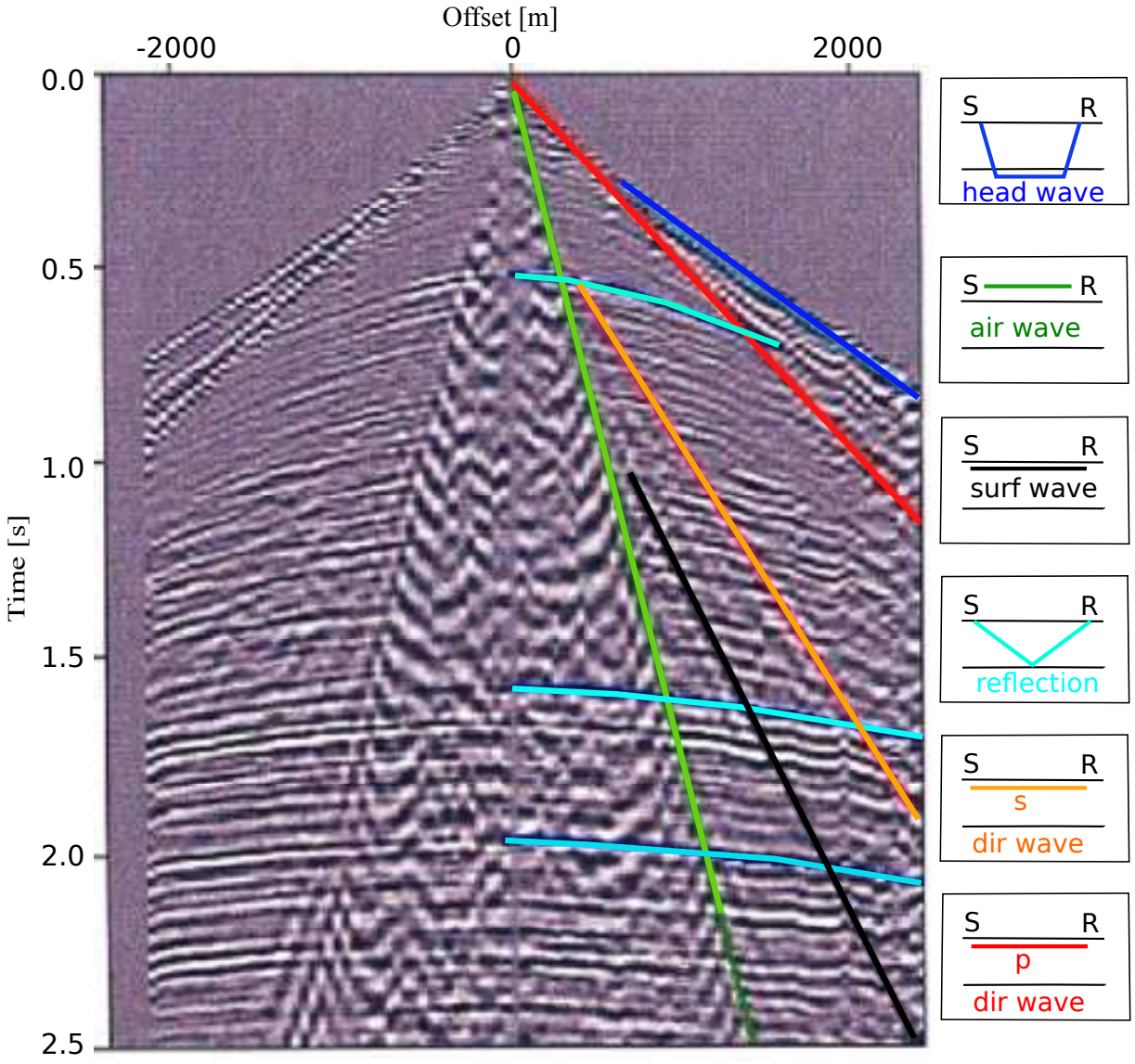

Figure 2.1: Example of land shot gather. Several kinds of events, in addition to reflections, are marked in the right side of the record. For each marked event, the small box indicates the path and wave type from source to receiver. The reflection event shows hyperbolic traveltime delay with increasing offset - the normal moveout effect. Only a few of the reflections are marked [Liner, 1999].

in time or in depth entirely replace it. However, the CMP stack method still remains an important processing step within the seismic processing flow. It has the main advantage of providing a time image section with substantially improved S/N ratio using simple and computationally not overly expensive procedures. This is also the reason why it is the standard stacking scheme used for shallow and ultrashallow seismic reflection data processing. The principles behind the CMP stack method are reviewed in Chapter 3.

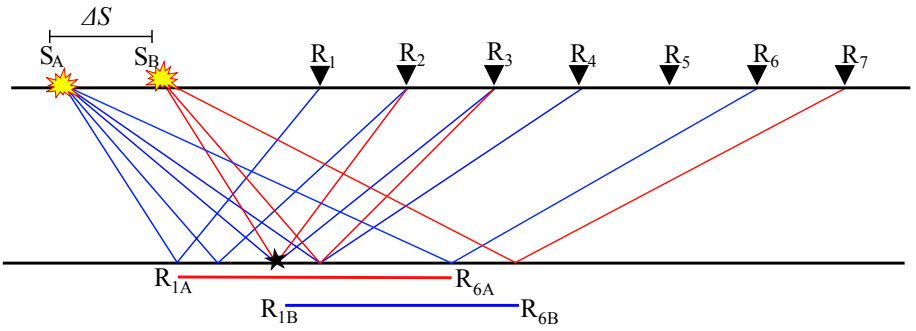

Figure 2.2: Illustration of multiple fold geometry. Assuming a homogeneous overburden, a regular acquisition geometry and according to Snell's law, the point indicated by the star is illuminated twice by the source/receiver pairs $S_A R_3$ and $S_B R_2$.

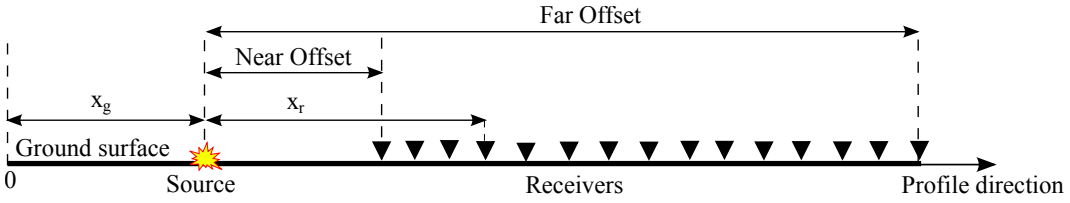

Figure 2.3: Illustration of multichannel seismic reflection data acquisition geometry.

2.2 The seismic gathers

To gain full advantage from the stacking procedures and additionally to estimate the propagation velocity of the waves, seismic reflection data are acquired so that each point on a reflecting interface of the subsurface is illuminated several times by different pairs of sources and receivers (see Figure 2.2). Gathering multiple fold data (i.e. data with multi traces per sub-surface position) allows for the collection of redundant information about the same reflection subsurface location, which can be used to reduce the noise and create a more reliable seismic image.

Multi fold acquisition is conventionally accomplished through a large number of independent seismic experiments or shots, each of which consists of a seismic source and of an array of seismic receivers placed at the measurement surface. For two-dimensional reflection surveys, the only type considered within this thesis, the receivers are equally spaced along a straight line at offset distances progressively increasing from the seismic source (see Figure 2.3). For each shot the sources can be at one end (off-end configuration) or in an intermediate position with respect to the seismic line (split-spread configuration). After each shot the source or the entire source-receiver setup (spread) is rolled forward to a certain distance multiple of the spacing between receivers. As the shots roll along, more than one source-receiver pair resamples the same subsurface position. Proceeding with this acquisition geometry, the resulting seismic traces can be sorted in groups or gathers, which relate to hypothetical experiments with specific source and receiver geometries (see Figure 2.4).

Seismic gathers play an important role in data processing as they are used to reorganize the information contained on a multi fold seismic reflection dataset. The common

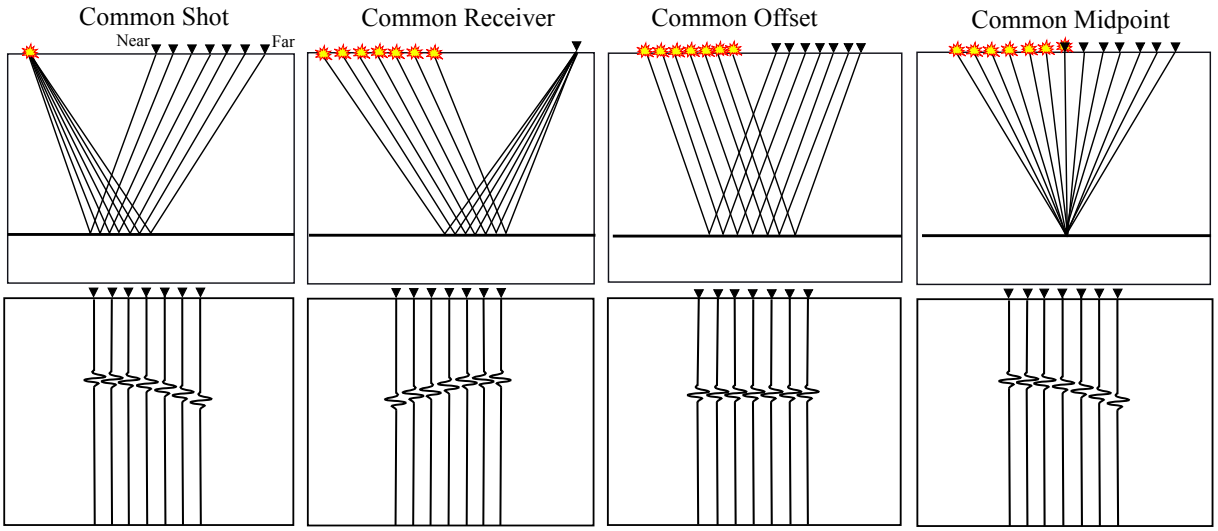

Figure 2.4: Seismic gather types and geometries for a simple horizontal reflector below a homogeneous overburden. The red dots are the shot positions while the ones gray-shaded the receiver positions. The ray-paths and the corresponding seismic traces are also depicted.

shot gathers (CSG) and the common receiver gathers (CRG) are the groups of traces with the same source x_S and receiver coordinates x_R respectively, while the common offset gathers (COG) are those with the same offset value $h = (x_R - x_S)$. The CSG and the CRG are used to inspect the traces corresponding to particular shot or receiver locations (i.e. to evaluate the effects produced by faulty shots/receivers), and to estimate the static corrections associated to each single position of source and receiver. The COG gathers approximate a time image section of the subsurface and are used for basic quality controls so as to estimate possible trigger inaccuracies. The common midpoint CMP gathers are the groups of traces with the same midpoint coordinates $x_M = (x_R + x_S)/2$, and are used in the CMP stack method to improve the S/N ratio of the records. The CMP are equally spaced along the seismic profile at half the spacing between the receivers. The number of traces they contain determines the fold of the stack or degree of coverage of that CMP gather. Usually the stacking fold of the dataset increases at the beginning of the line going up to its maximum value, which remains constant until the end of the line, where it decreases.

A convenient way to represent the multi fold seismic reflection dataset and corresponding seismic gathers is the stacking chart schematically represented in Figure 2.5. Alternatively a data cube with axes in the offset, midpoint, and time domain can be used (Figure 2.6).

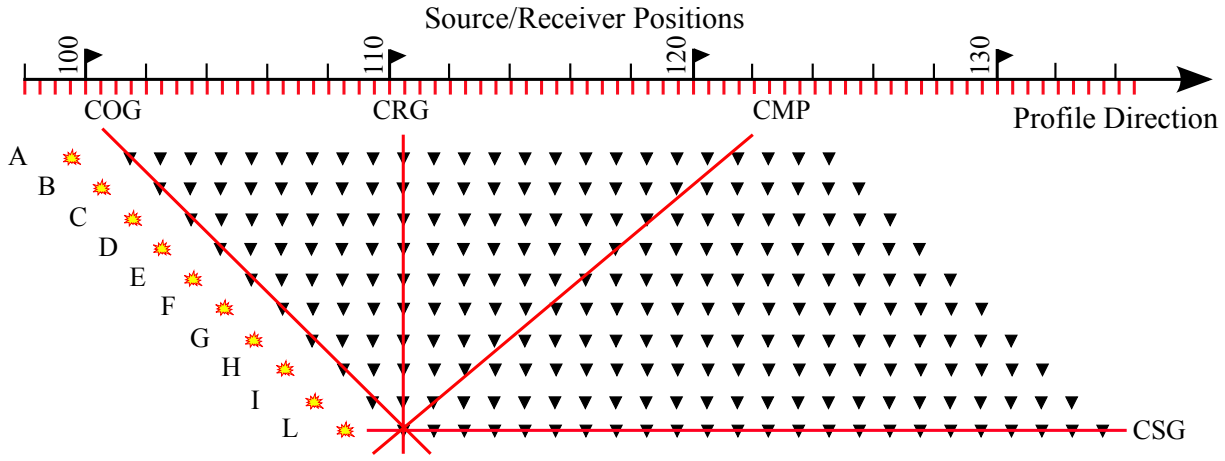

Figure 2.5: Example of stacking chart. The stars indicate single shots while the blacks triangles represent single receivers.

2.3 Near-surface seismic reflection methods

2.3.1 Overview

There is no satisfactory definition on what the near-surface for the seismic reflection method is. Its meaning has changed continuously due to the technological and theoretical improvements that overtime have progressively reduced the minimum recording depth from some tens of meters to less than two meters [e.g. Bachrach et al., 1998; Bachrach and Nur, 1998; Baker et al., 1999]. One possible distinction is that proposed by Steeples et al. [1997] which defines as "shallow" the reflection surveys aimed to investigate the portion of subsurface comprised between some tens to some hundred meters depth, and as "ultrashallow" those surveys targeting the first ten meters.

Development of the shallow and ultrashallow seismic reflection techniques has been marked by the continuous adaptation and improvement of the procedures for data acquisition and data processing pioneered by the hydrocarbon industry for deep seismic surveying. Initially these were extraordinarily complicated and unsuitable to deal with the near-surface seismic reflection profiling. Progressively, the increasing understanding of the various near-surface waveforms together with developments in software, powerful computer facilities and engineering seismographs led to better adaptation. Several ideas and concepts first conceived many years ago, thanks to technological advancements in microelectronics and computing powers, become technically and economically recently viable.

Attempts in using the reflection method to characterize the near-surface geology have been carried out since the early 1950s by Evison [1952], one of the first to have experienced the inadequacy of the standard seismic techniques for shallow surveys, particularly recognizing the need for high frequencies to record the shallow reflections without interference. Later, Pakiser's research group at the U.S. Geological Survey obtained successful P-wave records from depth less than 50 meters [Pakiser and Mabey, 1954; Pakiser and Warrick, 1956; Warrick and Winslow, 1960], but they had to abandon their

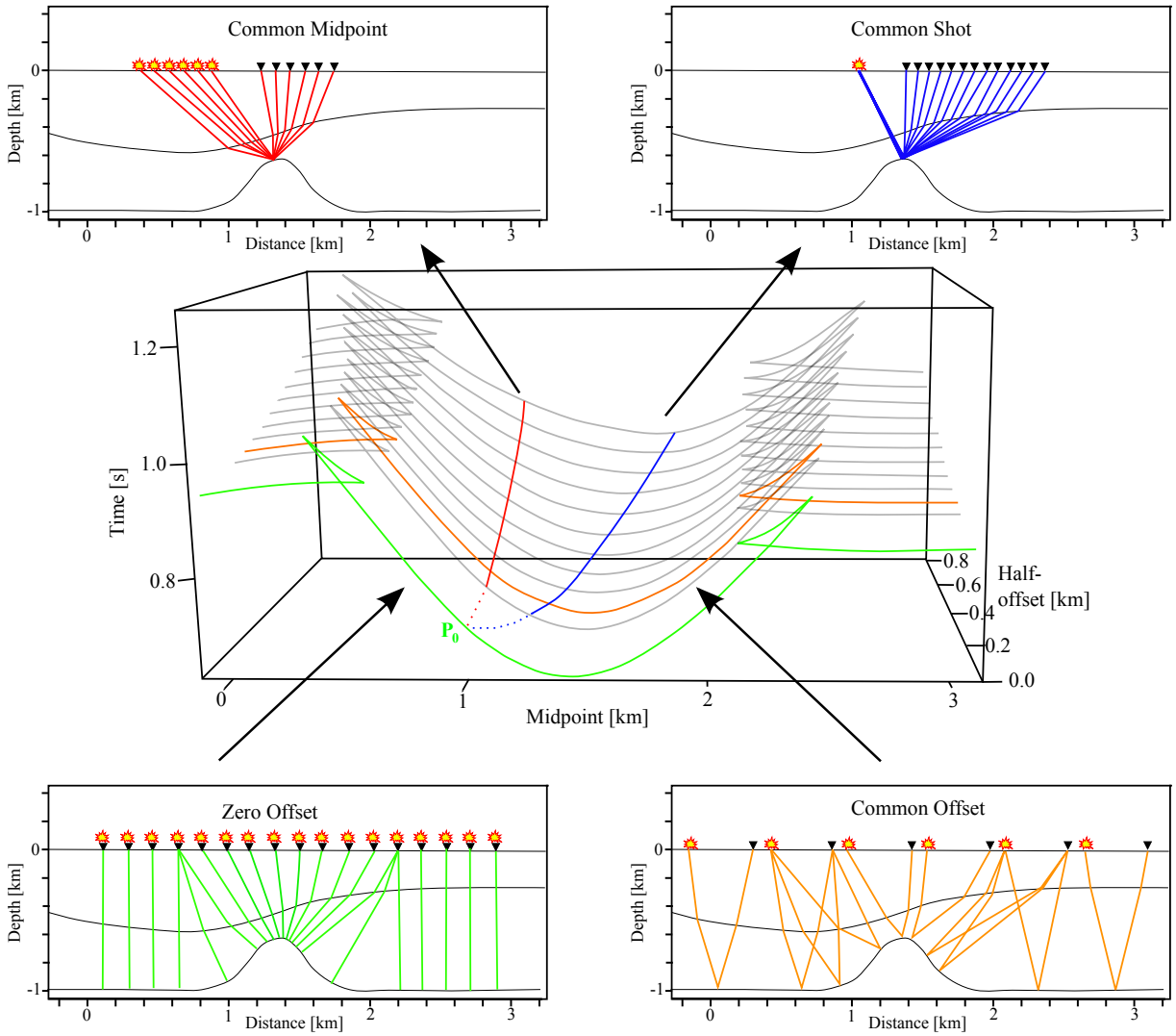

Figure 2.6: In the center, a 3D data volume typically used to visualize multi-coverage prestack data acquired by 2D acquisition is displayed. Only the traveltimes corresponding to one reflector are considered and the temporal extend of the recorded pulse is omitted. The volume can be divided into several subvolumes corresponding to specific source and receiver arrangements: A common shot (CS) gather contains all traces that have one and the same shot coordinate in common (blue). Similarly, the common-midpoint (CMP) gather (red) and the common-offset (CO) gather (yellow) contain all traces that have a certain midpoint position or a certain offset in common. The zero-offset (ZO) section (green) is a special kind of common-offset gather which cannot be directly acquired, but is usually simulated from the prestack data. Figure according to Höcht [2002].

experiments due to the prohibitive costs involved. The modern shallow seismic reflection method can be said to have begun with the work of Schepers [1975] who obtained excellent P-wave reflections from depths less than 20 meters. Later on, between the late 1970's and early 1980's, an increasing number of academic research groups started to focus on studying near-surface seismic reflection methods [e.g. Green and Mair, 1983; Green and Soonawala, 1982; Herber et al., 1981; Mair and Green, 1981; Ruskey, 1981; Steeples, 1984; Steeples and Knapp, 1982; Ziolkowski and Lerwill, 1979]. This led to significant progress in the application of high-resolution seismic reflection techniques in many engineering and environmental commercial projects including:

- mapping depth to bedrock [Hunter et al., 1984; Miller et al., 1989],
- detecting fractured and/or shallow fault [Ghose et al., 2013; Hawman and Ahmed, 1995; Miller and Steeples, 1986; Treadway et al., 1988],
- determining shallow stratigraphies [Ali and Hill, 1991; Brouwer et al., 1997; Clague et al., 1991],
- locating subsurface cavities and buried structures [Branham and Steeples, 1988; Deidda and Balia, 2001; Kourkafas and Goulty, 1996; Miller and Steeples, 1991; Miller et al., 1995; Steeples et al., 1986],
- groundwater studies [Birkelo et al., 1987; Deidda et al., 2006; Haeni, 1986].

Developments on the application of the SH-wave reflection method for shallow and ultrashallow reflection surveys [e.g. Deidda and Ranieri, 2001; Hasbrouck, 1991; Hasbrouck and Padget, 1982], and those in techniques for three-dimensional (3D) shallow and ultrashallow seismic imaging are more recent [e.g. Büker et al., 2000; House et al., 1995].

2.3.2 Data acquisition and processing

The main targets in environmental/engineering-scale seismic exploration are situated in the shallow ($\sim$ 200 m) subsurface, which is an area that may be quite difficult to investigate with seismic reflection methods. As a matter of fact, at these depths, the acquisition of reflection data is often impeded by the direct, head-waves, guided, surface and air waves that arrive at about the same two-way-traveltimes (twts) as those of the much weaker reflected waves [see e.g. Robertsson et al., 1996b]. The amount of such coherent noise and its degree of interference with reflection events are generally hard to predict because they are very site specific. For this reason it is always advisable to carry out preliminary tests of noise, so called walkaway noise tests, in order to estimate the site noise properties and consequently to match the appropriate acquisition parameters. This phase should always be preferred to that of successive elaborate processing steps which, besides proving ineffective, can also lead to deterioration in data quality [Steeples et al., 1995].

An early recording strategy designed to minimize the effects of source generated noise was the optimum-window technique (OWT) proposed by Hunter et al. [1984]. The OWT aimed to set appropriate source-receivers offsets in order to record shallow reflection data within a space-temporal window between the first breaks (either direct and/or head waves and/or airblast) and the first arrivals of surface waves (either Rayleigh and Love waves). This strategy was initially performed in single fold configurations (i.e. with single traces per sub-surface position) and spread rapidly in the field of the near-surface investigations since it was quite effective using the engineering seismographs commercially available at those times. Its main drawbacks were the non-negligible efforts in determining the optimum recording windows, sometimes non existent, the single-fold coverage and associated low S/N ratio and the lack of reliable velocity information. These drawbacks were solvable by the common-mid-point (CMP) technique. However, this only began to be commonly used in engineering and environmental surveys in the 90's, i.e. when the advancements in microelectronics made commercially available personal computers with sufficient computing power for digital processing. These items were previously not easily available to those outside of large companies. The same being true for engineering seismographs equipped with sufficient number of recording channels (from 12 to 120). Actually for a long time the two techniques were used jointly to take advantage of both multi fold coverage and optimum recording conditions [Pullan and Hunter, 1990]. This occurred until the spread of engineering seismographs equipped with a sufficient high number of recording channels and adequate dynamic range (up to 24 bits of A/D) made the OWT technique obsolete. Whatever the technical specifications of the seismograph, to reduce the interference between source-generated noises and shallow reflections it is always necessary to use a sufficient number of both near and long offset traces, adequate high-frequency content (possibly more than 100 Hz), broad spectral bandwidth and sufficiently short spacing between geophones.

Processing shallow seismic reflection data is different from the seismic data processing carried out in hydrocarbon exploration [Baker, 1999]. Its main goal is to reduce the number of misinterpretations by avoiding the generation of coherent noise events, even at the expense of obtaining a final image of poorer quality. For this reason, after each single processing step the data processor should be absolutely certain of the origin of events present on staked section, as the difficulties of acquisition and processing of shallow seismic reflection data (e.g. see the introduction of this thesis) always make the trade-offs between benefits and disadvantages a necessity.

Figure 2.7 shows a generalized CMP processing flowchart with four main processing steps (i.e. raw data editing, preprocessing, CMP processing and stack). Each is composed of a number of processing routines, but only some of them are always required, while the others should to be applied, depending on the specific data problem.

The most common pitfalls encountered in processing of shallow reflection data relate to spatial and temporal aliasing, misinterpretation of source-generated noise as pure reflections, inadequate velocity analysis, inappropriate static corrections and inaccurate stretch-mute functions [see e.g. Steeples and Miller, 1998]. The latter have been analyzed and discussed in detail by Miller [1992]. Robertsson et al. [1996a,b] and Roth et al. [1996] showed that source-generated noise, such as the guided waves, may have the same frequency content as shallow reflections, so that therefore frequency filters may

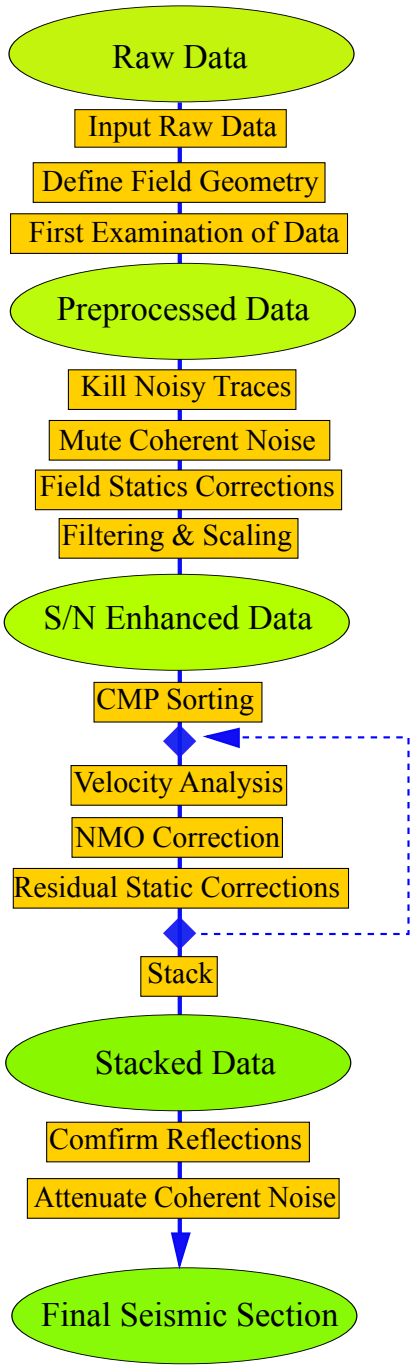

Figure 2.7: General processing flow for shallow reflection data. In general the velocity analysis/NMO correction/residual statics processing chain is iteratively repeated until satisfactory stacked section are obtained Baker [1999].

be ineffective for their elimination. Black et al. [1994] documented that at very shallow depths (i.e. less than 50 meter) and low near-surface velocities (< 1000 m/s) the migration is often unnecessary. In addition, since the migration is basically an inversion process, the low number of channels per record and low S/N ratios often encountered in the near-surface data prevent from an optimal migration process.

2.3.3 Vertical and lateral resolution

Seismic resolution is the ability to separate two features that are close together [Sheriff, 2002]. This is governed by the dominant wavelength of the recorded signals, namely by their frequency content and by their seismic velocities. The lower the frequency content of the data the lower the seismic resolution.

The limit for the vertical resolution is generally accepted in one quarter of a dominant wavelength of recorded data [Widess, 1973]. It can be increased using seismic sources to generate signals with high-frequency content. The practical limit to the use of high-frequency signals is the seismic attenuation, which acts along ray paths as a high-cut natural filter. Accordingly, the deeper the target is, the lower the frequencies content of reflections and thus the resolution. Maximum attenuations occur in the least consolidated near-surface materials and may significantly change between sites or within single sites.

The lateral resolution is generally expressed by the concept of first Fresnel zone, which is the portion of a reflector from which the reflected energy reaches a detector at arrival times less than one-half wavelength from the first break. In practice, this defines the minimum width of a detectable feature for a given depth, seismic velocity and frequency content wave [e.g. Yilmaz, 1987]. Accordingly, lateral changes less than the first Fresnel zone cannot be detected on stacked sections. In practice this limit can be proven to be pessimistic and accordingly geophones spacing should be much closer than the Fresnel zone limit.

In shallow seismic reflection, dominant signal frequencies are typically between 50 and 200 Hz, with a practical upper limit around 500 Hz [Steeples, 1998]. Compressional wave velocities in dry unconsolidated sediments vary from as low as 100 m/s [Bachrach et al., 1998; Bachrach and Nur, 1998] to as high as 2000 m/s. Velocities in waters saturated sediments are to the order of 1500 – 2500 m/s. Typical velocities for the vadose zone and saturated zone are around 400 m/s and 1700 m/s respectively. Given the range of expected frequencies, and based on the $\lambda/4$ criteria [Widess, 1973], the seismic reflection method for near-surface investigations can expect to resolve features to the order of 0.4 – 2.0 m in the vadose zone and 2 – 10 m in the saturated zone. These are just rough guidelines and actual results are strongly site dependent. Resolution and depth of penetration can be much higher or lower, depending on the source and energy absorption characteristics of the Earth's materials.

Vertical and lateral resolutions also depend on the S/N ratio of the data. An acoustic impedance contrast cannot be clearly depicted in the data if the amplitude of the reflected wave is less than the ambient noise. Stacking the traces is a common way to

enhance the S/N, theoretically by a factor equal to the square root of the number of stacking traces. In practice, the ever present small changes in amplitude levels of single traces and existing temporal shifts between neighbouring traces hinder the stack process which tends to act as high-cut filter, necessarily reducing the resolution.

Chapter 3

The CMP stack method

In this chapter I briefly show the theoretical backgrounds concerning the CMP stack method and related processing steps as velocity analysis and residual static corrections. In doing this I will refer to the theory of the seismic rays normal to the wavefronts of the propagating waves, which is the high-frequency approximation (so called zero-order ray theory) of the elasto-dynamic wave equation.

3.1 Basic principles

The common-midpoint (CMP) stack method introduced by Mayne [1962] is the standard stacking procedure for seismic reflection data. Its basic idea is that for a horizontal layer below a homogeneous overburden the source-receiver pairs with the same common midpoint (CMP) location collect signals reflected by a common depth-point (CDP) or common-reflection-point (CRP) located in depth directly beneath the corresponding CMP position (Figure 3.1). Therefore stacking the corresponding seismic traces in such a way that only the events reflected from the same CRP point contribute constructively to the sum (while everything else is subject to destructive interference) will provide a single stacked trace with a S/N ratio much higher than that of individual prestack traces. Assuming there are no amplitude variations between the traces and perfectly distributed random noise, the S/N improvement equals the square root of the number N of stacked traces, i.e. of the fold coverage. In practice, since these conditions are never perfectly met, the gained improvement is somewhat less than $\sqrt{N}$.

In order to coherently stack within a CMP gather the signal reflected from the same CRP point in the subsurface, it is necessary to know its CRP traveltime trajectory, namely the time-distance relation that exist between the CMP traces. For a single horizontal reflector below a homogeneous overburden this is exactly described (according to the Pythagorean theorem and to geometrical optics principles) by a hyperbola:

$$t^2(h) = t_0^2 + \frac{h^2}{V_{NMO}^2} \tag{3.1}$$

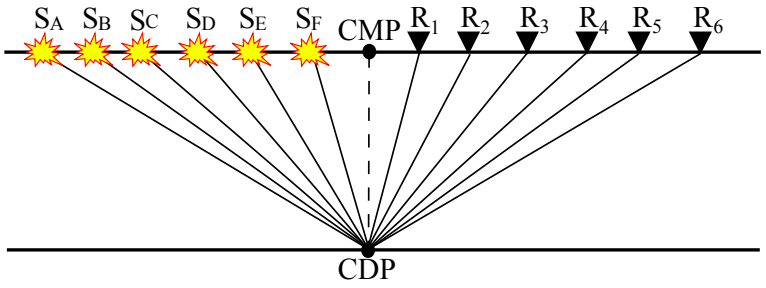

Figure 3.1: CMP geometry for a horizontal reflector.

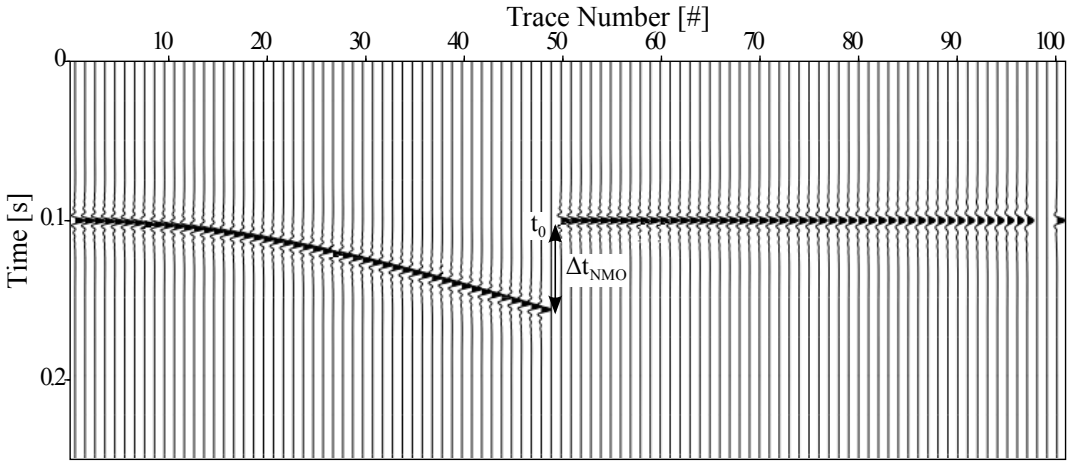

Figure 3.2: The reflection response for a single horizontal reflector is shown in traces 1–48. The zero-offset traveltime t_0 corresponds to the arrival time at the zero-offset trace 1. Δt_{NMO} depicts the normal moveout for a specific offset. Traces 50–97 show the corresponding normal moveout corrected CMP gather: the event is flattened. In trace 101 the stacked trace is depicted. It results from a horizontal summation of the NMO-corrected CMP gather (traces 50–97).

where h is the source-to-receiver distance (offset) and t_0 the traveltime measured for coincident source-receiver pair ($h = 0$). The V_{NMO} is the so-called normal moveout (NMO) velocity, which in this simple case is the velocity of the overburden (Figure 3.1). The traveltime difference:

$$\Delta t_{NMO}(h) = t(h) - t_0 = t_0 \sqrt{\left[1 + \left(\frac{h}{V_{NMO}\, t_0}\right)^2\right]} - t_0 \tag{3.2}$$

is called normal moveout (NMO) and it is the delay in arrival times of reflected signals due to different source-receiver offsets. The NMO is compensated through the NMO correction, which implies to remap according to Equation 3.2, the signals recorded with arbitrary offset h into their corresponding zero-offset (ZO) approximation (see Figure 3.2). Accordingly, by determining the V_{NMO} the NMO effect can be removed and, in turn, the NMO effect can be used to determine the V_{NMO}. In practice the NMO and the V_{NMO} are linked together. After the NMO correction, the CMP traces are horizontally stacked together to produce a single stacked trace which is placed into the corresponding CMP location. Repeating this process for all the CMP gathers of the

dataset produces a stacked section with a S/N ratio higher than that of the prestack traces. The stacked section may be interpreted as the time image of the subsurface that would be recorded if a source-receiver pair was placed at each CMP position.

A slight generalization of the previous time-distance relationship is obtained considering a dipping reflector below a homogeneous overburden. The corresponding CRP traveltime is still a hyperbola [Levin, 1971]:

$$t^2(h) = t_0^2 + \frac{h^2 \cos\alpha}{V^2} = t_0^2 + \frac{h^2}{V_{NMO}^2} \tag{3.3}$$

being α the dip angle of the reflector, V the velocity of propagation of the seismic wave in the medium and t_0 the ZO two-way traveltime measured along the normal to the reflector. Therefore, to coherently stack the reflection events an apparent velocity greater than the actual velocity of the medium is required. Accordingly, a dipping layer with low velocity yields the same V_{NMO} as a horizontal layer with higher velocity. As a consequence, a velocity inversion based on the moveout would lead to an apparent medium velocity $V_{apparent} = V_{NMO}$ higher than the actual medium velocity V.

For N arbitrary horizontal isovelocity layers the time-distance relation becomes a curve of higher order [Taner and Koehler, 1969]:

$$t^2(h) = t_0^2 + \frac{h^2}{V_{RMS}^2} + C_i\, h^{2i-2} + \ldots \tag{3.4}$$

where $C_i (i = 2, 3, \ldots, \infty)$ is an infinite series of coefficients which depend on the thickness and velocities of each of the N layers. If the offsets are relatively small compared to the depth of investigation the series of coefficients can be truncated with sufficient accuracy up to the second order. The resulting time-distance relation is a hyperbola, whose curvature depends on the root-mean-square velocity V_{RMS}. The V_{RMS} is an apparent velocity, which makes the traveltime of a wave propagating in a multi-layer medium (characterized by thickness $k_1, k_2, \ldots, k_N$ and velocities $v_1, v_2, \ldots, v_N$) equal to the traveltime of a wave propagating along a homogeneous medium with thickness $k = \sum_{j=1}^{n} k_j$.

If the N layers are assumed with arbitrary dip, then the CRP traveltime curve becomes [Hubral and Krey, 1980]:

$$t^2(h) = t_0^2 + \frac{h^2}{V_{NMO}^2} + \textit{higher order terms} \tag{3.5}$$

As in the previous case, if the spread is small compared to the depth of investigation the higher order terms can be ignored and the resulting traveltime curve is again a hyperbola whose curvature depends on:

$$V_{NMO}^2 = \frac{1}{t_0 \cos^2\beta_0} \sum_{k=1}^{N} v_k^2\, \Delta t_k \prod_{i=1}^{k-1} \left(\frac{\cos^2\alpha_i}{\cos^2\beta_i} \right) \tag{3.6}$$

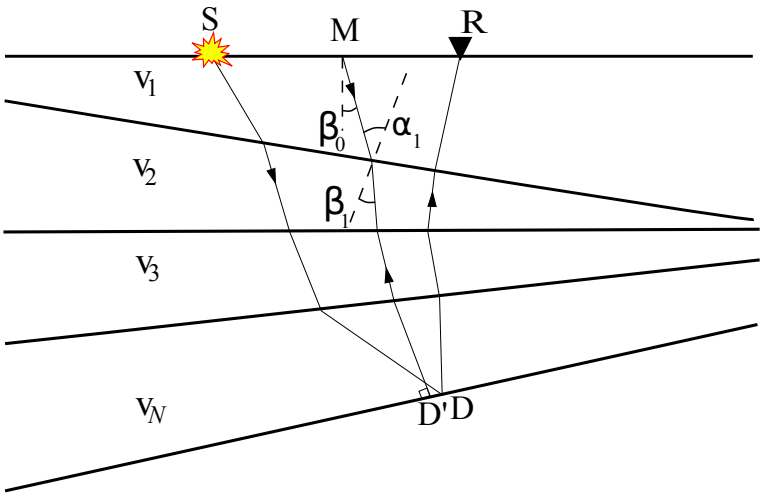

Figure 3.3: NMO geometry for a dipping reflector in an earth model with layers of arbitrary dips (Modified from Yilmaz [1987]).

being α_i and β_i the angles as indicated in Figure 3.3. If the dipping angles are assumed not to be too large, this V_{NMO} can be approximated with the V_{RMS} for horizontal layers.

The V_{NMO}, thus, is the true propagation velocity of the seismic waves only for the ideal situation of a single horizontal reflector beneath a uniform overburden. As geology becomes complex the V_{NMO} depends on model parameters such as incidence angles, interval velocities and reflector curvatures, and though still with the dimensions of a velocity it loses its physical meaning.

When the subsurface geological conditions are different from those of horizontal isovelocity layers the CMP gathers collect signals which are no more reflected by a single CRP located vertically below the shot-receiver midpoint, but rather signals reflected from a series of CRPs dispersed (i.e. smeared) along the reflector (see Figure 3.4). Simply stacking these signals would decrease the quality of the stacking process and consequently the S/N ratio of the stacked traces. The equivalence between CRP and CMP can be partially restored by means of the so called dip moveout (DMO) correction which tries to remove the smearing effect due to the reflector dip [e.g. Deregowski, 1986; Hale, 1991]. However, it does not remove the smearing effect caused by the reflector curvature or by the presence of lateral velocity variations. Accordingly, when geology becomes complex, the DMO corrections fails and the remaining reflection point dispersal will negatively affect the CMP stacking process. In practice, if the subsurface geology does not violate too much the assumptions of the CMP method, it can be used with sufficient accuracy the general traveltime equation expressed in the form of Equation 3.1, with the V_{NMO} that will change according to the subsurface.

3.2 The velocity analysis

If the assumptions of the CMP stack method are sufficiently accurate, the inverse traveltime problem can be solved by determining the V_{NMO} from the reflection events. The

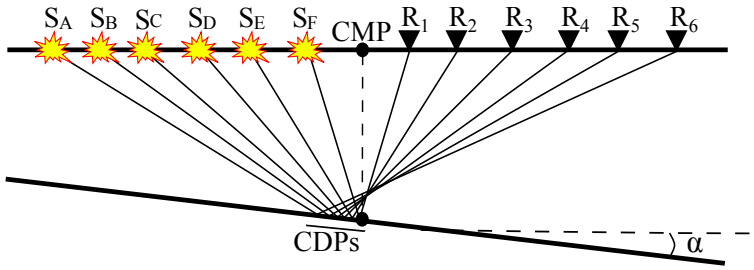

Figure 3.4: Reflection point smearing occurring over a single dipping reflector.

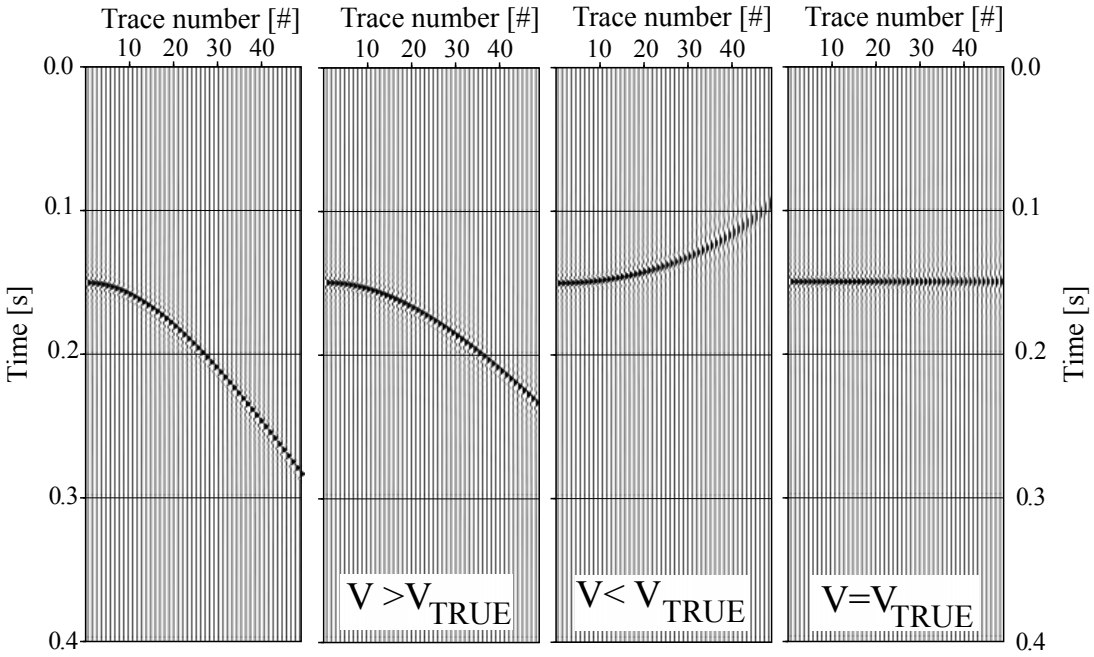

Figure 3.5: NMO correction of a reflection. (a) Reflection is not corrected; (b) velocity is too low; (d) velocity is too high; (d) NMO-correction with proper velocity.

V_{NMO}, therefore, is of crucial importance within the CMP stack process. Without a good set of V_{NMO} the reflection events will not be correctly expressed on the final stacked section and less than optimal seismic stack results will be obtained. Its estimation is obtained through the so-called velocity analysis, which is essentially a forward-modelling procedure aimed at searching on the CMP gathers for the pairs of (t_0, V_{NMO}) that best fit the recorded CRP trajectories. There are some conventional schemes commonly used to perform the velocity analysis. Each of these has its benefits and drawbacks that make it preferable in some conditions rather than in others, depending on the amount of moveout and S/N ratio of the recorded data.

A very simple but quite effective velocity analysis procedure consists in checking if the trial pairs (t_0', V_{NMO}) produce a good NMO correction, namely if they adequately align the reflection events respective to their zero-offset traveltime t_0. The more accurate the alignments the more accurate the stack will be. Conversely, too high or too low velocity will produce respectively undercorrected and overcorrected curves (see Figure 3.5) which will yield to less than optimal stacking results. This can be easily verified assuming a planar reflector below a homogeneous overburden of depth D and velocity V. The

resulting reflection event corrected for normal moveout would read:

$$t'_0\,(h, t'_0, V_{stack}) = t_{(h)}(h, t_0, V) - \Delta t_{NMO}(h, t'_0, V_{NMO}) \tag{3.7}$$

In Equation 3.7 the pair (t_0, V) defines the actual traveltime path while the pair (t'_0, V_{NMO}) the trial hyperbola. Deriving the previous relation along the offset direction and assuming $V_{NMO} = V$ and $t'_0 = 2D/V$ it results:

$$\frac{\partial t'_0}{\partial h} = \frac{\left(\frac{2h}{V^2}\right)}{2\sqrt{T_0^2 + \left(\frac{h}{V}\right)^2}} - \frac{\left(\frac{2h}{V^2}\right)}{2\sqrt{T_0^2 + \left(\frac{h}{V}\right)^2}} = 0 \tag{3.8}$$

which is the mathematical condition for a straight line on the plane th (i.e. the seismogram). Accordingly the flattening can be used as a measure for the accuracy of the assumed (t'_0, V_{NMO}) pair.

In the same way, the constant velocity scan method aims to flatten the reflection events using a range of trial V_{NMO}. To better identify the (t'_0, V_{NMO}) pairs the NMO-corrected CMP gathers are displayed next to each other in the form of a panel. The map is then obtained picking from the panel and interpolating the pairs (t'_0, V_{NMO}) that best flatten the reflection events. This velocity analysis technique may be the best available method for data with very poor S/N ratios.

The constant velocity stack (CVS) uses a slightly different approach based on the best stacking response. To this end, a certain number of neighbouring CMP gathers are progressively NMO-corrected and stacked using a range trial V_{NMO}. The resulting CMP stacked traces are then displayed next to each other to form a CVS panel. The sought time-variable V_{NMO} velocity function is the one that yields the best stack response in terms of S/N ratio and reflection continuity along several neighbouring CMP gathers, i.e. the one which best focuses the reflection events. The constant velocity stack of all the CMP gathers (brute stack) can be used to provide a first raw image of the subsurface.

The velocity spectra is definitely the most widely used velocity analysis technique. It is based on the generation of the so called velocity spectra, which essentially are plots that display the values assumed by a certain measure of signal coherency along appropriate defined curves, function of time and velocity. In general these are obtained for single CMP gathers sweeping for different t_0 a predetermined set of trial velocities $(v_1, v_2, \ldots, v_N)$ incremented with a regular interval Δv. Each pair of (t_0, v_N) produces a particular hyperbolic moveout trajectory along which the coherence measure is evaluated and then displayed on the spectra plot (see Figure 3.6). The stacking velocity function is obtained picking (manually or automatically) and interpolating the maxima peaks on the velocity spectrum obtained as a function of time and velocity. This process may be iteractively repeated until optimal stacked results are obtained. The most commonly used correlation criterion for the generation of spectra velocity plots is the semblance coefficient defined by Neidell and Taner [1971]:

$$S_i = \sum_{j=i-M}^{i+M} \left(\sum_{k=0}^{N+1} q_{j\,k} \right)^2 \Bigg/ N \sum_{j=i-M}^{i+M} \sum_{k=0}^{N+1} q_{i\,k} \tag{3.9}$$

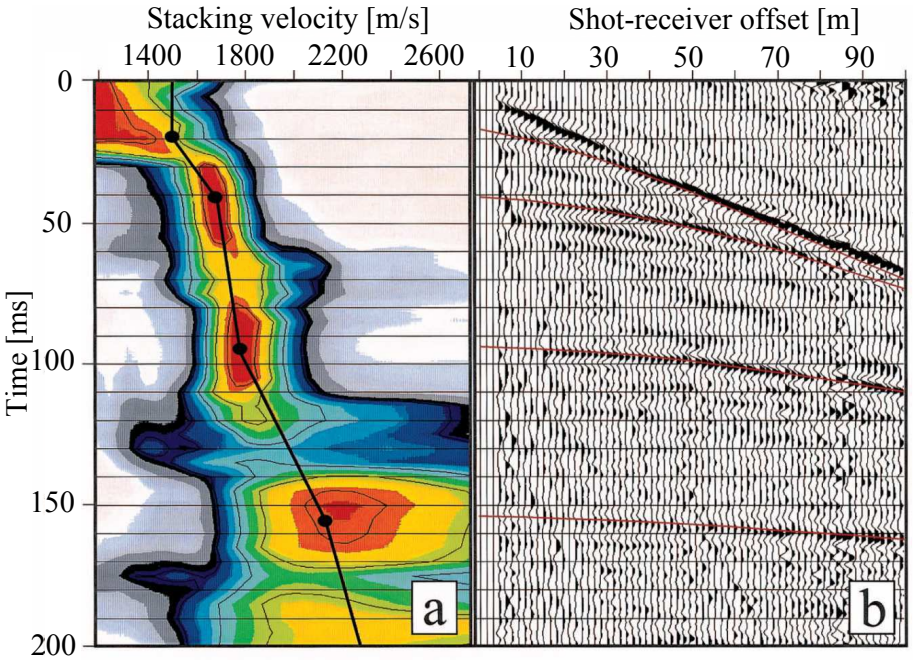

Figure 3.6: Stacking velocity analysis in a CMP gather. (a) Velocity spectrum.(b) NMO hyperbolas plotted over the CMP gather. Semblance values obtained along NMO hyperbolas are plotted as a function of zero-offset traveltime and stacking velocity. Maxima (red) correspond to reflection events in (b) [Büker et al., 2000].

It is computed through the amplitudes q of M samples taken from N traces in a time window of $2M+1$ samples length and centred at time index i, along the CRP trajectories generated by the trial velocity function. The semblance coefficient assumes values between 0 and 1, becoming 1 only if all signal values (or samples) that enter Equation 3.9 are identical. In practice, since the amplitudes of the reflection event usually change from trace to trace due to varying reflection coefficients, different geometrical spreading, temporal shifts etc, the semblance coefficient will never become 1 even if the corresponding trajectory exactly matches a reflection event.

3.2.1 The stacking velocity

Even if the V_{NMO} is the searched velocity to solve the inverse seismic problem, what all velocity analysis techniques actually provide is the velocity that produces the best stacking result. This so called stacking velocity V_{stack} is a mathematical parameter that defines the curvature of the best-stacking hyperbola, i.e. the hyperbola which produces the best stacking result:

$$t^2(h) = t_0'^2 + \frac{h^2}{V_{stack}^2} \tag{3.10}$$

The V_{stack} has the dimension of a velocity, but it has no physical meaning. Likewise t_0' is a twt which generally differs from the t_0 of the actual reflection event. The values (t_0', V_{stack}) are closely related to the concept of maximum stack. In the t^2h^2 plane they define the straight line that produces the best least square fitting of the true reflection

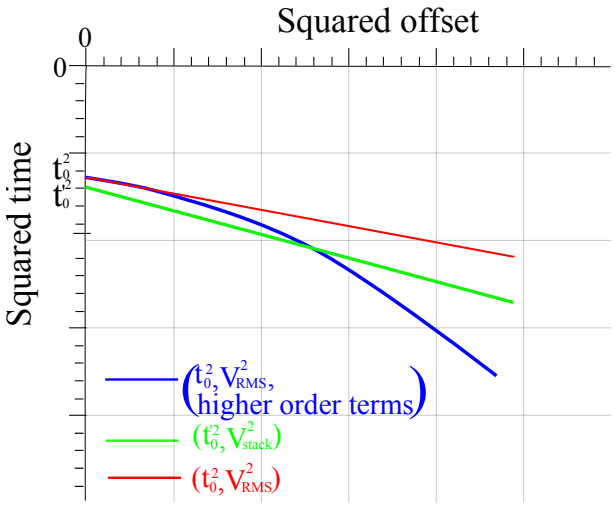

Figure 3.7: Small spread approximation (green) and best least square fitting (red) of the true (blue) CRP traveltime for N isovelocity layers arbitrary dip. The pair (t_0', V_{stack}) is the best least square fit of the true CRP traveltime for large offsets.

traveltime curve described by 3.5 (Figure 3.7). The difference of stacking velocities from NMO velocities, and in general, the difference of data-derived moveout parameters from the coefficients of corresponding traveltime approximation, is called spread-length bias [see e.g. Al-Chalabi, 1973; Hubral and Krey, 1980]. It is caused by a number of different factors, the most important of which are the difference of the actual reflection traveltime curve from a hyperbolic shape and the finite offset aperture used during velocity analysis. The spread-length bias plays a significant role whenever moveout parameters determined from the seismic data are used for further applications as, for example, the determination of interval velocities from stacking velocities. For shallow and ultrashallow seismic reflection data these effects have been analyzed in detail by Bradford [2002].

3.2.2 The velocity analysis in practice

Whatever technique is used, the velocity analysis is always plagued by a number of pitfalls which are more tedious in near-surface data rather than at the deep exploration scale [see e.g. Al-Chalabi, 1973; Steeples and Miller, 1998].

Inaccuracy in V_{NMO} may be caused by the lack of enough normal moveout for the reflections. Small NMO curvatures yield to a loss of sharpness on the peaks of the velocity spectra and to an enlargement of the V_{NMO} with the same comparable stack results in the CVS panels. This decrease in velocity resolution inevitably leads to less than optimal stacking results which may be particularly harmful for shallow and ultrashallow seismic reflection data, where small variations in NMO velocity of few meters per second can result in apparent subsurface structures without any matching with the data.

The coherence measures used to determine the V_{NMO} are affected by different factors such as time gate length, i.e. the temporal window within which the coherence measure

is performed, poor S/N ratios, low fold coverage and wavelet change along the offset, which may introduce erroneous peaks. In these situations the picking of the appropriate stacking pair (t'_0, V_{stack}) requires a high quality control by the user.

When the normal moveout departs from the hyperbolic path due to anisotropy or lateral heterogeneities or simply not totally compensated static shifts, the corresponding traveltime distortions cause misfit between trial hyperbolic path and real reflection events, which adversely affect the accuracy of the velocity analysis. In these situations higher-order traveltime approximations and/or residual static corrections routines might help to improve the results.

Further details on pitfalls commonly encountered during the velocity analysis for shallow and ultrashallow seismic reflection data are reported in the introduction of this thesis.

3.2.3 The NMO stretch

One of the main drawbacks of the conventional velocity analysis techniques and related NMO corrections is the well known pulse-stretch effect, namely the decrease in the frequency content of stacked traces [see e.g. Yilmaz, 1987]. This unwanted wavelet stretching phenomenon is particularly detrimental for reflection events with offsets relatively large compared to the depth (or traveltimes) under investigation. A commonly used technique to reduce the pulse-stretch effect is by muting prior to the stack the traces exposed to a stretch ratio higher than an acceptable value set by the user. This allowable stretch ratio greatly influences the seismic resolution of the stack results, especially for shallow and ultrashallow seismic reflection datasets which are characterized by relatively large offsets compared to the depths of investigation [e.g. Miller, 1992].

Contrary to what is frequently believed, the root of the pulse-stretch effect is not due to non-hyperbolic moveouts nor to different dynamic adjustments in the same seismic traces: it occurs even in single perfectly hyperbolic traveltime. It is rather related to the method used to apply Equation 3.2. This can be easily verified with a simple subsurface model composed of a planar reflector overlaid by a homogeneous overburden. Assuming z_0 as the reflector depth and V as the velocity of propagation of the seismic waves in the overburden, the traveltime of the corresponding reflection event recorded within a CMP gather is exactly a hyperbola:

$$t(h) = \sqrt{t_0^2 + \frac{h^2}{V^2}} \tag{3.11}$$

where $t_0 = 2\,z_0/V$ is the ZO two-way traveltime and h is the source-receiver offset. In the xt plane the asymptote of this hyperbola passes through the origin with the slope equal to $2\,V^{-1}$. For a band-limited source pulse (i.e. for real data) and assuming for the sake of simplicity a medium without attenuation, the reflection response would be a band of constant width (the pulse width) around the traveltime curve 3.11, i.e. more than one sample per trace defines the actual reflection response. The ideal NMO correction should simply move the whole band of samples around the traveltime curve 3.11 onto a band of the same width around the horizontal line $t = t_0$. For a given source-receiver

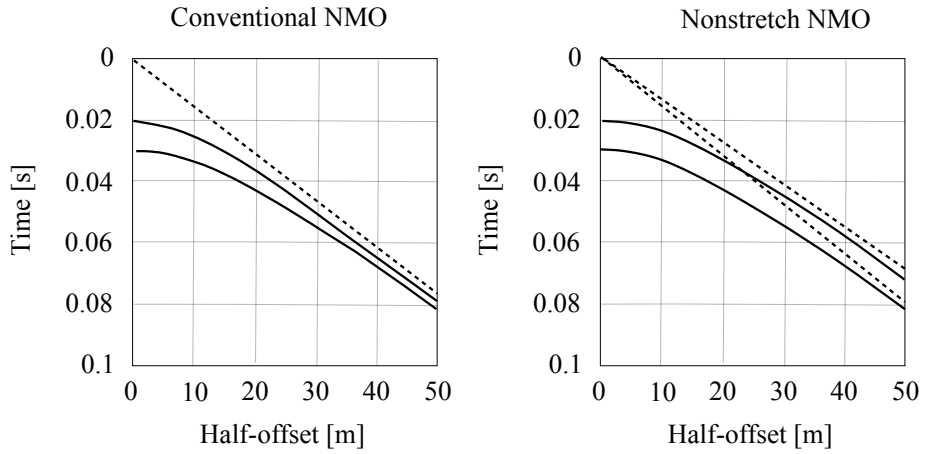

Figure 3.8: Comparison between conventional NMO (left) and nonstretch NMO (right). The hyperbolae corresponding to the onset and the end of a reflection event are shown (solid lines), together with their asymptotes (dashed lines). At half-offset h equal to 25 m, the vertical line reveals the separation between the hyperbolae. For conventional NMO, the hyperbolae converge with h, while for nonstretch NMO, their distance is kept equal for the chosen h [Perroud and Tygel, 2004].

offset h_{fix} this would imply moving all the samples within the pulse width upward of the same Δt_{NMO}:

$$\Delta t_{NMO} = \sqrt{t_0^2 + \frac{h_{fix}^2}{V_{NMO}^2}} - t_0 = C_0 \tag{3.12}$$

namely:

$$t_0^2 + \frac{h_{fix}^2}{V_{NMO}^2} - t_0 = C_1 \tag{3.13}$$

where C_0 and C_1 are arbitrary constants. Both previous relations imply that along the wavelet width the V_{NMO} decreases at the increase of the traveltime t_0. The corresponding traveltime hyperbolas within the pulse width are isomoveout curves, i.e. with the same moveout, parallel to each other (Figure 3.8). Conversely, for a given reflection event the conventional stacking velocity analysis provides an estimation of the corresponding V_{NMO} for user-selected values of t_0, generally with an increase of V_{NMO} between increasing traveltimes t_0. Restricted to the simple case of planar reflector with homogeneous overburden, a fixed $V_{NMO} = V$ would provide for two ZO traveltimes t_0 and $t_0 + \tau$ within the same seismic pulse two moveout hyperbolas converging at the same asymptote $t = 2V^{-1}$, i.e. with different moveouts (Figure 3.8). The resulting NMO correction causes the stretch of the reflection pulse because within the same trace (i.e. offset h_{fix}) smaller time samples will be moved upward of Δt_{NMO} larger than those of later time samples. This effect increases with offset and decreases with zero-offset time of a stretch ratio [Dunkin and Levin, 1973]:

$$\frac{\tau'}{\tau} = \frac{t(h)}{t_0} \tag{3.14}$$

The pulse stretch effect would occur even if the stacking process took place along hyperbolic trajectories rather than straight lines. In such case, assuming still a single

reflection event with $V_{NMO} = V$, as the offset increases, an increasing number of adjacent stacking trajectories with different t_0 tend to the same asymptote $t = 2V^{-1}$. The resulting stacked traces will show the original reflection pulse stretched for interpolation along adjacent traveltimes t_0, those of the stacking trajectories that, tending to $t = 2V^{-1}$, pass within the same reflection pulse.

There are various methods proposed to overcome the pulse stretch effect [see e.g. Masoomzadeh et al., 2010; Zhang et al., 2013, and references given within], but these are rarely used because generally they are overly complicated. It is rather preferred to apply a mute function to reject the signals stretched more than a user defined limit. For exploration data this is conventionally fixed to 50%, but for shallow and ultrashallow seismic reflection dataset this limit can be reduced to less than 30%. This obviously implies the loss of information contained at larger offset.

3.3 Static corrections

The statics are undesired deviations on the arrival times of the seismic energy caused by lateral changes in elevation and thickness, as well as by vertical and lateral velocity variations, occurring in the low-velocity-layer (LVL). The LVL is the uppermost part of the subsurface which is often called weathering layer as it is mainly induced by weathering. Compared to the sub-weathering layers, the LVL exhibits lower velocities with strong and rapid changes in both velocity and thickness, which cause misalignments and distortions on the reflected events. Their removal is achieved through so-called static corrections, which according to Sheriff [2002] are: "Corrections applied to seismic data to compensate for effects of variations in the weathering layer. Their objective is to determine the reflection arrival times which would have been observed if all measurement had been made on a (usually) flat plane with no weathering or low velocity material present ". The term static stands for corrections independent from the record time, contrary to the term dynamic which is used to indicate corrections depending on record time (e.g. the NMO correction). The statics and corresponding corrections are distinguished on the basis of their wavelength in field and residual statics.

The field statics are time distortions whose spatial variation is longer than the length of the geophone spread. They are primarily related to major topographic variations along the survey line, and usually they don't affect the traveltimes within each CMP gather but rather the structural interpretation of the final stacked section. The field statics are removed by evaluating the thickness of the LVL below each station location, using supplementary information such as source and geophone elevations, up-hole times and refraction data [e.g. Marsden, 1993a,b]. Being independent from the velocity analysis, the field statics are usually resolved during the pre-processing of the data.

The residual statics are short-period time shifts with wavelengths shorter than the length of the receivers spread. The residual statics appear as differences on the arrival times of neighbouring traces that distort the expected hyperbolic traveltime of the reflected events (see Figure 3.9). These misalignments lead to an incoherent stack process that destroys and corrupts the reflected signals rather than enhancing them [e.g. Marsden,

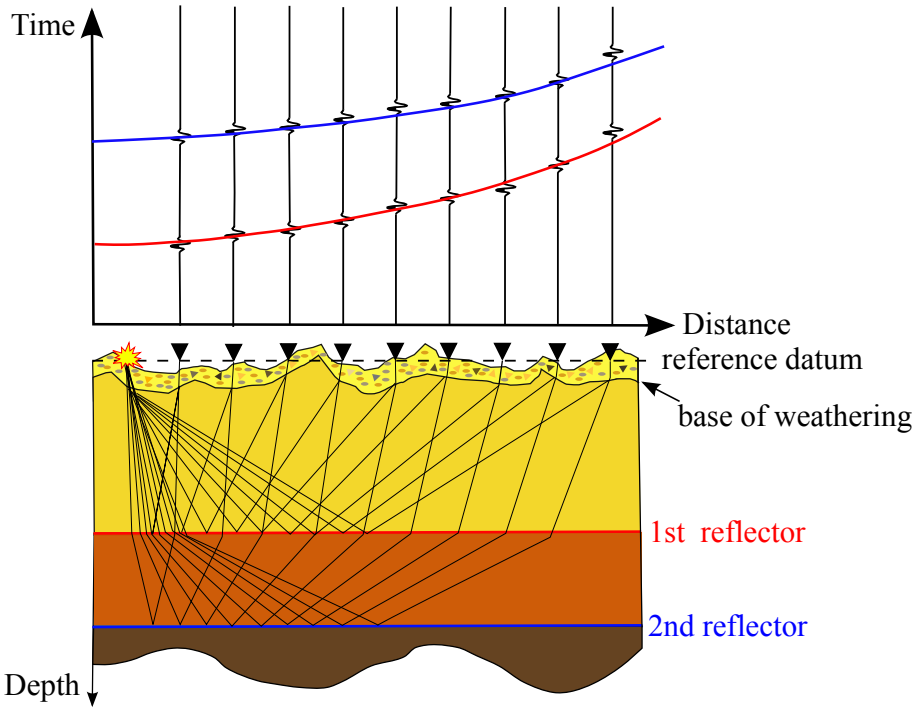

Figure 3.9: Illustration of the possible misalignments induced by the weathering layer on the traces [Koglin et al., 2006].

1993a]. They are conventionally removed using statistical correlation routines that automatically try to recover the alignment of existing reflections using small time shifts within a user-defined limit. Unlike the field statics, the residual statics are solved together with velocity analysis. These two processes benefit from each other and generally are iteratively implemented together as if they were a single process.

Sometimes data exhibit also medium-wavelength time variations, mainly related to changes in thickness and velocity of the weathering layer that occur within the length of the geophone spread. Their compensation is a critical issue as they can both degrade the resolution and affect the structural interpretation of the final stacked section. The medium-wavelength statics are perhaps the most difficult statics to correct for using the conventional methods [see e.g. Kozyrev et al., 2004].

Below I briefly report the description of the techniques commonly used for the correction of residual static that, being strictly related to the velocity analysis, are of particular relevance in this thesis.

3.3.1 Conventional residual static correction assumptions

The basic assumptions used by the conventional residual static correction routines are [see e.g. Cox, 1999; Hileman et al., 1968; Taner et al., 1974]:

- time-consistency,

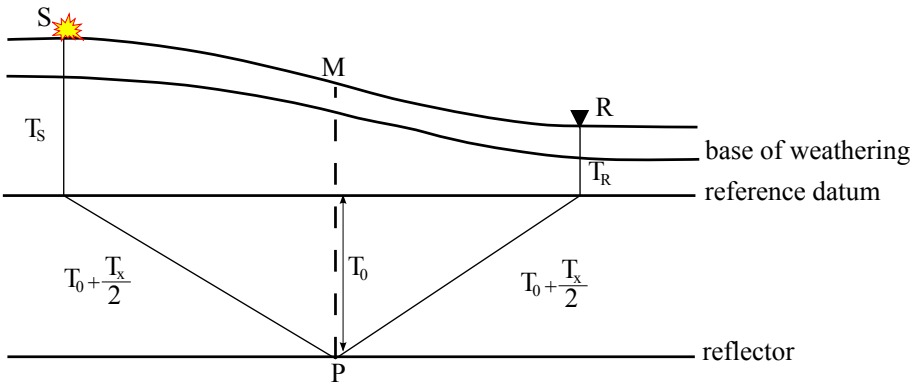

Figure 3.10: Idealized geometry for the statics surface consistent model.

- surface-consistency,
- wavelet change.

The time-consistency assumption imposes that the near-surface acts in the same manner regardless of the recording time. In practice it imposes that the induced misalignments are constant temporal shifts within single traces.

The surface-consistency assumption assumes that residual statics are time delays that depend only on the source and receiver location at the surface, but not on the path of the energy through the subsurface. This assumption implies a horizontal LVL with velocity remarkably lower than the sub weathering velocities so that, according to Snell's law, the waves travel through the LVL layer along paths close to the vertical (Figure 3.10). Accordingly, the misalignments induced by the LVL along different wave paths can be considered small.

The wavelet changes assumption implies that the LVL has no or at least the same influence on the shape of the wavelet of all emerging waves. Therefore the residual static correction routines do not include wavelet changes.

On the basis of previous assumptions residual static time shifts can be split into the following terms:

$$t_{ij} = s_j + r_i + G_{kh} + M_{kh}\, x_{ij}^2 \quad \text{with} \quad k = \frac{i+j}{2} \tag{3.15}$$

In particular:

- t_{ij} is the residual static shift associated to the trace with the j-th source, the i-th receiver.
- s_j is the static time shift associated with the j-th source station.
- r_i is the static time shift associated with the i-th receiver station.
- G_{kh} an arbitrary time shift for the k-th CMP gather along the h-th horizon that refers to subsurface structural variations.

- M_{kh} is a residual moveout term that accounts for the imperfect moveout correction for the *h-th* horizon.

The squared source-receiver offset $x_k^2 = (s_j - r_i)^2$ accounts for the offset dependency of term M_{kh}, which together with the structural term G_{kh} is assumed to be time variant (i.e. dynamic).

The objective of the surface-consistent residual static corrections is therefore to estimate t_{ij} or s_j and r_i and to associate one exclusive static time shift for each source and each receiver location. Despite its apparent simplicity, at the exploration scale the surface-consistent modeling fit the real data well enough [Yilmaz, 1987]. At the near-surface scale, instead, the surface-consistent modeling is not completely valid as the spread-length is often of the same order of the magnitude as the target depth, and consequently the down-going and up-going ray paths that leave the source and receiver locations are in general not completely vertical. Accordingly, the residual static correction routines may fail.

3.3.2 Linear traveltime inversion methods

The many different surface-consistent techniques conventionally employed in residual static corrections mainly vary in their approach in estimating s_j and r_i [e.g. Cox, 1999]. However, all of them determine the time shifts t_{ij} using the cross-correlation between pilot traces and single moveout-corrected traces with preliminary velocity functions. This conventional traveltime picking scheme is more reliable than the cross-correlation between single traces because of the improvement in S/N of the pilot trace. The most widespread approaches are CMP-based methods in which the cross-correlation takes places between individual NMO-corrected CMP traces and CMP stacked traces [Taner et al., 1974].

Once estimated t_{ij}, the s_j, r_i, G_{kh} and M_{kh} terms are evaluated by linear traveltime inversion methods. These define the static problem as the system of linear equations in the form of 3.15 that arise from the estimation of t_{ij} for each trace of the seismic dataset. Assuming for simplicity N_G CMPs with a constant fold N_F, the resulting number equations is $\approx N_G \cdot N_F$. The number of unknowns is instead equal to $N_S + N_R + N_G + N_G$ where N_S and N_R are the number of source and receiver locations respectively. Generally, $N_G \cdot N_F > N_S + N_R + 2N_G$ with more unknowns than independent equations and it is thus not possible to obtain an exact solution [Yilmaz, 1987]. An approximated solution is the one that minimizes in a least-square sense the sum of the energy between the modelled times t_{ij} and the observed picks t'_{ij}:

$$E = \sum_{ij} (t_{ij} - t'_{ij})^2 \tag{3.16}$$

Inserting Equation 3.15 in Equation 3.16 leads to:

$$E = \sum_{ij} (t_{ij} - s'_j - r'_i - G'_{kh} - M'_{kh}\, X'^2_{kh})^2 \tag{3.17}$$

whose minimum is found by imposing:

$$\frac{\partial E}{\partial s'_j} = \frac{\partial E}{\partial r'_i} = \frac{\partial E}{\partial G'_{kh}} = \frac{\partial E}{\partial M'_{kh}} = 0 \tag{3.18}$$

These conditions define a new linear system of $N_S + N_R + N_G + N_G$ equations with the same number of unknowns, which has as unique solution N_S source statics, N_R receiver statics, N_G structural terms and N_G residual moveout terms. Wiggins et al. [1976] proposed to solve this system using a Gauss-Siedel iterative procedure with initial values $s'_j = r'_i = G'_{kh} = M'_{kh}$. However, since the system of Equation 3.18 is under-constrained, it is always advisable to use reasonable constraints to reduce the possibility of errors and uncertainty.

The linear traveltime methods are able to estimate residual static corrections up to half of the dominant period of the reflection events. Therefore they may not be adequate to estimate larger time shifts especially in high noise conditions. In these situations the linear traveltime methods tend to be subject to so-called "cycle skipping" errors, namely they converge on a local solution rather than on the global one. Non-linear traveltime inversion methods take into account a greater number of possible peaks and are therefore more suited to accommodate possible large time shifts [see e.g. Rothman, 1986].

3.3.3 The stack power maximization method

The success of the traveltime decomposition methods mostly depends on the ability to achieve reliable static shifts. Generally, these are estimated by automatic picking of maxima in the cross-correlation results. This procedure, however, is sensitive to errors in the presence of ambiguities or noise within the cross-correlation results from which the time shifts are estimated. To reduce this sensitivity, Ronen and Claerbout [1985] proposed to evaluate the static corrections using the power of the stacked trace, i.e. the sum of their squared amplitudes. The basic idea behind this approach is that if all stacking traces are aligned with no relative shift then the resulting stacked trace has the highest power.

For a given time shift Δt the stack power $E(\Delta t)$between a pilot trace $G(t)$ and a shifted trace $F(t)$ equals to:

$$\begin{gathered} E(\Delta t) = \sum \left[F(t-\Delta t) + G(t)\right]^2 = \\ \sum \left[F(t-\Delta t)^2 + G(t)^2\right] + 2\sum \left[F(t-\Delta t)\cdot G(t)\right] \end{gathered} \tag{3.19}$$

By varying Δt, the maximum of the cross-correlation of the two traces (the second term in the latter expression) provides the maximum of the stack power $E(\Delta t)$ and the corresponding time shift. The sum of the power of the two traces instead, namely the first term in Equation 3.19, remains constant whatever the applied time shift Δt.

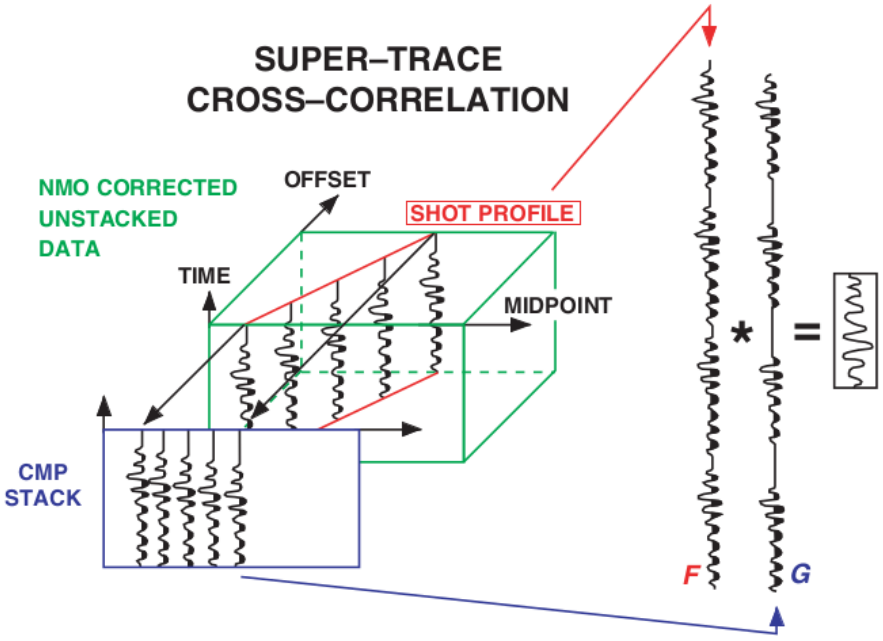

Figure 3.11: Example of supertraces for one moveout-corrected shot gather. Supertrace F and super trace G are cross-correlated to determine the corresponding source static [Ronen and Claerbout, 1985].

Accordingly, if $F(t)$ is an individual trace from a source location and $G(t)$ the corresponding CMP stacked trace, the source static correction can be estimated as the time shift that maximizes the power of the stacked trace. What Ronen and Claerbout [1985] actually proposed in their stack power method was something slightly different. A super-trace $F(t)$ built concatenating all NMO corrected traces within a shot gather is cross-correlated with another super-trace $G(t)$ built concatenating the CMP stacked traces corresponding to the relevant part of the stack, without the contribution of that shot in order to avoid the auto correlation of $F(t)$. Zero segments are positioned between the single traces to ensure that there is not cross-multiplication of data from one trace to another trace during the cross correlation procedure (see Figure 3.11). The cross correlation lag Δt with the highest stack power $E(\Delta t)$ is assumed as the residual static correction for the considered source location. Once derived, the static correction is immediately applied to the data and the whole process is repeated for the next gather incorporating the latest residual static corrections. Repeating this procedure for all the source and receiver gathers provides a one-step optimization surface-consistent residual static corrections without solving any inverse problem.

Like for all residual static correction routines the reliability of the stack power method proposed by Ronen and Claerbout [1985] relies on the initial NMO correction. Therefore, if the initial results are not satisfactory the whole procedure can be applied again together with the velocity analysis, until satisfactory results are obtained. Compared to other CMP-based surface consistent routines, the stack-power maximization method uses a higher number of traces to estimate single time shifts t_{ij}. This makes the stack-power maximization method more robust than the conventional correlation methods, especially with regards to data with low signal-to-noise ratios. However, since it does

not compensate for residual NMO correction, the method of Ronen and Claerbout [1985] turns out to be more sensitive to residual NMO errors. In addition, it doesn't take into account the structural term G_{kh} and therefore may suffer from inaccuracy when dealing with the data of complex subsurface structures. To this end some optional constraint can be accounted for within the procedure.

3.3.4 Residual static correction in practice

The quality of residual static corrections greatly depends on the cross-correlation window and maximum allowable static shift used.

The cross-correlation window is the time gate that defines the part of trace that has to be cross-correlated in order to estimate the residual static corrections. It must contain as many reflections as possible to reduce the discrepancy from the time invariance assumption. In addition it should avoid the reflection events with poor S/N and muted zone. Its choice is a critical step which can often be resolved only after some trial-and-error attempts.

The maximum allowable static shift is the amount of time shift between traces allowed during their cross-correlation. In principle it should be adequate to accommodate all possible combined shot and receiver static shifts at any given location. However, static shifts greater than the dominant period of the data may induce cycle skips errors especially for poor S/N ratio data. Conversely, small static shifts may be inadequate to account for all possible shot and receiver static shifts. Attempting to use small time intervals in sequence to avoid the possibility of cycle skipping errors without reducing the possibility of solving large time shifts is an alternative that unfortunately does not work properly [Yilmaz, 1987]. For shallow and ultrashallow seismic reflection dataset Steeples and Miller [1998] suggest to limit the maximum allowable static shifts to one-quarter of the dominant wavelet period, ensuring at least two (but preferably more) reflection events within the correlation window. However, as the frequency content of the reflection signals increases it becomes more and more difficult to compensate for the static anomalies minimizing the chance of generating static artefacts. This could be approached with some degree of confidence only when a large number of reflections are present. Unfortunately, this is not the case of shallow seismic reflection data where generally the number of reflection events is very low, often no more than two or three. In these cases, unsuitable cross-correlation window and/or allowable static shift could even set the stage for production of artefacts as bogus structures and coherent events from noise.

Further considerations concerning the pitfalls commonly faced in residual static corrections of shallow and ultrashallow seismic reflection data are reported in the introduction of this thesis.

Chapter 4

The CRS stack method

In this chapter I introduce the concepts of the CRS stack process and of the related CRS-based processing tools for deriving velocity information, residual static corrections and for event-consistent smoothing of CRS parameters. These processing tools permit the establishment of CRS processing chains based entirely on the same assumptions, operators, and apertures.

4.1 Introduction

The Common Reflection Surface (CRS) stack method [e.g. Jäger et al., 2001; Mann et al., 1999] is a seismic reflection imaging technique that produces the zero-offset section, stacking the traces whose sources and receivers are within the limits of a certain aperture in the vicinity of a central point x_0. Therefore, unlike the conventional CMP stack which evaluates the reflections within individual CMP gathers, the CRS stack spans several neighbouring CMP gathers to produce the so-called CRS-supergathers. Each CRS-supergather covers all the traces stemming from a common reflector segment centred in depth at the reflection point of the image ray, i.e. of the zero-offset ray which emerges at the image point location x_0 [Hubral, 1983]. The stack result is then placed at the location of the imaging point x_0. Since the number of traces falling into the CRS-supergather can significantly exceed the number of traces belonging to one CMP gather, the resulting CRS stacked section generally shows higher S/N ratio and better reflection continuity compared to its CMP counterpart. This is especially true in complex and/or low-coverage areas. Moreover, the high number of traces allows for the implementation of a stable data-driven process to determine accurate stacking parameters, velocity information and residual static corrections. This makes the CRS stack a much faster and less user interactive time-imaging procedure than the conventional CMP processing.

To fully understand the reason for using the traces of neighbouring CMP gathers to produce single ZO stacked traces, it is helpful to consider a laterally inhomogeneous model with dipping and/or curved reflectors and marked velocity variations in the overburden. In such conditions, the signals reflected from a common-reflection-point (CRP) in depth are not confined to single CMP gathers bacause it occurs the so-called reflection-point

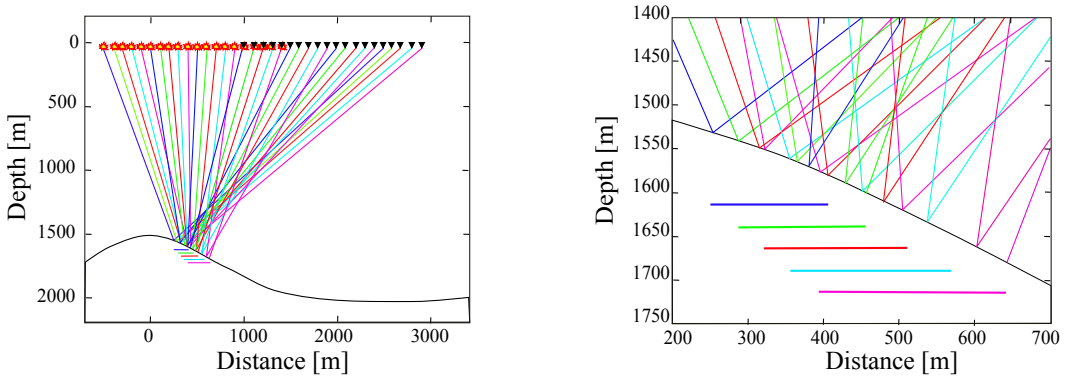

(a) (b)

Figure 4.1: (a) Ray families (in colour) for five neighbouring CMP gathers; (b) detail showing the regions covered by reflection points [Hertweck et al., 2007].

smearing [e.g. Yilmaz, 1987]. This is well illustrated in Figure 4.1a, where the ray families of few neighbouring CMP gathers together with their respective range of reflection points are shown above a curved reflector. Rays with the same colour belong to the same CMP family. Since that some reflection points are sampled by the rays of different CMP gathers (see Figure 4.1b), in principle it is not so strange to look for signals reflected from the same CRP in neighbouring CMP gathers. In practice however, this is never possible as it presupposes a perfect knowledge of the geometry and characteristics of the subsurface which, obviously, are themeselves the objective of the seismic survey. To recover the equivalence between CRP and CMP dip-moveout (DMO) correction can be used [e.g. Deregowski, 1986], which however will remove only the effect due to the reflector dip but not the reflection point dispersal caused by the reflector curvature or by the velocity variations on the overburden. Accordingly, as geology becomes complex the DMO corrections fails and a residual reflection point dispersal remains. In these cases thus, the CMP stack method uses events that are reflected in a certain vicinity of a central reflection point, i.e. the reflection point of the image ray, relying implicitly on the continuity of the reflector around it. Since this same assumption also underlies the DMO correction, using events that are reflected in the vicinity of a reflection point under consideration does not violate the principles underlying the CMP stack.

It is well known that since the seismic energy propagates into the ground with a finite-frequency content, its propagation affects not only the structures along the ray paths, as implied by the ray theory approximation, but rather a finite volume of space around the geometrical ray path. The intersection of this volume with a reflector yields the so-called first interface Fresnel zone, which defines the maximum achievable resolution in terms of reflector properties. The first interface Fresnel zone in the depth domain corresponds to the projected first Fresnel zone in the time domain. Accordingly, the major contribution stemming from a particular reflector segment in the depth domain can be found inside the associated projected first Fresnel zone in the time domain. Stacking the traces stemming from a common-reflector-segment (a common reflection surface for 3D surveys) within the first Fresnel zone around the supposed central reflection point, would improve the fold coverage of the central CMP gather without sacrificing the resolution on the final stacked section. This is what the CRS stack actually does: it uses the traces

of neighbouring CMP gathers to evaluate the reflection response of a reflection portion within the first Fresnel zone of arbitrary dip and curvature, including diffraction points and planar reflectors. Obviously, to take into account neighbouring CMPs the CRS stack has to add an additional data dimension along CMP direction, i.e. the midpoint direction. As a result, the stacking trajectories in the time-offset plane are replaced by stacking surfaces in the time-offset-midpoint volume. This implies the existence of continuous reflection events over several neighbouring CMP gathers, i.e. the considered reflector segment has to be continuous over at least the range of reflection points. This assumption, however, underlies also the NMO/DMO processing chain, which requires continuity of the reflector at least with regards to the portion on which the reflection point dispersal occurs. The CRS stack therefore is not a new stacking concept but simply the generalization, along the midpoint direction, of the conventional CMP stack method.

4.2 The CRS stacking operator

The so-called CRS stacking surface or CRS stacking operator is a second order traveltime relation. It approximates in the vicinity of the imaging point x_0 the kinematic reflection response of a common reflection segment of arbitrary dip and curvature, which is centred in depth at the reflection point of the image ray. Compared to the conventional CMP traveltime relation it has two additional traveltime components, which relate to the local slope and curvature of the reflector.

The CRS stacking operator can be derived either in time (data space) or in depth (model space) domain, depending on the type of parameterization used to describe the problem. The depth domain parameterization was employed in the original derivation of the CRS operator. It involves wavefield attributes which are closely related to the depth, slope and curvature of the common reflection segment [Hubral, 1983]. They are very suitable for inversion and/or event-consistent smoothing process, but being rather unfamiliar the CRS wavefield attributes tend to make the CRS operator unclear. Parameterization in the time domain, instead, is less common [e.g. Hertweck et al., 2007], but has the chief advantage of involving parameters which are closely related to the well-known NMO velocity concept. They are less suitable for inversion and/or smoothing process, but easier to understand than their model space counterparts.

In the following sections I will present a brief review of both approaches.

4.3 Depth domain CRS stacking parameters

As proposed by Höcht et al. [1999], one way to derive CRS traveltime relation in terms of depth domain parameters without any knowledge concerning the velocity model is by using the concepts of geometrical optics. The idea is to express the CRS traveltime relation as the ensemble of the CRP traveltimes of all the points that pertain to a reflection segment located around an arbitrary reflection point R. To this end, the

analytic formulae of the CRP traveltimes for curved interfaces in a homogenous medium with constant velocity (the so-called auxiliary medium) are firstly derived. These are then expressed as a function of the attributes of two hypothetical waves observed at the surface. In this way the location, orientation and curvature of the reflector segment located around the arbitrary reflection point R are parameterized in term of wavefield attributes (i.e. depth domain parameters) [Hubral, 1983]. The derived traveltimes are then extended to a inhomogeneous medium with constant near-surface velocity v_0 (i.e. the real medium) via a homeomorphic transformation [Höcht et al., 1999]. The Taylor series expansions up to the second-order in midpoint and half-offset coordinates of the so derived expressions provide the CRS traveltime relation or, so-called, hyperbolic CRS operator.

Following the approach of Höcht et al. [1999], I report below the geometric derivation of the CRS operator. The resulting formulae are derived from a kinematic point of view, meaning that neither the amplitudes nor possible phase shifts are considered.

4.3.1 CRP traveltimes for homogeneous medium

Assuming an arbitrary curved reflector below a homogeneous overburden of constant velocity v (Figure 4.2), as a result of Snell's law or Fermat's principle the isochron of a shot/receiver pair defined by the half-offset h and the midpoint x_m, is an ellipse:

$$F(x,z;x_m,h)=\frac{(x-x_m)^2}{\left(\frac{v}{2}t\right)^2}+\frac{z^2}{\left(\frac{v}{2}t\right)^2-h^2}-1=0 \tag{4.1}$$

where $t=t(x_m,h)$ is the traveltime of the shot/receiver pair. Setting in Equation 4.1 the half-offset $h=$ const provides the (x,z) coordinates that describe the isochron in the depth domain as a function of the midpoint location x_m. Therefore, solving the resulting relation together with the envelope condition $\partial F/\partial x_m=0$ provides the (x,z) coordinates of a curve tangent to all the ellipses for each midpoint location x_m, namely the depth domain coordinates of the reflector:

$$x=x_m+\frac{1}{2h^2}\frac{1}{t'}\left[\left(\frac{v}{2}t\right)^2-h^2\right]\left[1-\sqrt{1+4h^2\left(\frac{t\,t'}{t^2-\left(\frac{2h}{v}\right)^2}\right)^2}\right] \tag{4.2}$$

$$z=\sqrt{\left[\left(\frac{v}{2}t\right)^2-h^2\right]\left[1-\left(\frac{(x-x_m)^2}{\left(\frac{v}{2}t\right)^2}\right)\right]} \tag{4.3}$$

where $t'=\partial t/\partial x_m$. Now, considering an arbitrary point $(\hat{x_m},\hat{h},\hat{t})$ on the generic common-offset section of the multicoverage dataset which is supposed to have been collected from the ideal subsurface of Figure 4.2, if the slope $\hat{t'}=\frac{\partial t}{\partial x_m}|_{x=x_m,h=\hat{h}}$ of the

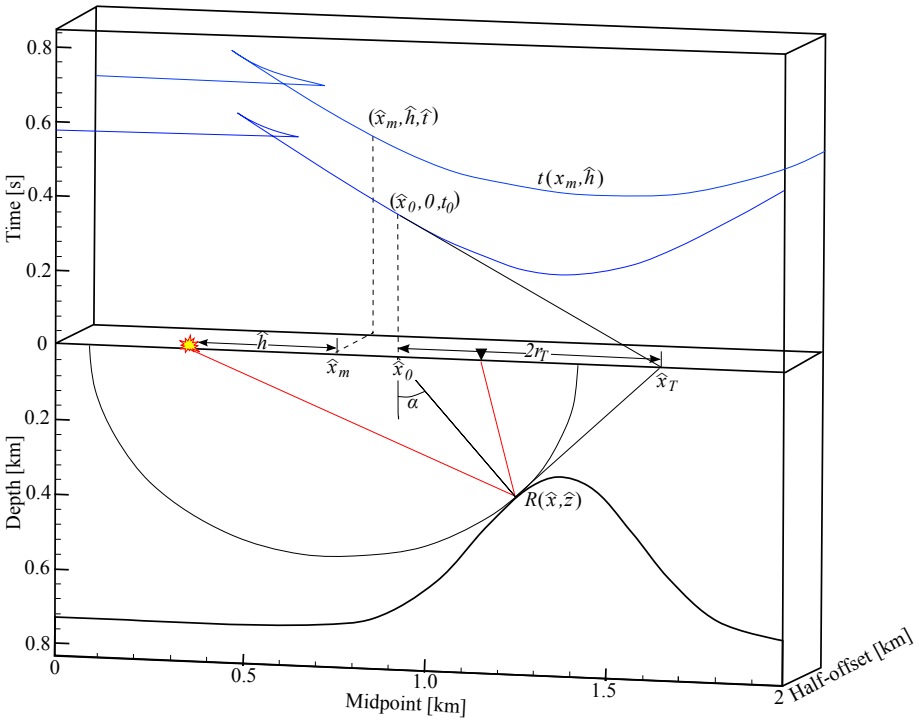

Figure 4.2: CO traveltime curves in (x_m, h, t) space for constant velocity model. The isochron of point $(\hat{x}_m, \hat{h}, \hat{t})$ is the darkgray ellipse that is tangent to the reflector at point R. The isochron of point $(x_0, 0, t_0)$ is a circle (not plotted) that is also tangent to the reflector at point R Höcht et al. [1999].

associated CO traveltime curve at $\hat{t}$ is also known, the depth domain coordinates of the corresponding reflection point $R = (\hat{x}, \hat{z})$ are obtained simply replacing (x_m, h, t, t') with $(\hat{x}_m, \hat{h}, \hat{t}, \hat{t}')$ in Equations 4.2 and 4.3. The first derivative of the CO isochron at $R = (\hat{x}, \hat{z})$ provides the tangent and, perpendicular to it, the normal to the reflector at point $R = (\hat{x}, \hat{z})$. Their intersections with the x-axis at $z = 0$ (i.e. the ground surface) are denoted in Figure 4.2 as x_T and x_0 respectively. The distance between these two points reads:

$$x_0 - x_T = 2r_T = \frac{\hat{t}^{\,2} - \left(\frac{2\hat{h}}{v}\right)^2}{\hat{t}\hat{t}'} \tag{4.4}$$

This distance only depends on the location $R = (\hat{x}, \hat{z})$ and on the orientation of the reflector at $R = (\hat{x}, \hat{z})$. Consequently, r_T is independent of the chosen point $(\hat{x}_m, \hat{h}, \hat{t}, \hat{t}')$ on the CO gathers but it represents a characteristic quantity of the reflection point $R = (\hat{x}, \hat{z})$. It is fully determined from a single point on the reflection event $(\hat{x}_m, \hat{h}, \hat{t}, \hat{t}')$ and the corresponding slope $\hat{t}'$ of the CO curve at this point.

The normal of the ellipse at R coincides with the normal incident ZO ray, i.e. the ray associated to a ZO experiment (see Figure 4.2). Its intersection with the measurement surface, which is the location $(x_0, 0)$ of the coincident shot-receiver pair, produces (see

Figure 4.2):

$$x_0 = \hat{x}_m - r_T \sqrt{\left(\frac{\hat{h}}{r_T}\right)^2 + 1} \tag{4.5}$$

while the square of its associated ZO reflection time reads:

$$t_0^2 = 2 \frac{\hat{t}^2 - \left(\frac{2\hat{h}}{v}\right)^2}{1 + \sqrt{\left(\frac{\hat{h}}{r_T}\right)^2 + 1}} \tag{4.6}$$

Equations 4.5 and 4.6 establish a general relationship between the point $(\hat{x}_m, \hat{h}, \hat{t})$ on a CO section and the point $R = (\hat{x}, \hat{z})$. It is therefore possible to establish a general relationship between the point $(\hat{x}_m, \hat{h}, \hat{t})$ and the location of the reflection events in other CO sections that pertain to the same $R = (\hat{x}, \hat{z})$ (i.e. with the same ZO ray):

$$x_m - r_T \sqrt{\left(\frac{h}{r_T}\right)^2 + 1} = \hat{x}_m - r_T \sqrt{\left(\frac{\hat{h}}{r_T}\right)^2 + 1} \tag{4.7}$$

$$\frac{t^2 - \left(\frac{2h}{v}\right)^2}{1 + \sqrt{\left(\frac{h}{r_T}\right)^2 + 1}} = \frac{\hat{t}^2 - \left(\frac{2\hat{h}}{v}\right)^2}{1 + \sqrt{\left(\frac{\hat{h}}{r_T}\right)^2 + 1}} \tag{4.8}$$

Equations 4.7 and 4.8 describe in the (t, x_m, h) data volume the CRP traveltime associated to the reflection point $R = (\hat{x}, \hat{z})$ as a function of initial values $(\hat{x}_m, \hat{h}, \hat{t})$, without need of explicitly knowing the coordinates of the reflection point R. Choosing as initial values $\hat{x}_m = x_0$, $\hat{h} = 0$ and $\hat{t} = t_0$, (i.e. the coordinate of corresponding ZO or normal ray) provides:

$$x_m(h) = x_0 + r_T \sqrt{\left(\frac{h}{r_T}\right)^2 + 1} - 1 \tag{4.9}$$

$$t^2(h) = 4\frac{h^2}{v^2} + \frac{1}{2} t_0^2 \left(\sqrt{\left(\frac{h}{r_T}\right)^2 + 1} - 1 \right) \tag{4.10}$$

with:

$$2\, r_T = \frac{t_0}{t'_0} \tag{4.11}$$

Using the horizontal slowness, also called the ray parameter $p = \frac{t'_0}{2} = \frac{\sin\alpha}{v}$ Equation 4.11 becomes:

$$2\, r_T = \frac{v}{2} \frac{t_0}{\sin\alpha} \tag{4.12}$$

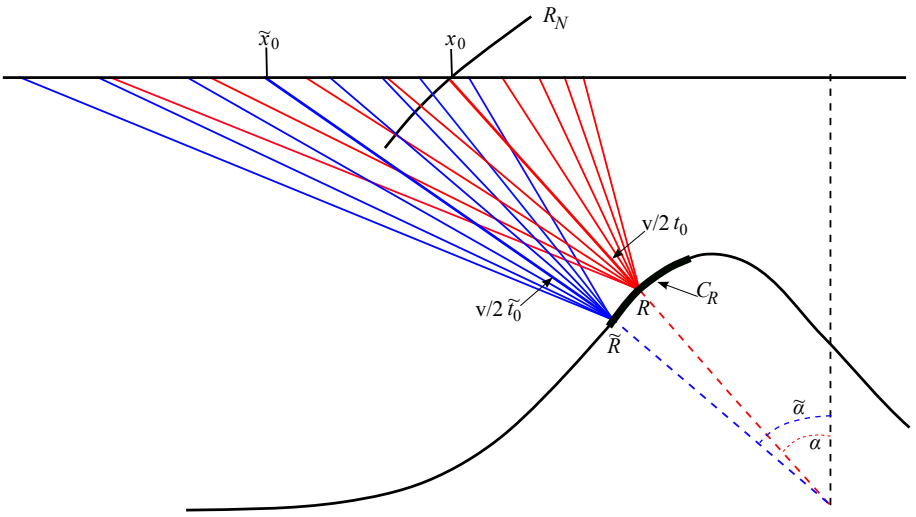

Figure 4.3: Constant velocity model: illumination of point $\tilde{R}$ and point R both located on the circle C_R, centred at point R with radius of curvature R_R [Höcht et al., 1999].

being α the emergence angle of the ZO ray measured with respect to the surface normal; it coincident with the local reflector dip measured with respect to the surface $z = 0$.

4.3.2 CRS stack for homogenous medium

As shown, in a homogeneous medium the CRP traveltimes in the (t, x_m, h) domain can be evaluated by the pair (t_0, x_0) associated to the corresponding ZO ray (Equations 4.9 and 4.10). Consequently, the CRP traveltimes associated to the reflection points located around a considered central reflection point R can be evaluated by the twt $\tilde{t}_0$ and the emergence location $\tilde{x}_0$ of their corresponding ZO rays. For the ideal subsurface of Figure 4.2, using simple geometrical considerations it is possible to express the ZO traveltime $\tilde{t}_0$ and the emergence location $\tilde{x}_0$ of the ZO ray associated to an arbitrary point $\tilde{R}$, as a function of the emergence location x_0 and emergence angle α of the ray that connects the surface location of the coincident shot/receiver pair with the reflection point R (see Figure 4.3):

$$\tilde{x}_0(\tilde{\alpha}) = x_0 + R_N(\cos\alpha \tan\tilde{\alpha} - \sin\alpha) \tag{4.13}$$

$$\tilde{t}_0(\tilde{\alpha}) = t_0 + \frac{2}{v} R_N \left(\frac{\cos\alpha}{\cos\tilde{\alpha}} - 1\right) \tag{4.14}$$

being $\tilde{\alpha}$ the emergence angle of the ZO ray associated to the arbitrary point $\tilde{R}$, and R_N the radius of curvature that changes along the ZO ray according to the so-called transmission law for wavefront curvature [Hubral and Krey, 1980]. This is also known as spherical divergence or geometrical spreading:

$$R_N = R_R + \frac{v}{2} t_0 \tag{4.15}$$

Therefore, provided that α and R_R (i.e. the radius of curvature of the arc segment C_R) are known, it is possible to determine the ZO location $\tilde{x}_0$ and ZO traveltime $\tilde{t}_0$ for an

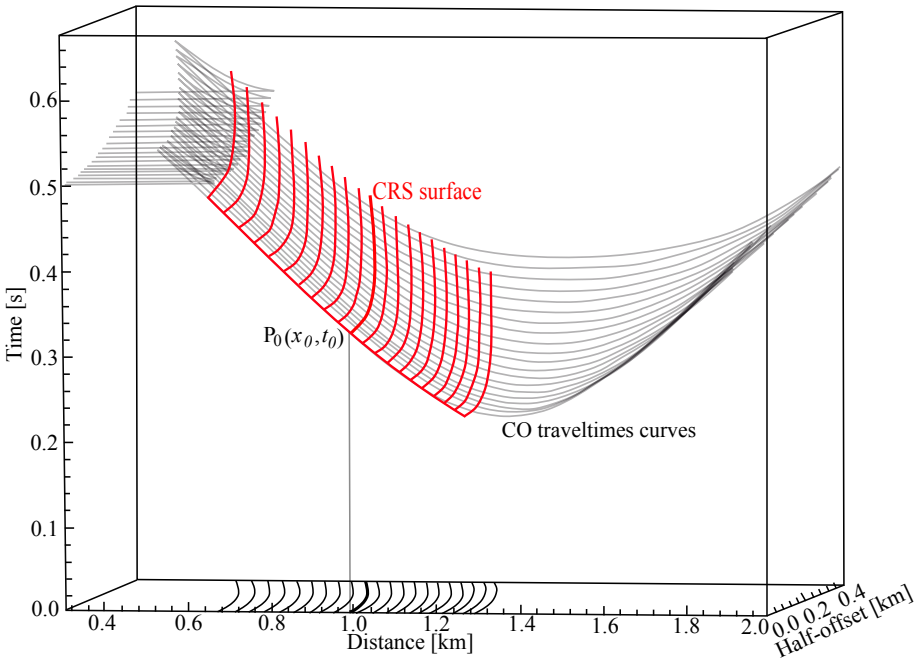

Figure 4.4: 3-D data space representing the CRS surface. The CRS stack surface is constructed with the CRP traveltimes (dark gray) of the circular reflector of Figure 4.4. The ZO travel time curve for the circle C_R is depicted in black [Höcht et al., 1999].

arbitrary point $\tilde{R}$ specified on the circle C_R by the angle $\tilde{\alpha}$. The corresponding CRP traveltime in the (t, x_m, h) data volume is obtained by replacing x_0, t_0 and r_T with $\tilde{x}_0, \tilde{t}_0$ and $\tilde{r}_T$ in Equations 4.9 and 4.10:

$$\tilde{x}_m(\tilde{\alpha}, h) = \tilde{x}_0(\tilde{\alpha}) + \tilde{r}_T \left(\sqrt{\frac{h^2}{\tilde{r}_T^{\,2}(\tilde{\alpha})} + 1} - 1 \right) \tag{4.16}$$

$$\tilde{t}^{\,2}(\tilde{\alpha}, h) = 4\,\frac{h^2}{v^2} + \frac{1}{2}\,\tilde{t}_0(\tilde{\alpha}) \left(\sqrt{\left(\frac{h^2}{\tilde{r}_T^{\,2}(\tilde{\alpha})} \right) + 1} - 1 \right) \tag{4.17}$$

with:

$$\tilde{r}_T(\tilde{\alpha}) = \frac{v}{4}\frac{\tilde{t}_0(\tilde{\alpha})}{\sin\tilde{\alpha}} \tag{4.18}$$

Varying the emergence angle $\tilde{\alpha}$ of the ZO ray associated to the arbitrary point $\tilde{R}$ provides the CRP traveltimes associated to all the points of the considered arc of reflector, namely the corresponding CRS stack surface in the (t, x_m, h) data volume (Figure 4.4).

The previous relations can be expressed in term of wavefield attributes through the waves of two hypothetical one-way experiments. One experiment is obtained by placing a fictitious point source at R. A portion of the resulting circular wavefront emerging at x_0 with radius of curvature $R_{NIP} = t_0 \frac{v}{2}$ is depicted at different instants of time in Figure 4.5. As the ZO ray is normal to the reflector at R, this is referred as the normal-incidence-point (NIP) wave [Hubral, 1983]. The second experiment is obtained assuming an exploding reflector model for circle C_R, which yields the hypothetical circular wavefront emerging at x_0 with radius of curvature R_N (Figure 4.5). As all rays

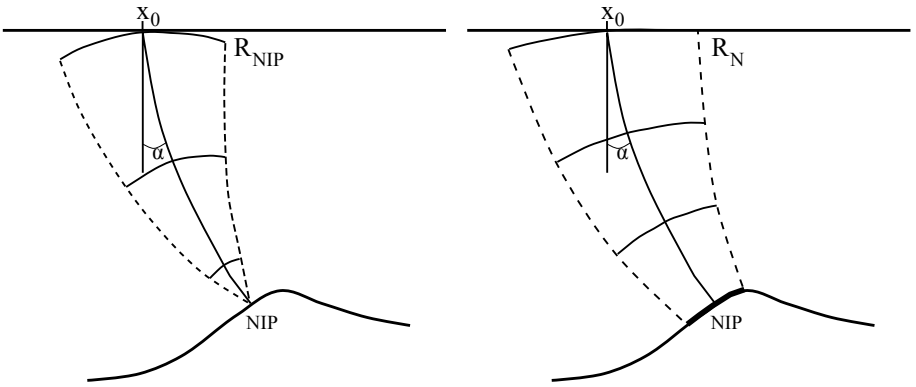

Figure 4.5: Physical interpretation of the CRS stacking parameters for a constant velocity model. The angle of emergence α, defines the angular orientation of the CRS (blue colour). The radius of curvature of the NIP-wave (a) gives the distance from the NIP to the surface, while the radius of curvature of the N-wave (b) is a measure for the CRS curvature.

are perpendicular to the reflector segment the resulting wave is called normal (N) wave [Hubral, 1983]. Both waves emerge at x_0 on the ground surface at time $t_0/2$ with an angle α coincident with the emergence angle of the ZO ray. with these wavefield attributes Equations 4.13 and 4.14 read:

$$\tilde{x}_0(\tilde{\alpha}) = x_0 + R_N(\cos\alpha \tan\tilde{\alpha} - \sin\alpha) \tag{4.19}$$

$$\tilde{t}_0(\tilde{\alpha}) = \frac{2R_{NIP}}{v} + \frac{2}{v}R_N\left(\frac{\cos\alpha}{\cos\tilde{\alpha}} - 1\right) \tag{4.20}$$

Therefore, the CRP traveltimes for homogeneous medium in term of wavefield attributes read:

$$x_m(\tilde{\alpha}, h) = \tilde{x}_0(\tilde{\alpha}) + \tilde{r}_T + \left(\sqrt{\frac{h^2}{\tilde{r}_T^2(\tilde{\alpha})} + 1} - 1\right) \tag{4.21}$$

$$t^2(\tilde{\alpha}, h) = 4\frac{h^2}{v^2} + \frac{2}{v^2}\tilde{R}_{NIP}^2(\tilde{\alpha})\left(\sqrt{\frac{h^2}{\tilde{r}_T^2(\tilde{\alpha})} + 1} + 1\right) \tag{4.22}$$

$$\tilde{r}_T(\tilde{\alpha}) = \frac{1}{2}\frac{\tilde{R}_{NIP}(\tilde{\alpha})}{\sin\tilde{\alpha}} \tag{4.23}$$

with:

$$\tilde{R}_{NIP} = R_{NIP}\left(\frac{\cos\alpha}{\cos\tilde{\alpha}} - 1\right) + R_{NIP} \tag{4.24}$$

Varying the angle $\tilde{\alpha}$ Equations 4.21 and 4.22 represent the ensemble of CRP traveltimes that, in a constant velocity medium, provide the kinematic reflection response of a circular reflector segment located at R, oriented by the emergence angle α and with radius of curvature $R_N - R_{NIP}$.

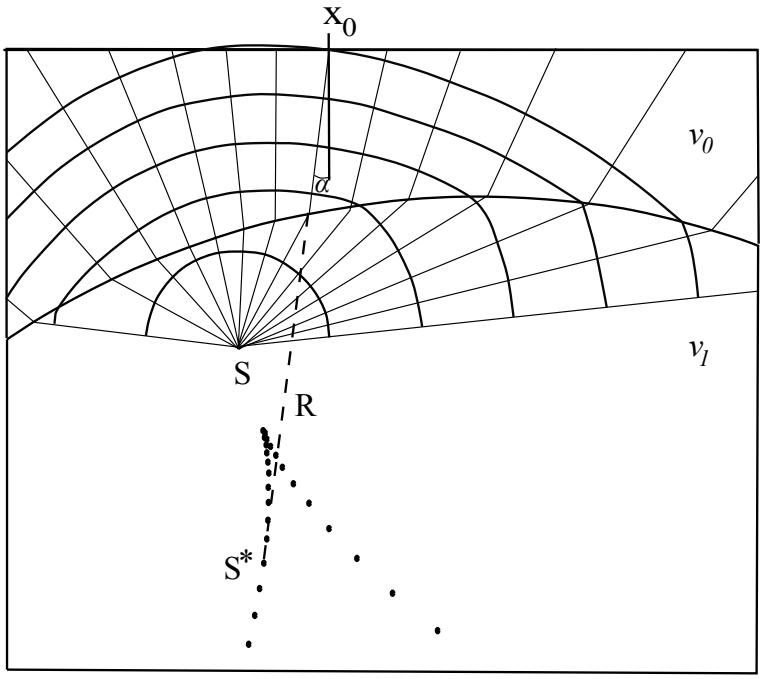

Figure 4.6: Model and image space: A point source at the object point S provides a wave shown in dark gray at different instants of time. The conjugate point S^* would be observed at x_0 on the ground surface. All conjugate points observed on the ground surface form a caustic (light gray points) [Höcht et al., 1999].

4.3.3 CRS stack for inhomogeneous medium

To an observer standing at the ground surface the light emitted by the point light source S shown in Figure 4.6, appears to be stemming from a point source located on the S^*, conjugate point of S. The location of the conjugate point $S^* = (x_0 - R\sin\alpha, R\cos\alpha)$ is defined by the emergence angle α and the radius of curvature R at x_0 of the wave that stems from the point source at S. Likewise, two hypothetical NIP- and N-waves with object point S_{NIP} and S_N would have their image points located respectively at S^*_{NIP} and S^*_N (see Figure 4.7). The image point S^*_N is determined assuming the centre of curvature S_N of the interface at S_{NIP} as object point, which is equivalent to assuming the exploding reflector segment around S_{NIP} as circular. This is a valid approximation since in the vicinity of the central ZO ray both the NIP- and N-waves fronts emerging at x_0 can be assumed to be circular. Accordingly, in a inhomogeneous medium with near-surface velocity v_0, a circular reflector segment placed at S_{NIP} with centre of curvature at S_N would yield wavefronts emerging at x_0 with the same emergence angle α and radii of curvature R_N and R_{NIP} of those that would be observed in a homogeneous medium with constant velocity v_0 for a circular reflector segment placed at S^*_{NIP} with centre of curvature at S^*_N (Figure 4.7). Obviously, the ZO traveltime $t_0/2$ of the NIP-wave from S_{NIP} to $(x_0, 0)$ in the real inhomogeneous medium will in general differ from the ZO traveltime $t^*_0 = R_{NIP}/v_0$ from S^*_{NIP} to $(x_0, 0)$ in the auxiliary homogeneous model.

In the auxiliary medium the traveltime difference between the traveltime t^*_0 for the coincident source/receiver pair at x_0 and the traveltime t for an arbitrary source/receiver pair associated with a ray that passes through S^*_{NIP} can be determined by means of

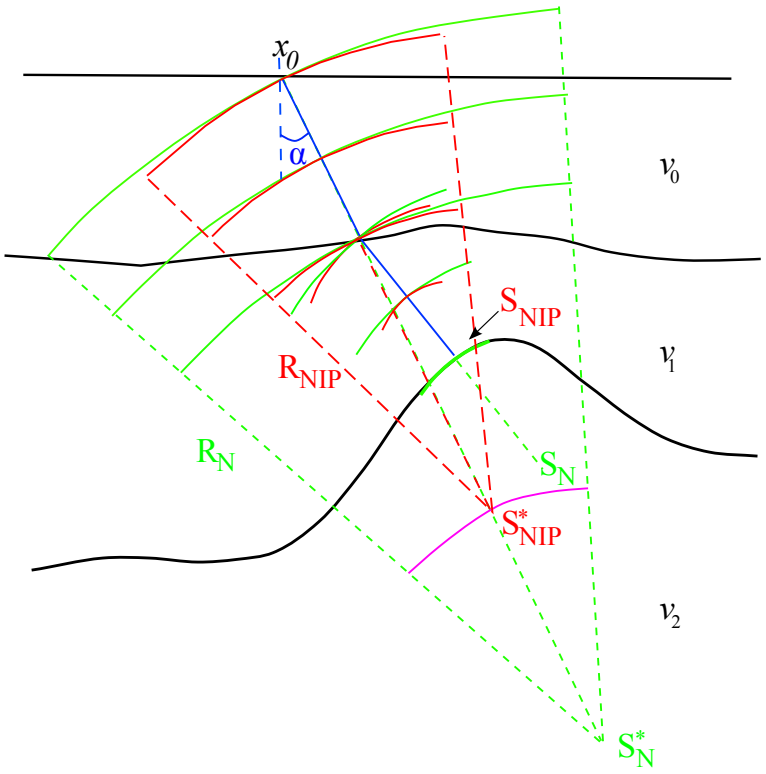

Figure 4.7: Model with object points S_{NIP} and S_N and their image points S^*_{NIP} and S^*_N provided by the radii of curvature of the NIP wave and the normal wave at x_0 on the surface. The radii of curvature of the NIP wave and the normal wave along the normal incident ray are plotted in red and green, respectively. [Mann, 2002].

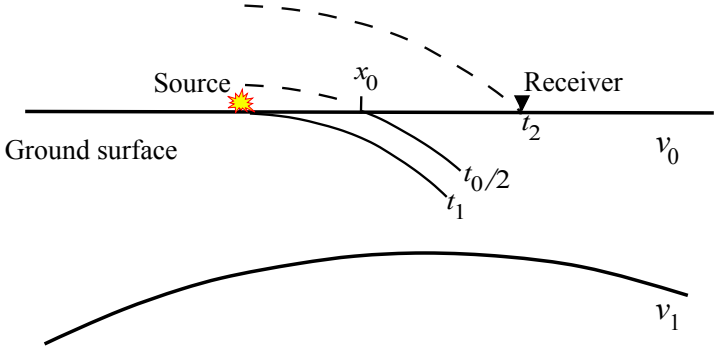

Figure 4.8: NIP wave at different instants of time [Höcht et al., 1999].

the instants of time t_1 and t_2 when the NIP wave emerges at source and receiver coordinates: $\Delta t = t - t_0 = t_1 - t_0/2 + t_2 - t_0/2$, i.e. it depends only on the medium through which the NIP wave passes in the time interval between $\min(t_1, t_0/2, t_2)$ and $\max(t_1, t_0/2, t_2)$ (Figure 4.8). For a circular wavefront the same traveltime difference applies to any shot/receiver pair of a inhomogeneous medium. Therefore, denoting $t(h)$ as the traveltime for an arbitrary shot/receiver pair passing through S_{NIP} in the real inhomogeneous model and t_I as the traveltime for an arbitrary shot/receiver pair passing

through S^*_{NIP} in the auxiliary homogeneous model, results:

$$t(h) - t_0 = t_I - \frac{2R_{NIP}}{v_0} \tag{4.25}$$

Hence:

$$t(h) = t_0 + t_I - \frac{2R_{NIP}}{v_0} \tag{4.26}$$

This equation synchronizes the traveltime $t(h)$ for the reflection point S_{NIP} of the actual medium with the traveltime t_I from the hypothetical reflection point S^*_{NIP} of the auxiliary medium. Accordingly, the CRP traveltime of the object point S_{NIP} in the inhomogeneous medium can be approximated with the time-delayed CRP traveltime of its image point S^*_{NIP} simply taking into account the time delay given by Equation 4.25:

$$x_m(\tilde{\alpha}, h) = \tilde{x}_0(\tilde{\alpha}) + \tilde{r}_T + \left(\sqrt{\frac{h^2}{\tilde{r}_T^2(\tilde{\alpha})} + 1} - 1 \right) \tag{4.27}$$

$$\left[t(\tilde{x}_0, h) - \left(t_0 - \frac{2}{v_0} R_{NIP} \right) \right]^2 = 4 \frac{h^2}{v_0^2} + \frac{2}{v_0^2} R^2_{NIP}(\alpha) \left(\sqrt{\frac{h^2}{\tilde{r}_T^2(\tilde{\alpha})}} \right) \tag{4.28}$$

where:

$$\tilde{r}_T = \frac{1}{2} \frac{\tilde{R}_{NIP}(\tilde{x}_0)}{\sin \alpha(\tilde{x}_0)} \tag{4.29}$$

Equations 4.27 and 4.28 approximate in a inhomogeneous medium the CRP trajectory associated to an arbitrary point $\tilde{R}$ located in depth on a curved reflector segment. The $\tilde{R}$ location with respect to emergence location x_0 of the ray normally reflected at the centre of the reflector segment is specified by the angle $\tilde{\alpha}$. The approximation is valid until the wavefronts in the vicinity of x_0 can be considered, with sufficient accuracy, circular. Varying the emergence angle $\tilde{\alpha}$ of the ZO ray associated to the arbitrary point $\tilde{R}$ provides the approximation of the CRP traveltimes associated to all the points of the considered arc of reflector, namely the corresponding CRS stack surface in the (t, x_m, h) data volume.

Despite its well-defined geometrical interpretation, the parametric representation of the CRS response provided by equations Equations 4.27 and 4.28 is very difficult to implement. Conversely, the Taylor expansions provide explicit functions of $(x_m - x_0)$ and h much easier to evaluate for each contributing trace. The second-order Taylor expansion of t^2, the so-called hyperbolic approximation, reads:

$$t^2_{hyp}(x_m, h) = \left[t_0 + \frac{2 \sin \alpha \, (x_m - x_0)}{v_0} \right]^2 + \frac{2 \, t_0 \cos^2 \alpha}{v_0} \left[\frac{(x_m - x_0)^2}{R_N} + \frac{h^2}{R_{NIP}} \right] \tag{4.30}$$

with the parameters as indicated in Table 4.1. In the (t, x_m, h) domain the traveltime 4.30 represents a hyperboloid with vertical symmetry axis and its apex located in the ZO section, shifted in time and midpoint with respect to x_0 and t_0 (Figure 4.9). This is also the operator employed by the CRS implementation used in this thesis [Mann et al., 1999].

t_0	twt of the normal (central) ray ($h = 0$).
x_0	emergence point coordinate of the normal (central) ray ($h = 0$).
h	half-offset between the source and receiver position.
$(x_m - x_0)$	midpoint displacement (midpoint aperture).
v_0	constant near-surface velocity.
α	emergence angle of the normal ray.
R_N	radius of curvatures of the hypothetical N-wave emerging at x_0.
R_{NIP}	radius of curvatures of the hypothetical NIP-wave emerging at x_0.

Table 4.1: CRS parameters of Equation 4.30.

4.4 Time domain CRS stacking parameters

The CRS operator in the time domain can be expressed through three independent stacking parameters (v_{NMO}, p, v_{CMO}) [Hertweck et al., 2007]:

$$t_{hyp}^2(x_m, h) = [t_0 + 2\,p(x_m - x_0)]^2 + \frac{h^2}{V_{NMO}^2} + \frac{(x_m - x_0)^2}{V_{CMO}^2} \tag{4.31}$$

where t_0 is the zero-offset traveltime, h represents the source-receiver offset, $(x_m - x_0)$ is the midpoint displacement from the central CMP gather under consideration, p is the horizontal slowness of the ZO reflected rays, V_{NMO} is the well-know normal-moveout velocity and V_{CMO} is a velocity parameter that depends on the reflector curvature (i.e. a curvature-moveout velocity).

Compared to the classical CMP traveltime, the two additional terms (p and V_{CMO}) take into account the difference in arrival times induced by the local slope and curvature of the reflector with respect to the traveltime of the image ray (see Figure 4.10). This difference must be taken into account to coherently stack the traces of neighbouring CMP gathers. In summary, the CRS stack operator uses:

- a parameter to define the curvature of events with respect to offset in the central CMP gather (the well-known NMO velocity V_{NMO});
- a parameter to define the slope of events at offset zero with respect to the midpoint coordinate (twice the horizontal slowness p);
- a parameter to define the curvature of events at offset zero with respect to the midpoint coordinate (the curvature moveout velocity V_{CMO}).

Developing and rearranging Equation 4.31 reads:

$$t_{hyp}^2(x_m, h) = \underbrace{\left[t_0^2 + \frac{h^2}{V_{NMO}^2}\right]}_{\text{NMO}} + \underbrace{\left[4\,t_0\,p(x_m - x_0) + 4\,p^2(x_m - x_0)^2\right]}_{\textit{Dip parameter}} + \underbrace{\left[\frac{(x_m - x_0)^2}{V_{CMO}^2}\right]}_{\textit{Curvature parameter}} \tag{4.32}$$

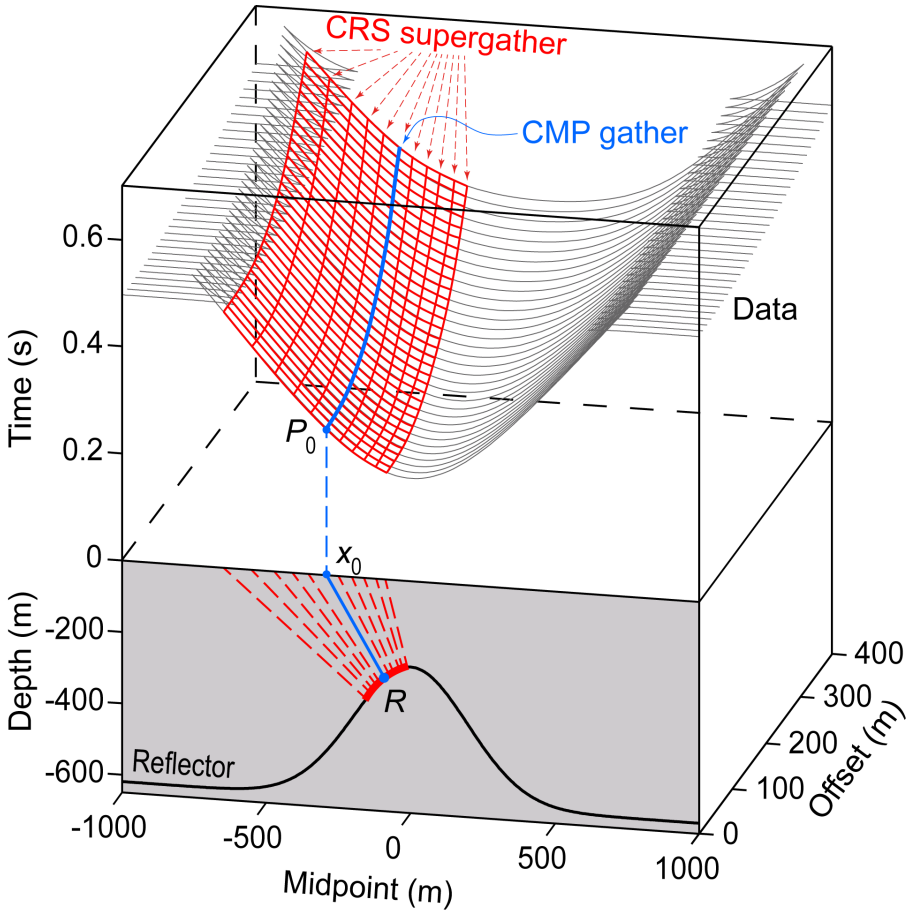

Figure 4.9: CRS stacking surface in the midpoint-offset domain for a 2D constant-velocity medium. The grey curves are the common-offset traveltimes for the subsurface reflector. The blue curve describes the traveltimes of source-receiver pairs with reflection points spread over the reflector segment R. The red curves are the traveltimes gathered at neighbouring midpoints around x_0 and represent the CRS supergather for all source receiver pairs with a reflection point in the reflector segment R. The CRS stack sums the data along the red surface and assigns the result to the point $P_0 = (x_0, t_0)$, where x_0 is the CMP coordinate and t_0 is the zero-offset traveltime. (Modified from Müller [1999]).

It is easy to recognize that Equation 4.32 does not provide a new stacking concept but just an extension of the conventional hyperbolic CMP stack into the midpoint direction to take into account the slope and the curvature of the reflection events in the ZO time section. As a matter of fact, assuming $(x_m - x_0)$, i.e. within the central CMP gather, Equation 4.32 reduces to the well-known CMP traveltime relation (Equation 3.1). Likewise, since that in a homogeneous medium for a planar horizontal reflector the horizontal slowness p of the ZO rays becomes 0 and the curvature move-out velocity parameter V_{CMO} is infinitely large, the corresponding slope and curvature terms can be neglected and the CRS traveltime formula reads exactly as the conventional CMP traveltime relation 3.1.

In the vicinity of x_0 the emergence location of the normal ray, the parameters in the

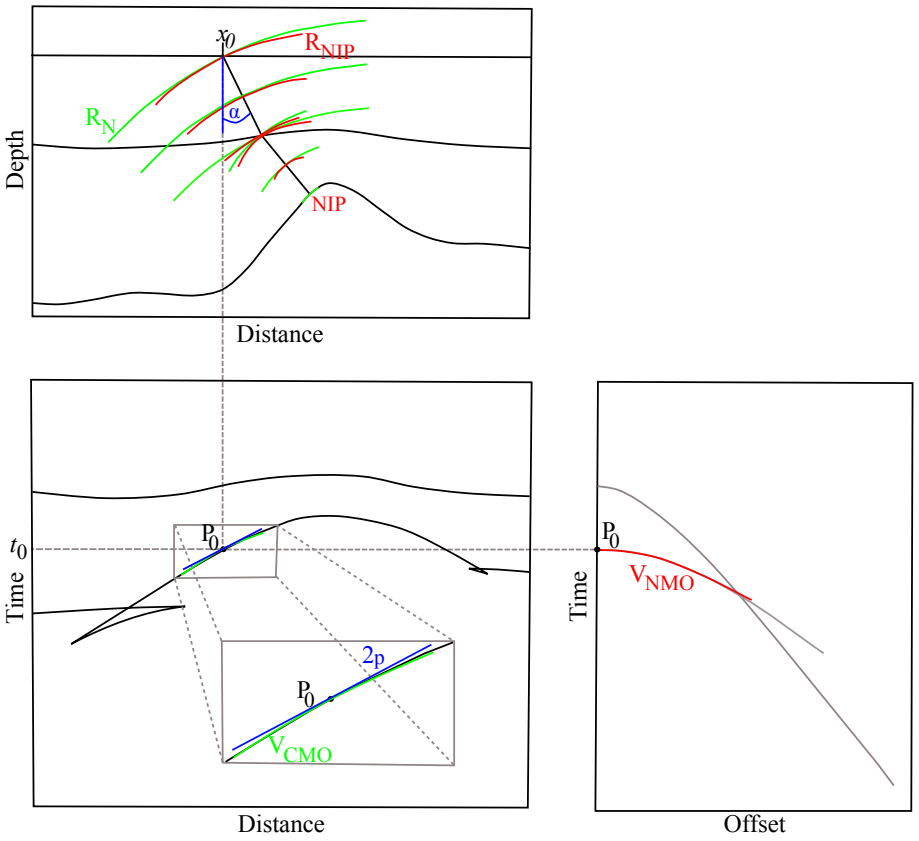

Figure 4.10: Subsets of the data space. ZO section (left) and CMP gather (right). Point $P_0(x_0, t_0)$ is the location of an event associated with the normal ray shown in the upper part. In this domain, the CRS stacking parameters are given by the curvature of the CMP event (red, V_{NMO}), the slope (blue, $2p$) and curvature (green, V_{CMO}) of the ZO event [Hertweck et al., 2007].

time domain are coupled with the parameters in the depth domain by the near-surface velocity v_0 [Hertweck et al., 2007]:

$$p = \frac{\sin\alpha}{v_0} \tag{4.33}$$

$$V_{NMO}^2 = \frac{2\,v_0\,R_{NIP}}{t_0\cos^2\alpha} \tag{4.34}$$

$$V_{CMO}^2 = \frac{v_0\,R_N}{2\,t_0\cos^2\alpha} \tag{4.35}$$

4.5 The pragmatic search approach

Since the locations of the reflection events in the ZO plane are initially unknown, to produce a ZO stacked section the CRS algorithm has to estimate for each point of the ZO section to be simulated the CRS attribute (α, R_{NIP}, R_N) triplet of the CRS stacking surface that best fits the (possible) reflection event. This is a nonlinear optimization

problem computationally very demanding whose solution requires efficient search strategies. The implementation used in this thesis is based on the so-called pragmatic search approach [Müller, 1999]. This strategy splits the initial 3-parameters search in three independent one-parameter searches which are then used as the starting points for a final local 3-parameters optimization, computationally less demanding.

The first one-parameter search is called automatic CMP stack. It consists of restricting Equation 4.30 to $(x_m - x_0) = 0$ to perform a sample-by-sample stacking velocity analysis in the resulting CMP gathers. Setting $(x_m - x_0) = 0$ Equation 4.30 becomes:

$$t_{hyp}^2(h) = t_0^2 + \frac{2\,t_0\,\cos^2\alpha}{v_0}\frac{h^2}{R_{NIP}} \tag{4.36}$$

and placing:

$$V_{NMO}^2 = \frac{2\,v_0\,R_{NIP}}{t_0\cos^2\alpha} \tag{4.37}$$

it further simplifies to:

$$t_{hyp}^2(h) = t_0^2 + \frac{4\,h^2}{V_{NMO}^2} \tag{4.38}$$

The stacking velocity resulting from the automatic CMP stack process is evaluated through the stacking velocity that yields the highest coherence value. Summation of prestack data along the corresponding stacking hyperbolas leads to the so-called automatic CMP stack section. This is also the domain used for the further research steps of the pragmatic search approach.

The second one-parameter search uses a zero-offset formulation of the CRS stacking operator obtained setting in Equation 4.30 the half-offset $h = 0$:

$$t_{hyp}^2(h) = \left[t_0 + \frac{2\,\sin\alpha}{v_0}(x_m - x_0)\right]^2 + \frac{2\,t_0\cos^2\alpha}{v_0}\cdot\left[\frac{(x_m - x_0)^2}{R_N}\right] \tag{4.39}$$

Since the resulting CRS operator depends on α and R_N, the one-parametric relation is obtained through the plane wave assumption $R_N = \infty$:

$$t_{hyp}^2(h) = \left[t_0 + \frac{2\,\sin\alpha}{v_0}(x_m - x_0)\right] \tag{4.40}$$

A semblance-based coherence analysis in the ZO section from the automatic CMP stack determines for each point (x_0, t_0) the emergence angle α which yields the highest coherence value. As Equation 4.40 defines a linear stacking operator in the ZO section, this procedure is called linear ZO stack. After that the initial values of V_{NMO} and α are estimated, the initial value of R_{NIP} can be computed through Equation 4.37:

$$R_{NIP} = \frac{V_{NMO}^2\,t_0\cos^2\alpha}{2\,v_0} \tag{4.41}$$

Known α and R_{NIP}, Equation 4.39 depends only on R_N. This is the last one-parameter equation of the pragmatic search approach, which is used to search in the ZO section

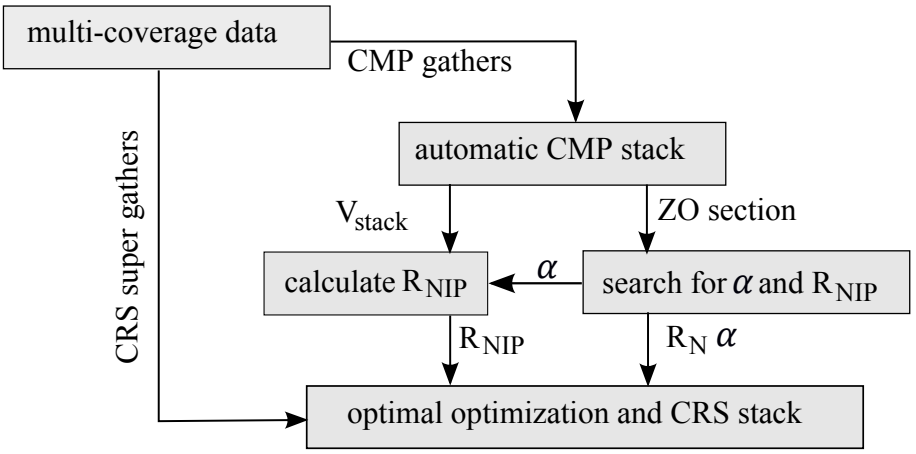

Figure 4.11: Simplified flowchart of the pragmatic search strategy. The indicated processing steps have to be performed for each ZO sample to be simulated [Mann, 2002].

produced by the automatic CMP stacked the initial value of R_N. As Equation 4.39 is a hyperbolic stacking operator, this step is called hyperbolic ZO stack.

The values from the three independent one-parameter searches, however, are not the best possible ones but just values close enough to the optimum ones. Therefore, they can be used as initial attributes for a local optimization process computationally much less demanding than the global one. The whole procedure, which is depicted in Figure 4.11, provides a final optimized CRS stack section together with a number of sections including optimized attribute and coherence (semblance) sections. It is implemented in a fully automatic way without any user interaction on the pre-stack data being necessary. However, since its implementation relies heavily on coherence measures, any kind of noise may negatively affect the attributes search procedure and, consequently, the stack results. Additionally the stacking of many traces may lead to alignment of spurious events without any correlation to the data (see Figures 4.12a and 4.12b). A-priori information to constrain the procedure should avoid unreliable stacking results. If these are not available, a careful comparison between the initial CRS results and the pre-stack data can help to choose the optimal CRS processing parameters.

4.6 Considerations

4.6.1 Apertures

The CRS operator is a traveltime relation approximated to the second order whose validity generally decreases when distances in midpoint and offset directions from the considered zero-offset location (x_0) are increased. Its implementation requires defining the correct amount of offset and midpoint displacements which render the approximation sufficiently valid. These are the so-called CRS apertures, which define the number of traces involved in the coherence analysis and stack process. Their definition affects the

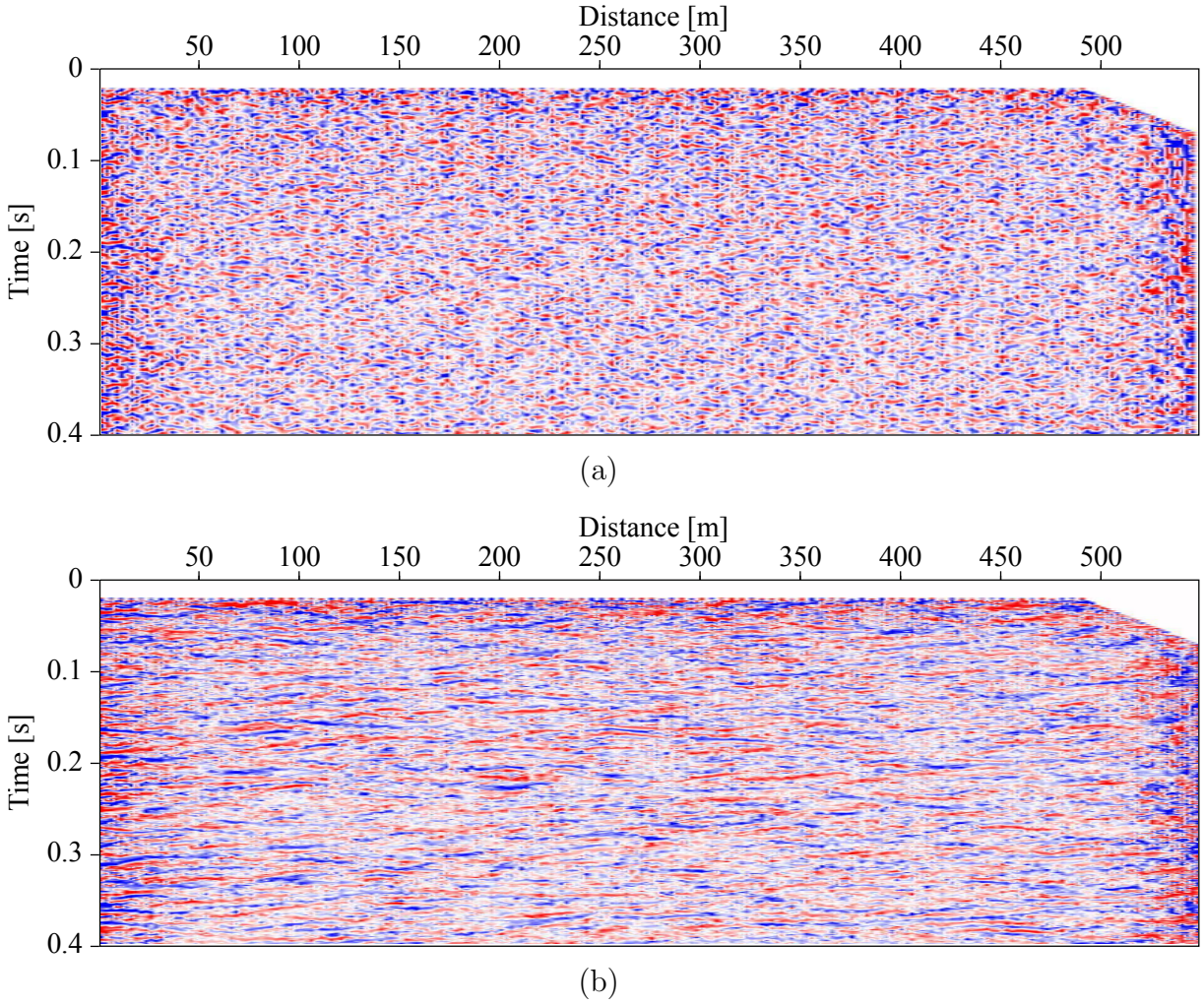

Figure 4.12: (a) Automatic CMP stacked section and optimized CRS stacked section (b) of a dataset containing gaussian random noise in the range of 15-250 Hz. The larger number of stacked traces used during the optimization gives rise to bogus alignments of noise which may lead to misinterpretations.

reliability with which the CRS attributes are estimated, as well as the seismic lateral resolution and the S/N ratio of the stacked section. If the CRS apertures are set too wide apart the second order traveltime approximation may no longer be valid and CRS stack operator will produce a decrease of lateral resolution. On the other hand, if the apertures are too small the number of contributing traces in coherence analysis may considerably decrease and, as a consequence, the reliability of the CRS parameter will liwewise decrease. Therefore, apertures choice is a crucial step in CRS processing. Trying different apertures and taking the ones that maximize the coherence analysis is not useful because the coherence analysis is very sensitive to the number of contributing traces. Therefore the results with different apertures size, i.e. different number of traces, are not comparable. The only solution is to perform some numerical tests based on user-defined criteria.

A valuable criterion in selecting the aperture in the offset direction is possible using the same offsets that would be used during the conventional CMP stack method. The

midpoint aperture size, instead, can be set equal to the size of the first projected Fresnel zone, which defines the portion of reflector from which most of reflected energy interferes constructively. Wider apertures will decrease the resolution, while smaller apertures will not increase the resolution. Mann [2002] expressed the radius of the projected first Fresnel zone in terms of the CRS wavefield attributes:

$$\frac{W_F}{2} = \frac{1}{\cos\alpha}\sqrt{\frac{v_0 T}{2\left|\frac{1}{R_N} - \frac{1}{R_{NIP}}\right|}} \tag{4.42}$$

but this cannot be used directly to estimate the midpoint aperture as it depends on CRS parameters initially unknown. An alternative way may be by using the more common relation [see e.g. Sheriff, 2002]:

$$\frac{W_F}{2} = \frac{v}{2}\sqrt{\frac{T^2}{4} + T\,t_0} \approx \frac{v}{2}\sqrt{T\,t_0} \tag{4.43}$$

which defines the projected first Fresnel zone for a mono-frequency wave of period T in a homogeneous medium of constant velocity v, as a function of the twt t_0. This of course describes an ideal situation, one somewhat removed from actual case conditions. However, as suggested by Mann [2002], Equation 4.43 can be used as a first guess for midpoint aperture. Then, the resulting CRS parameters can be used in Equation 4.42 to check if the size of midpoint aperture is similar to that used. If they are very different then it is probable that the midpoint aperture used was wrong and the CRS parameters non reliable; a new iteration of the CRS stacking process with better defined aperture would be wise. If instead they are similar, the CRS results can be considered reliable and no further iterations are required. In this way, the quality control of both stacked and coherence final sections allows one to find the best size regarding midpoint aperture.

The CRS algorithm implemented in this thesis approximates the first Fresnel zone width as:

$$\frac{W_F}{2} = \min\left[W_{F,max}, \frac{v_0 + (v_{max} - v_0)\dfrac{t_0}{t_{max}}}{2}\sqrt{2\,T t_0} + W_{F,min}\right] \tag{4.44}$$

where v_0 and v_{max} are respectively the minimum and maximum considered stacking velocity, T is the assumed dominant period of the signals, t_0 the considered twt and t_{max} the maximum considered twt. The corresponding midpoint apertures $W_{F,min}$ and $W_{F,max}$ have to be provided by the user, for example on the base of Equation 4.43. The resulting ZO aperture is an elliptical surface in the (x_m, h)domain (Figure 4.13).

4.6.2 The near-surface velocity

The CRS stacking operator of Equation 4.30 requires explicit knowledge of the near-surface velocity v_0 along the seismic line. For marine datasets this information is always available. For land datasets it might be more difficult to estimate, even more so when dealing with shallow and ultra shallow datasets. However, the exact knowledge of the

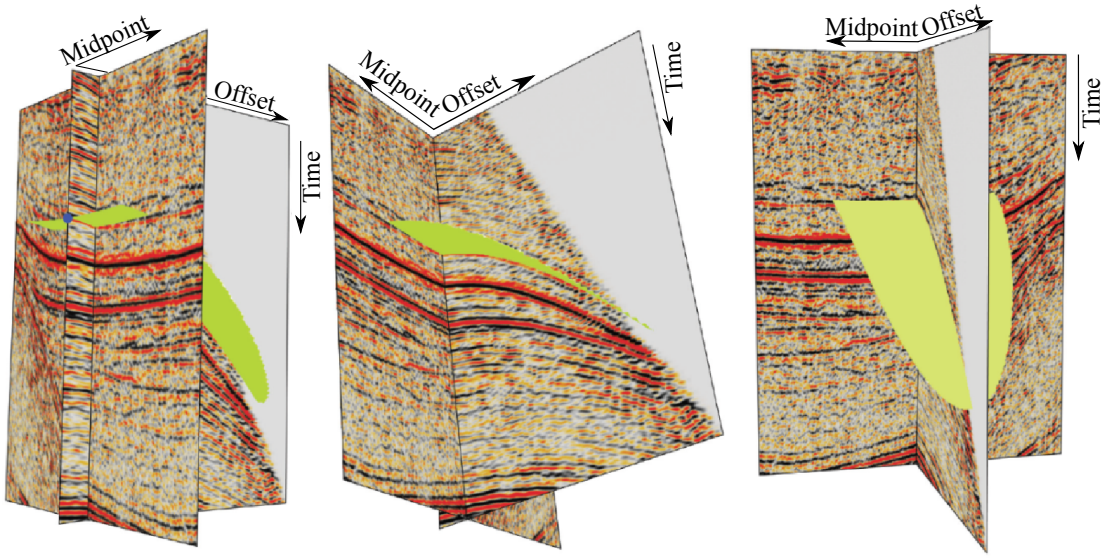

Figure 4.13: Tree different views of the CRS stacking operator for a selected ZO location [Hertweck et al., 2007].

near-surface velocity is not necessary for optimal CRS stack results. If the correct near-surface velocity value is available then the resulting CRS stacking parameters associated to reflection events are physically interpretable as the geometrical properties of a common reflection surface in depth. If, instead, the near-surface velocity v_0 is unknown the resulting CRS stacking parameters are simply the coefficients A, B and C of the hyperbolic surfaces $t^2 = (t_0 + A\Delta x_m)^2 + B\Delta x_m^2 + Ch^2$ that best fit the reflection event on the pre-stack data [see e.g. Baykulov et al., 2011]. Consequently, if the time imaging is the only aim of the CRS stack process, an erroneous v_0 in Equation 4.30 has no influence on the processing: any arbitrary value would provide the same CRS stacked results. If instead the CRS attributes must be used for further processing steps such as the NIP-wave tomography [Duveneck, 2004], then they must have a well-defined physical meaning. It is therefore necessary to provide a value close enough to the real near-surface velocity value.

Actually, the near-surface velocity also occurs in Equation 4.44 for the determination of the midpoint (i.e. ZO) aperture values, even if in this case its influence is minimal.

4.6.3 Nonstretch NMO

As shown in Chapter 3, undistorted NMO corrected reflection events would imply a systematic decreasing of V_{NMO} within the wavelet of the reflections. As shown by Mann and Höcht [2003], since the CRS determines the stacking velocity separately for each ZO sample in a completely data-driven way, the resulting stacking velocity function is not constant along neighbouring samples within the wavelet but decreases with increasing traveltime, exposing a characteristic "jig saw" appearance better suited to avoid the pulse stretch effect. As a consequence, the CRS stack method is a procedure able to

produce almost unstretched stacked results without necessitating any additional process. Conversely, the CRS parameters are almost constant within the same wavelet.

4.7 Velocity information from CRS attributes

The CRS stack can be considered as a generalized velocity analysis tool that provides kinematic information in the form of stacking attributes. Whenever the CRS operator fits well enough the traveltimes of the reflection events on the pre-stack data, the corresponding kinematic information have a well-established physical meaning and can be used to derive velocity information.

4.7.1 Stacking velocities

Stacking velocities can be expressed in term of CRS attributes α and R_{NIP} through Equation 4.37. Therefore, their estimation requires to extract from the corresponding attribute sections the optimized α and R_{NIP} values related to genuine reflection events. This can be done picking on the CRS-stacked section the reflection events from which the velocity information want to be derived. The high S/N ratio and the coherence section help in distinguishing them. The required α and R_{NIP} values are then derived from each picked (x_0, t_0) pair.

4.7.2 Interval velocities

Interval velocities may be evaluated from the CRS attributes through the so-called NIP-wave tomography, which is an inversion method to determine a smooth depth velocity model from the CRS attributes [Duveneck, 2004]. This method is based on the NIP-wave theorem [Hubral and Krey, 1980], which states that up to the second order the rays connecting sources and receivers on the measurement surface with a common reflection point are geometrically identical to the rays of a hypothetical emerging wave generated by a point source placed at the corresponding CRP (Figure 4.14). If the CRP coincides with a normal incident point, i.e. the reflection point associated to a ZO ray, then such a wave is called NIP-wave. Accordingly, a velocity model can be considered consistent with the data if all NIP-waves focus at zero traveltime after their back-propagation. This implies that the R_{NIP} values become zero at $t_0/2 = 0$.

The input for the NIP-wave tomography inversion process consists on a number of sparse picked points in the CRS stacked section related to genuine reflection events. From each picked point (x_0, t_0) the CRS attributes R_{NIP} and α, i.e. the radii of curvature and the emergence angle of the hypothetical NIP-wave, are extracted from the corresponding CRS attribute sections. Actually, for practical purposes the inversion rather than R_{NIP} and α assumes the second spatial derivative of the traveltime of the NIP wave at x_0 and

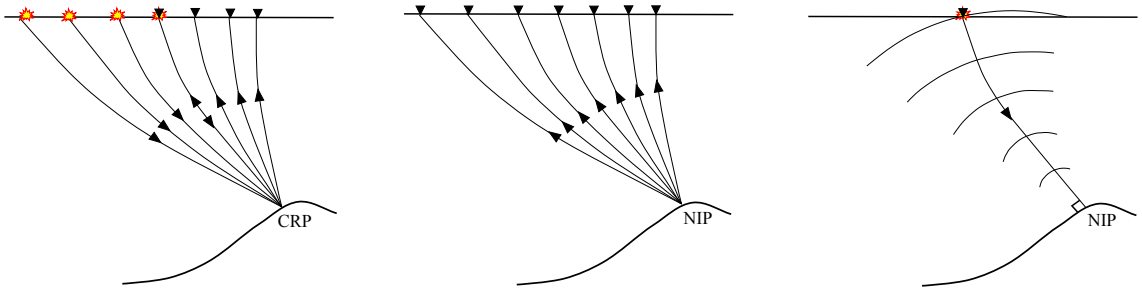

Figure 4.14: Ray trajectories associated with a CRP and NIP points. (a) Ray segments of specular rays reflect at a CRP in the subsurface. (b) Geometrically, ray trajectories associated with a hypothetical wave due to a point source at the NIP coincide with the CRP ray segments. (c) In a consistent velocity model, the NIP-wave focuses at the NIP at zero traveltime, when they are propagated back into the subsurface.

the horizontal component of the slowness vector, respectively:

$$M_{NIP} = \frac{\cos^2 \alpha}{v_0 R_{NIP}} \tag{4.45}$$

$$p = \frac{\sin \beta_0}{v_0} \tag{4.46}$$

The input data vector is then:

$$\tilde{\mathbf{d}}_{\mathbf{obs}}(t_0/2, M_{NIP}, p, x)_i \quad \text{for} \quad i = 1, \ldots, N \tag{4.47}$$

where N is a number of picked data points.

In principle, once the input data $\tilde{\mathbf{d}}_{\mathbf{obs}}$ are determined it is possible to find the correct velocity model simply using the focusing properties of NIP-waves for all picked data points. However, these must be expected to be affected by noise or measurement errors which may lead to a destabilization of the inversion process. Accordingly, prior to the inversion process they must be checked for the presence of outliers, multiples and other noise and if necessary edited. In addition, since the picked NIPs data are extracted from a time image section, their true subsurface locations (x_0, t_0) as well as the associated local dip θ_{NIP} (see Figure 4.15) are initially unknown. Consequently, these quantities need to be considered as additional model parameters to be determined together with velocity distribution. The velocity model is described in terms of B-Spline coefficients for each point of a grid with n_x and n_z nodes in the horizontal and vertical directions respectively:

$$v(x, z) = \sum_{j=1}^{n_x} \sum_{k=1}^{n_z} v_{jk} \beta_j(x) \beta_k(z) \tag{4.48}$$

being $\beta_j(x)$ and $\beta_k(z)$ the B-spline basis functions. Therefore, the aim of the inversion process is to find a model vector $\tilde{\mathbf{m}}$:

$$\tilde{\mathbf{m}}[(x, z, \theta_{NIP})_{i=1}^{n}, v_{jk}] \tag{4.49}$$

that minimizes in a least-squares sense, the cost function 4.50 between the picked data

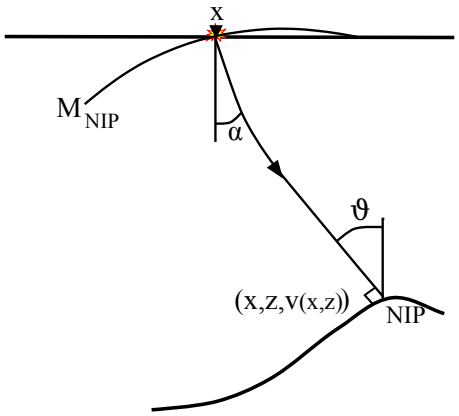

Figure 4.15: Data and model components for the NIP-wave tomographic inversion.

vector $\tilde{\mathbf{d}}_{\mathbf{obs}}$ and the forward-modelled data vector $\tilde{\mathbf{d}}_{\mathbf{m}} = f(\tilde{\mathbf{m}})$, having defined with f a nonlinear operator symbolizing the dynamic ray tracing:

$$S(\tilde{\mathbf{m}}) = \frac{1}{2}\left|\tilde{\mathbf{d}} - \tilde{\mathbf{d}}_{\mathbf{m}}\right|_D^2 \tag{4.50}$$

This is an ill-posed problem as the data space does not contain sufficient information to uniquely determine all model parameters. Its regularisation is obtained by imposing the velocity model of having minimum second derivatives, namely limiting the roughness of the velocity distribution. This is a reasonable constraint, since the smooth model is the simplest one that explains the data. To apply the mentioned constrains, a term depending on the B-spline coefficients is added to the cost function:

$$S(\tilde{\mathbf{m}}) = \frac{1}{2}\left|\tilde{\mathbf{d}} - \tilde{\mathbf{d}}_{\mathbf{m}}\right|_D^2 + c\,(v_{jk}) \tag{4.51}$$

where $c\,(v_{jk})$ is a measure for the model smoothness that has to be provided during the inversion process.

The inversion algorithm starts from an initial velocity model which can be described by a constant gradient model $V(z) = v_0 + g\,z$, where v_0 is the near-surface velocity, g the velocity gradient and z the depth. Any other available a priori velocity information can be used to constrain the initial velocity model. After that, kinematic ray tracing in the downward direction for each of the picked data points in the starting velocity model is performed. This yields the initial elements of vector $\tilde{\mathbf{m}}[(x, z, \theta_{NIP}), v_{jk}]$. Using these values, dynamic ray tracing in the upward direction is then performed until the rays reach the measurement surface to obtain the elements of model vector $\tilde{\mathbf{d}}_{\mathbf{m}} = f(\tilde{\mathbf{m}})$. Then the cost function is calculated using Equation 4.51 to describe the misfit between picked and modelled data. The linear system of equation is solved by using the least-square inversion method and the model update vector is obtained. The current model $\tilde{\mathbf{m}}$ is updated, and the forward dynamic ray tracing is repeated using the new model. If the cost function increases, the model update vector decreases, and the cost function is recalculated; otherwise, a next iteration is started. The inversion process is stopped when the data misfit reaches the specified minimum, or when the given maximum number of iterations is reached, or when the minimum of the cost function is found. The

characteristic decrease of the model update vector during the inversion has the effect of the determination of the long-wavelength features during the first iterations, while more and more details can be resolved in further iterations.

4.8 Residual static corrections from CRS attributes

The residual static corrections may be evaluated from the kinematic wavefield information derived from the CRS stack process through the so-called CRS-based residual static correction method [Koglin et al., 2006]. This is a surface-consistent linear traveltime inversion technique, which determines the static shifts on the basis of the summation of the cross-correlation results between CRS stacked traces and corresponding prestack moveout corrected traces, namely the traces within the corresponding CRS-supergather. Since the number of traces falling into the CRS-supergather can significantly exceed the number of traces belonging to one CMP gather, for each source/receiver location the number of contributing cross-correlation results is generally much larger than provided by conventional CMP-based residual static correction methods.

Like all residual static correction techniques, the CRS-based residual static correction method alos performs an initial NMO-correction so that the reflection events in each gather can be considered to be misaligned due to the residual static shifts. Using the CRS attributes (α, R_{NIP}, R_N) derived by a previous implementation of the CRS stack, the moveout-corrected CRS supergathers are obtained for each ZO trace by:

$$t_{moveout-corr}(x_m, h) = t_{hyp}(x_m, h) - t_0 \tag{4.52}$$

The single prestack moveout corrected traces are then cross-correlated with the corresponding CRS stacked and the resulting cross-correlation results are sorted and then stacked for common source and common receiver gathers. Assuming static shifts randomly distributed around zero, this stack process should cancel out all contributions which are not related to the considered surface location, enhancing only the ones related to the same surface location. The implicit assumption is that the structural component M_k in moveout in Equation 3.15 vanishes, as the CRS operator already accounts for the subsurface structures by means of the wavefield attribute R_N. The twts of the maximums in the cross-correlation stack results can therefore be assumed to be the residual static time shifts of the corresponding source/receiver locations. Once derived, the static correction for each prestack trace is simply the sum of the corresponding source and receiver estimated static values.

The whole procedure can be summarized through the following steps:

- initial NMO-correction;
- cross-correlation between single prestack moveout-corrected traces within a supergather and corresponding CRS stacked traces;
- sorting of cross-correlation results for common source receiver location;

- stack of cross-correlation results for common source receiver location;
- searching for the maximums of the cross-correlation stacks results for each common source receiver location;
- coupling of maximums of the cross-correlation stacks results to residual static;
- application of residual time shifts to initial traces.

This process repeated for all the ZO stacked traces provides surface-consistent residual static corrections in a one-step optimization, without solving any inverse problem. Being an iterative procedure, if the initial results are not satisfactory the whole process can be repeated including or excluding a new CRS stack process. This process is therefore very similar to the stack power maximization method proposed by Ronen and Claerbout [1985].

4.9 Event-consistent smoothing of CRS attributes

The data-driven CRS stack determination of kinematic attributes is expected to produce outliers, fluctuations and wrong automatic picks, especially for noisy, low fold and/or very complicated areas. To improve the final stack results and before using the derived attributes for other CRS-based processes, these unwanted results must be removed through an appropriate smoothing process. This should smooth the CRS parameters in an event-consistent manner, namely preserving their local proprieties without mixing any feature related to different events.

As discussed by Mann and Höcht [2003], the CRS kinematic wavefield attributes have the relevant advantage to be virtually constant along the seismic wavelet and to vary smoothly along the reflection event, as this is related to an emerging continuous wavefront. Accordingly, they can be smoothed without losing their local properties. Additionally, the emergence angle α and the coherence value at every ZO sample enable to smooth the attributes along the reflection events without the need to explicitly identify them. Accordingly, the smoothing process can be implemented in an automated manner without the need of time consuming manual detection of reflection events.

The event-consistent smoothing algorithm employed in this thesis acts following certain steps:

- For every ZO sample $P(x_0, t_0)$ a parallelogram-shaped smoothing window of user-defined size is adopted, centred around P and aligned with the reflection event (the emergence angle α). In time direction, the smoothing window should not be larger than the wavelet of the considered event in order to not mix valuable information with noise or information related to different coherent events. In the spatial directions, it should be restricted to a few traces (depending on the midpoint spacing) in order to avoid overlay strong variations of the wavefield attributes. The size of the smoothing window controls the smoothing effect;

- a coherence threshold is applied to reject the samples within the smoothing window with unreliable and/or unphysical attributes;
- a coherence threshold is applied to reject the samples within the smoothing window with an emergence angle value that differ from the emergence angle of the central sample with a value higher than the adopted threshold;
- any possible outliers in the attributes associated to remaining samples are removed applying a median filter. The selected attribute values are then averaged and assigned to the considered ZO sample $P(x_0, t_0)$.

These steps once repeated for all ZO samples in the CRS stack results yield the sections of smoothed kinematic wavefield attributes that substitute the original unsmoothed attribute sections in further processing.

Chapter 5

First example: P-wave dataset*

As a first example I will present a P-wave dataset collected to support a hydrogeological study conducted in a paleolake environment situated near Cagliari, in southern Sardinia, Italy (see Figure 5.1). The aim of the survey was to delineate the spatial extent of the multilayer aquifer and of its confining units, in order to outline the hydrogeological framework of the area. The available information concerning the geology of the area suggests the presence of silty and clayey deposits of marshy origin in the first 15–20 meters, and of a thick blanket of Miocene marl interbedded with sandstone up to 200-250 meter depth which precedes the Paleozoic basement composed of granitic rocks. The acquisition parameters were chosen according to this preliminary information, but the limited number of available channels brought about the enforced use of a maximum offset too small compared to the planned depth of observation (about 200-250 m). This inevitably introduced small moveout curvatures and consequently uncertainties during the velocity analysis. To overcome this limit of the acquisition it was necessary to perform a detailed CMP-by-CMP stacking velocity analysis with different velocity analysis techniques iteratively run together several times before imaging with good coherency and lateral continuity the many recorded reflection events. This required a great deal of time. Conversely, the CRS processing of the same pre-processed data set, including smoothing of CRS parameters and residual static corrections, took less than half hour on a standard personal computer. It provided, almost immediately, similar results without any preliminary explicit velocity analysis having been made.

5.1 Data acquisition and preprocessing

The P-wave data were acquired along a line 630 m long using a standard CMP roll-along technique in an end-on configuration with 24 active 50-Hz vertical receivers attached to a 24-channel EG&G Geometrics ES2420 seismograph with 14-bit A/D conversion, using a near offset of 25 m. A 0.15-kg explosive source was buried at approximately 2 m depth

*This example has been published under the following citation: Deidda G.P., Battaglia E., Heilmann Z., 2012, Common-reflection-surface imaging of shallow and ultrashallow reflectors: Geophysics, 77, B177-B185.

Figure 5.1: Site map indicating the location of the field site and the position of the seismic line.

Seismograph	24-channel EG&G Geometrics ES2420
Energy source	0.15-kg explosive
Receivers	24 50-Hz geophones
Receiver spacing	5 m
Shot spacing	5 m
Spread geometry	off-end
Number of shots	99
Minimum offset	25 m
Maximum offset	140 m
Record length	500 ms
Sampling interval	0.5 ms
Number of CMPs	220
CMP spacing	2.5 m
Maximum CMP fold	12
Line length	550 m

Table 5.1: Equipment and parameters used during the acquisition.

for each shot position. Both geophone and source spacing of 5 m provided twelvefold CMP coverage (see Figure 5.2) with a CMP spacing of 2.5 m. An analog 50-Hz low-cut filter was used to attenuate the ground roll, which had been recorded as having very high amplitudes at this site in a preliminary walkaway noise test. All acquisition and equipment parameters are reassumed in Table 5.1.

Four representative field records are shown in Figure 5.3. In addition to the typical ground roll, several clear reflections can be observed in each record. The spectral content of the recorded data ranges from about 20 to 300 Hz at near offsets, and up to 180 Hz at far offsets (see Figure 5.4). Peak amplitudes fall between 20–40 Hz and belong to ground roll, while the dominant frequency of the reflected signals is around 70–80 Hz on average.

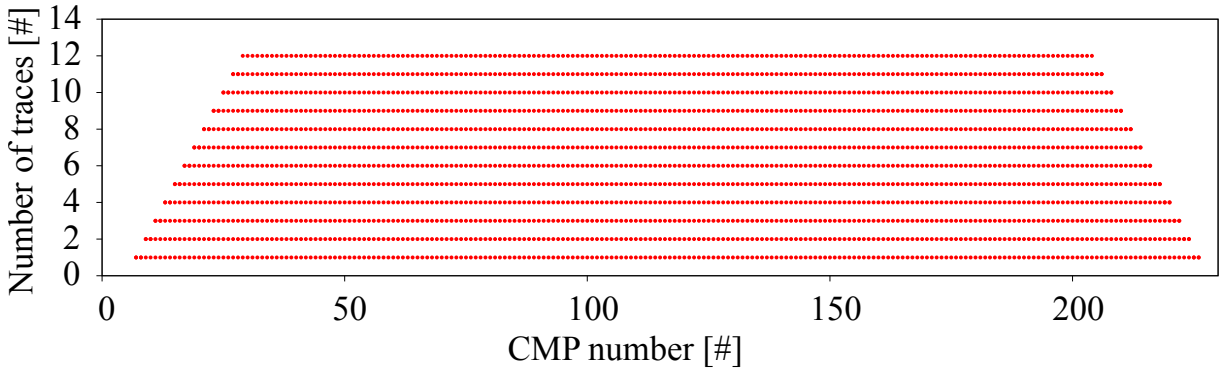

Figure 5.2: CMP fold diagram.

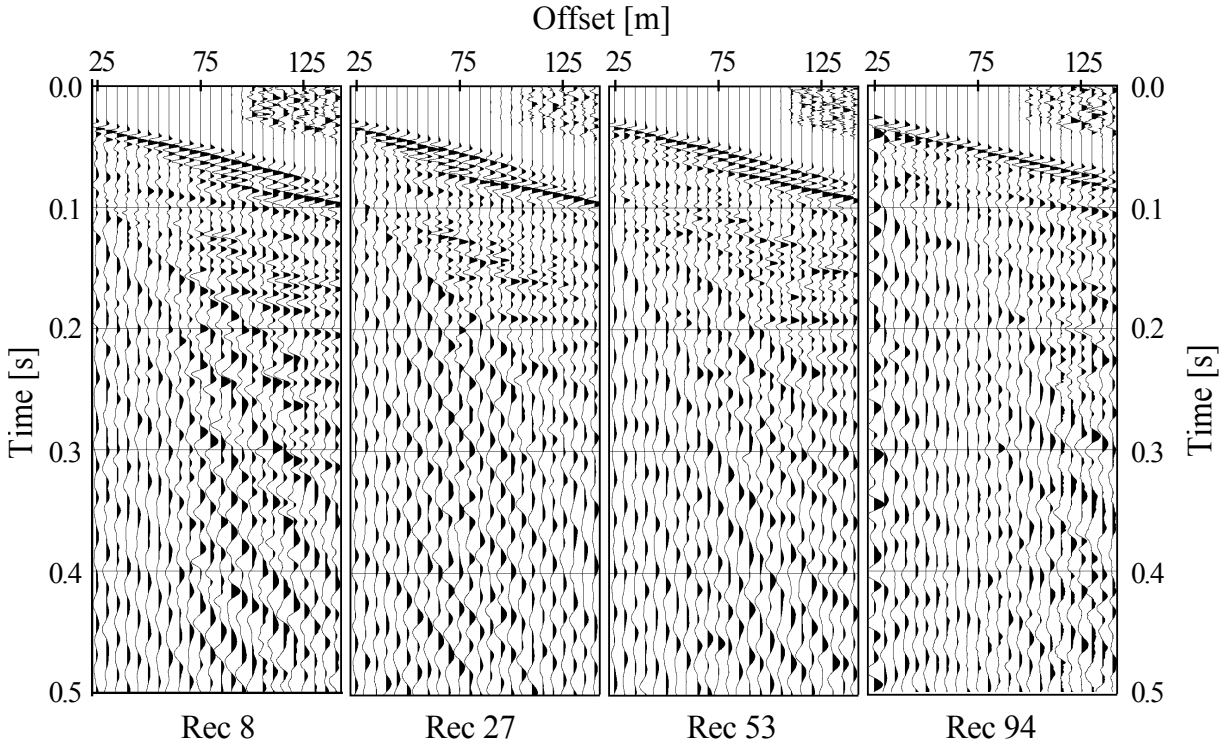

Figure 5.3: Raw shot gathers from three locations along the line. For display purposes, AGC scaling with a 100-ms window has been applied.

The data processing steps were performed on a laptop using Parallel Geoscience Corp.'s SPW seismic package. To attenuate low-frequency ground roll components still evident in the records and high-frequency noises, Butterworth band-pass filtering (50–250 Hz, 24 dB/octave) was used. F-k muting helped to filter out ground roll with higher frequencies (up to about 60 Hz), some of which had a small amount of spatial aliasing, but also the aliased portions of other linear noises (e.g., critically refracted wave and airwave), sometimes evident in the records (see Figure 5.5). Removal of time-break variations due to small unavoidable differences among source depths and/or to trigger inaccuracies completed the preprocessing. No amplitude correction neither trace balancing nor spherical divergence corrections were applied and, since topography was flat, no field statics were calculated. Figure 5.6 shows the filtered records shown in Figure 5.3.

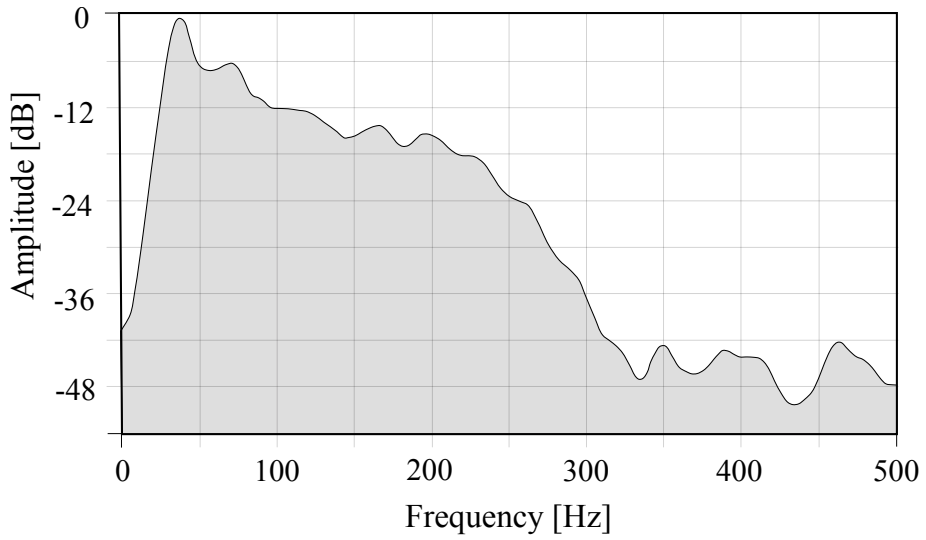

Figure 5.4: Amplitude spectrum obtained averaging the first 8 traces (near offset traces) from 50 shot gathers. Note that signal frequencies up to 300 Hz appear well above the background noise level.

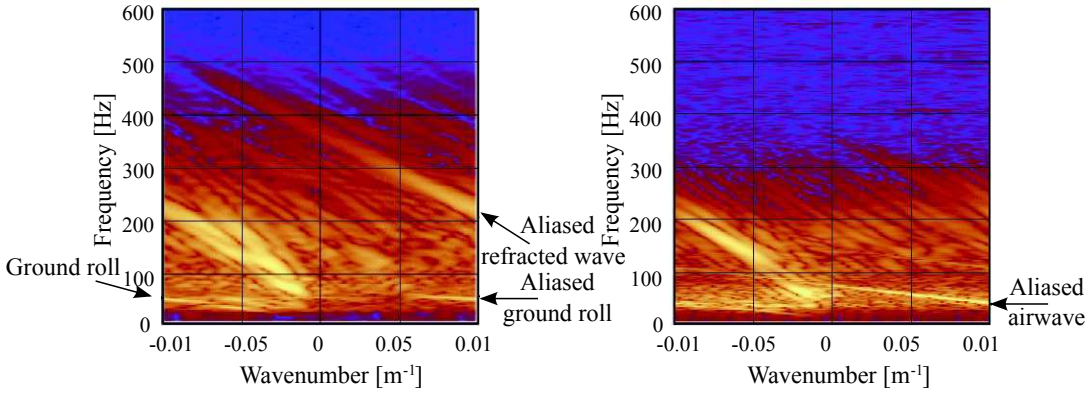

Figure 5.5: Two examples of f-k spectra (relative amplitude in dB).

5.2 CMP Processing

I performed the CMP processing using the standard approaches and procedures described in many text books [e.g. Baker, 1999; Yilmaz, 1987], paying particular attention to velocity analysis and to residual static corrections. To obtain high-amplitude stacked traces, I started evaluating by visual fitting of reflection hyperbolas on CMP gathers preliminary stacking velocity values roughly between 1800 and 2400 m/s. After that, I used these values as starting point for a more accurate stacking velocity analysis, which I performed, CMP-by-CMP, through the integration of semblance plots, constant velocity scan (CVS) and constant velocity stacks. As shown by clear reflections in Figure 5.7a and the relatively sharp peaks in the semblance plot of Figure 5.7b, the resolution of stacking velocities was quite good for events above 250 ms twt, while velocity resolution was poor for greater traveltimes. This was mainly caused by the maximum offset

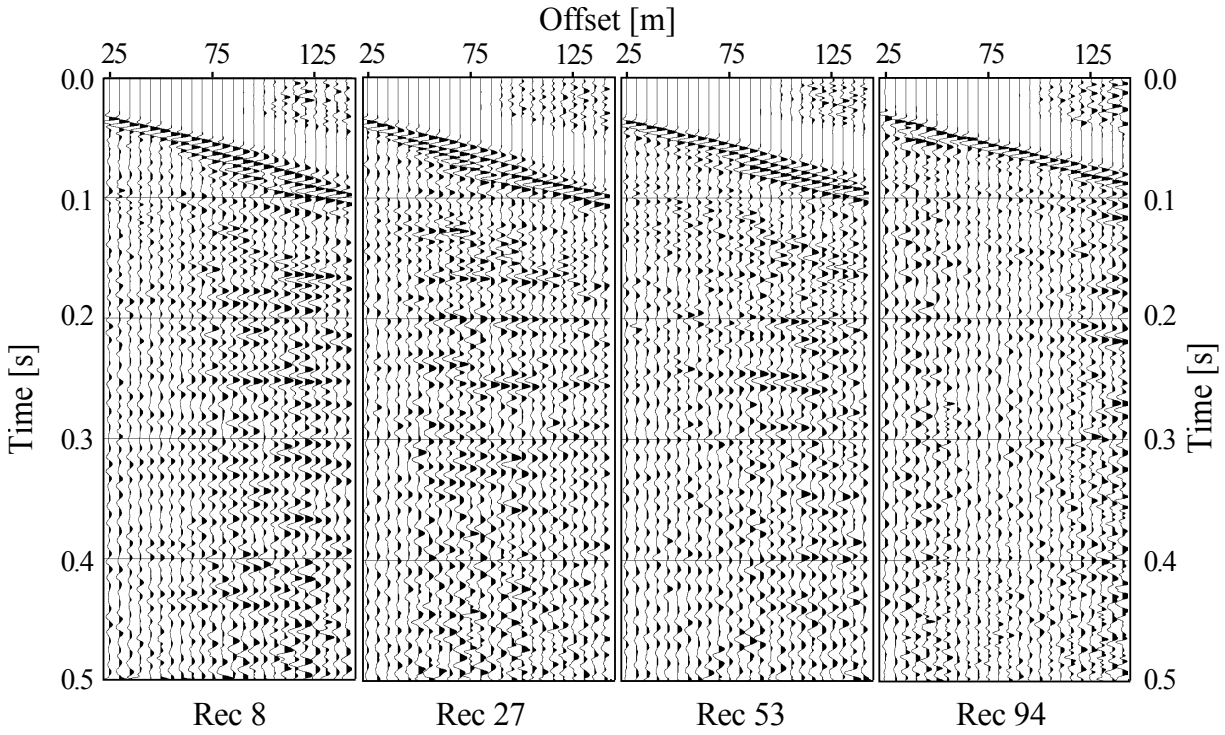

Figure 5.6: The same records as Figure 5.3, after Butterworth filtering and f–k muting to help remove the ground roll.

used to acquire the data, basically too short to produce significant normal move-out for events below 200-250 ms twt. A higher number of receivers would have enabled offsets sufficiently large for a better velocity control of deeper events, without the risk of incurring spatial aliasing of surface waves. Unfortunately, these were not available at the time of the acquisition. To overcome inaccuracies caused by the elongation of the semblance maxima along the velocity axis, I refined the velocities by means of a visual adjustment of the corresponding hyperbolas on the CMP data. This was only possible when the S/N ratio of the analyzed event was significantly high.

I completed the prestack process removing the short-wavelength misalignments sometimes visible along the profile by means of surface-consistent residual statics corrections. Five loops of a conventional correlation routine with a time correlation window ranging from 0.08 ms to 0.3 ms and maximum allowable time shift of ± 5 ms proved to be adequate for this purpose.

The final stacking velocity field that I used to NMO correct the P-wave data shows lateral and vertical velocity variations, ranging from 1850 to 2450 m/s (see Figure 5.8b). The most prominent are the vertical changes occurring at the interfaces, while the lateral changes are confined almost exclusively in the near surface, at 350-450 m from the source. The resulting CMP stacked section reveals a simple stratigraphic framework along the survey line. Several clear reflections are visible throughout the entire section, although not always continuous (Figure 5.8a). In the near-surface, down to about 140 ms two-way traveltime, the reflections appear as flat events, while at greater depths the more continuous events are dipping. The shallowest reflection, with onset of about 60 ms two-way traveltime, is continuous from the beginning of the section up to the

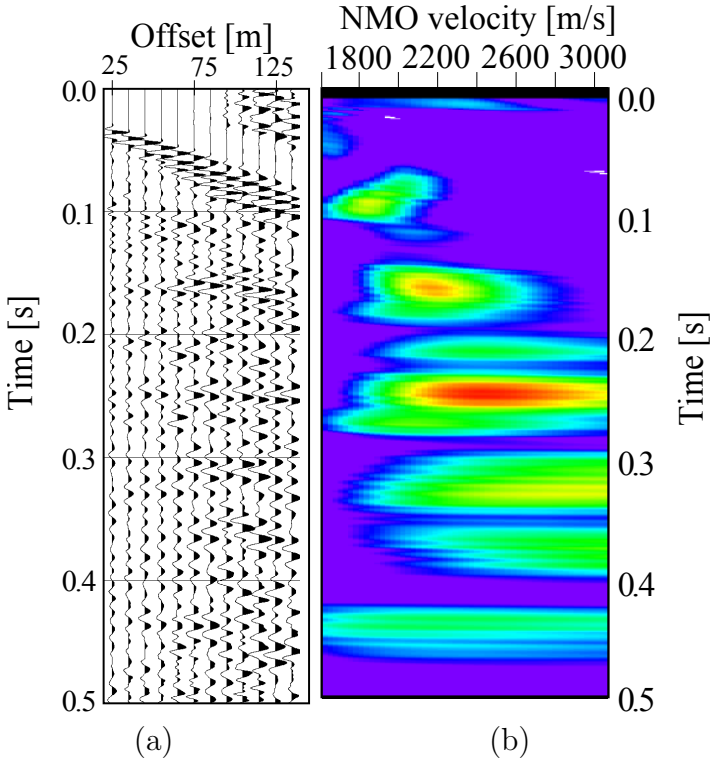

Figure 5.7: (a) CMP gather 54 with (b) its velocity spectrum (semblance plot).

distance of 350 m, where it disappears or its amplitudes become too low. The second flat reflection (onset of 120 ms) is evident only beyond the progressive of 200 m. Below it, in a system of dipping reflectors being more or less continuous, the one with the highest amplitudes starts at the beginning of the section with onset of about 250 ms and shallows up to 190 ms at the end of the section. For this event, too, amplitudes greatly change along the section. Deeper reflectors are also evident but they appear very discontinuous, probably because the uncertainties in velocity values at depths greater than 250 ms two-way traveltimes prevented a well-defined seismic imaging. Lack of reflected energy also contributed to the weakness of deeper reflection events.

5.3 CRS Processing

I swiftly implemented the CRS processing in a completely data-driven way on the same preprocessed data used for the conventional CMP imaging. The only a-priori information concerning the prestack-data and the unknown stacking velocity model that I provided were the near-surface velocity along the seismic line (1900 m/s) and the dominant frequency of the reflected signals (70 Hz). Both are required to evaluate the time-domain variation of the CRS midpoint aperture between the minimum and maximum values defined by the user. I used the dominant frequency of the reflections also to set the coherence-analysis bandwidth, which as a rule of thumb should equal the dominant period of the reflections. As a guide for the data-driven implementation and to minimize the computational effort, I provided the expected range of NMO velocities

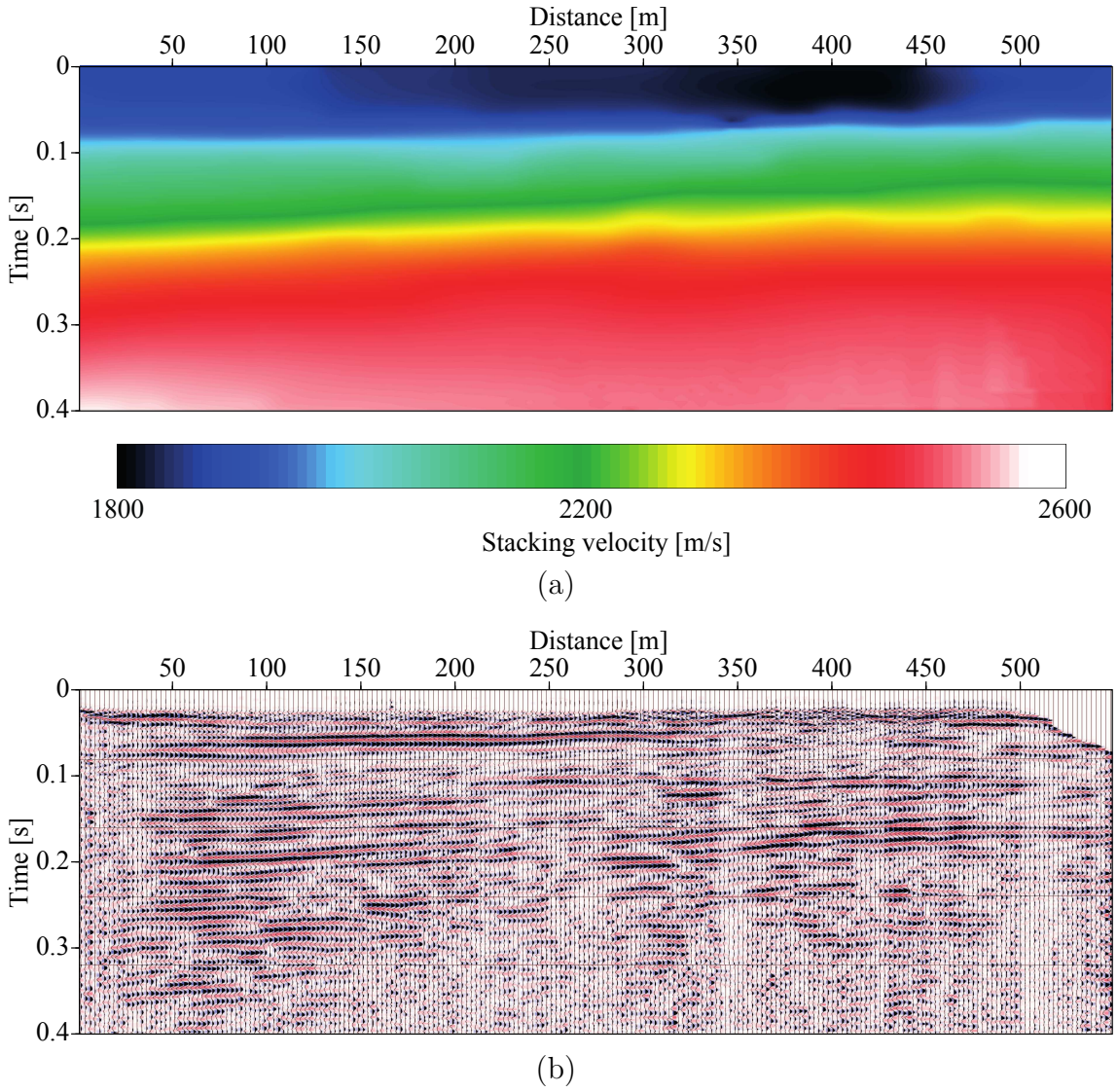

Figure 5.8: (a) Stacking velocity field obtained through integrated analysis of constant velocity scan, constant velocity stacks, and semblance plots. The velocity map, defined for all time samples up to 400 ms two-way traveltime and all CMPs, was generated by interpolation of the time-velocity curves spaced along the seismic line. (b) CMP stacked time section.

between 1800-2400 m/s. As outlined on the processing parameters listed in Table 5.2, I performed the coherence analysis using traces normalized with the magnitude of the analytic signal. This helped to make the semblance coefficients less sensitive to possible amplitude variations and/or to the presence of high-amplitude noise along the offset. The stack process was instead performed without gain.

In estimating the optimized CRS attributes (α, R_{NIP}, R_N), I paid great attention to the determination of the appropriate aperture values. In order to include as many traces as possible in the automatic semblance analysis and related stack process without including excessive noise I used an offset aperture of between 25 m and 140 m at 0.02 s twt and 0.07 s twt respectively. The maximum available offset of data was used because no

Context	Processing parameter	Setting
General Parameters	Dominant frequency	70 Hz
	Coherence measure	Semblance
	Data used for coherence analysis	Normalized traces
	Temporal width of coherence band	15 ms
Velocities	Near surface velocity	1900 m/s
	Stacking velocities	1800-2400 m/s
Apertures and taper	Minimum midpoint aperture	25 m @ 0.02 s
	Maximum midpoint aperture	140 m @ 0.07 s
	Minimum ZO aperture	20 m @ 0.02 s
	Maximum ZO aperture	70 m @ 0.3 s
	Relative taper size	30 %
Automatic CMP stack	Number of refinement iterations	3
Linear ZO stack	Tested emergence angles	$-15^\circ \ldots 15^\circ$
	Initial emergence angle increment	1°
	Number of refinement iterations	3
Hyperbolic ZO stack	Number of refinement iterations	3
Local optimization	Coherence threshold for smallest traveltime	0.0
	Coherence threshold for largest traveltime	0.0
	Maximum number of iterations	100

Table 5.2: Processing parameters used for the CRS stack process.

stretch effects were expected to be generated by the CRS stack. The determination of the CRS aperture along the midpoint direction was a bit more laborious. Starting from a preliminary stacking velocity model and assuming a maximum reflection twt of 0.3 s, I used as first attempt a time-dependent aperture increasing between 26 m at 0.02 s twt and 100 m at 0.3 s twt. Afterwards, by analyzing the ratio between the chosen aperture and the approximate size of the first Fresnel zone, which is automatically calculated by the code for each sample of the stacked section, I repeatedly changed the minimum and the maximum midpoint apertures to search the optimal values not larger than the first Fresnel zone and as small as image quality and stacking parameter reliability allowed. In this way, by checking the quality of the results through the analysis of both the stacked and coherence (semblance) sections, I got optimum minimum and maximum apertures of 10 m and 70 m at 0.02 s twt and 0.3 s twt respectively. Several tests were also made to evelaute the influence of the other CRS parameters reported in Table 5.2, which however provided only minimal changes on the final results and, accordingly, are not analysed in detail.

To remove outliers and fluctuations without physical meaning, to enhance the trace-to-trace continuity of reflection events and to refine both the stacked and kinematic wavefield attribute sections I applied within the CRS-stack workflow an event-consistent smoothing of the CRS parameters and surface-consistent residual static corrections.

Following the event-consistent smoothing process proposed by Mann and Duveneck

Context	Processing parameter	Setting
Input	Data used for moveout correction	Original traces
	Moveout correction performed by	Optimized CRS attributes
	ZO section used as pilot traces	Optimized CRS stack
Cross correlation	Maximum correlation shift	5 ms
	ZO time used for cross correlation	0.08-0.3 ms
	Correlation weight	CRS semblance
	Minimum number of 'live' samples per traces	0
Estimation of Static Corrections	Data used for static correction estimation	Original correlation results
	Method applied	Center of area around local maximum
	Minimum number of contributions	sources:1, receivers:1

Table 5.3: Processing parameters used for the CRS-based residual static corrections.

[2004], I smoothed the CRS parameters (α, R_{NIP}, R_N) of each ZO sample exceeding a time-dependent coherence threshold linearly decreasing from 0.4 at minimum traveltime to 0.2 at maximum traveltime. To avoid mixing the different events, the parallelogram shaped smoothing window was set with a temporal extension of 15 ms and a spatial extension of 7 meters.

After that, I evaluated the residual static corrections via the CRS based surface-consistent residual static correction method [Koglin et al., 2006], using for the moveut correction of the prestack data the CRS parameters previously smoothed. In doing this I used the same threshold adopted in the standard CMP processing (i.e. with a maximum allowable static shift of $\pm$ 5 ms), and the same CRS apertures that I used for the CRS stack (see Table 5.3). Larger aperture values as well as other values on the CRS stack-based surface-consistent residual static correction parameters did not lead to different results. This was probably because of the characteristics of the considered dataset.

The result that I obtained after five iterations of the whole procedure is the CRS-stacked section shown in Figure 5.9. In this section all the reflectors already highlighted in the CMP stacked section, from the shallowest down to the deepest ones, are well-imaged too, with increased reflection continuity and greater S/N ratios. Particularly, the CMP stacked events, only barely perceptible at traveltimes larger than 250 ms, appear better defined and continuous in the CRS-stacked section. This result is clearly due to the fact that the number of traces used by the CRS stack to generate each single ZO stacked trace is up to 20 times higher than that used by the CMP stack process (see Figure 5.10 and Figure 5.11).

The obtained CRS wavefield parameters agree with CRS stacked section. As already mentioned these have a well defined physical meaning (see Chapter 4) and therefore can be used as tools for quality control of the stacked section. In a constant velocity medium the R_{NIP} parameter is associated with the reflector depth, but deviates from it as the geology becomes more complex. In this case the values of R_{NIP} which roughly resemble

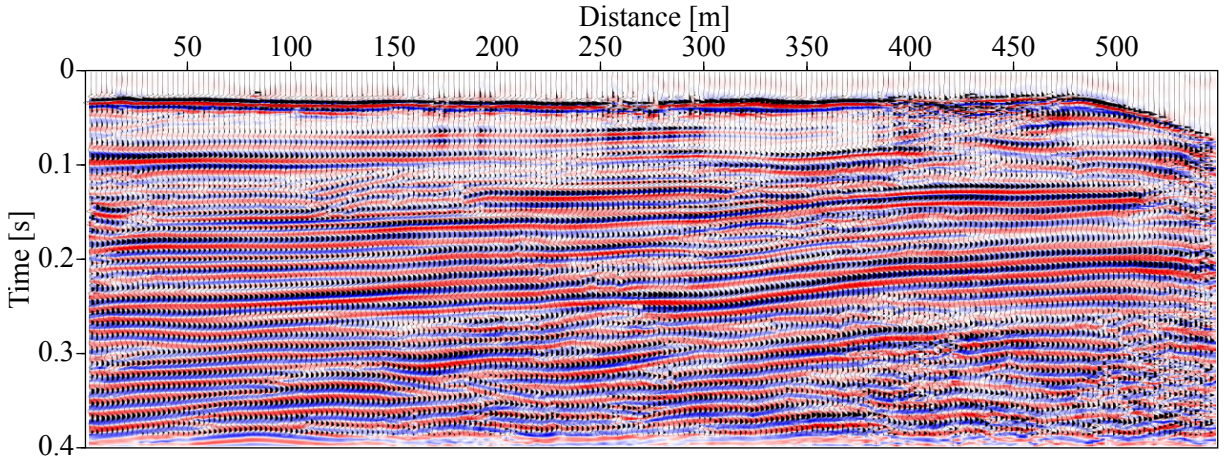

Figure 5.9: Optimized CRS stacked section.

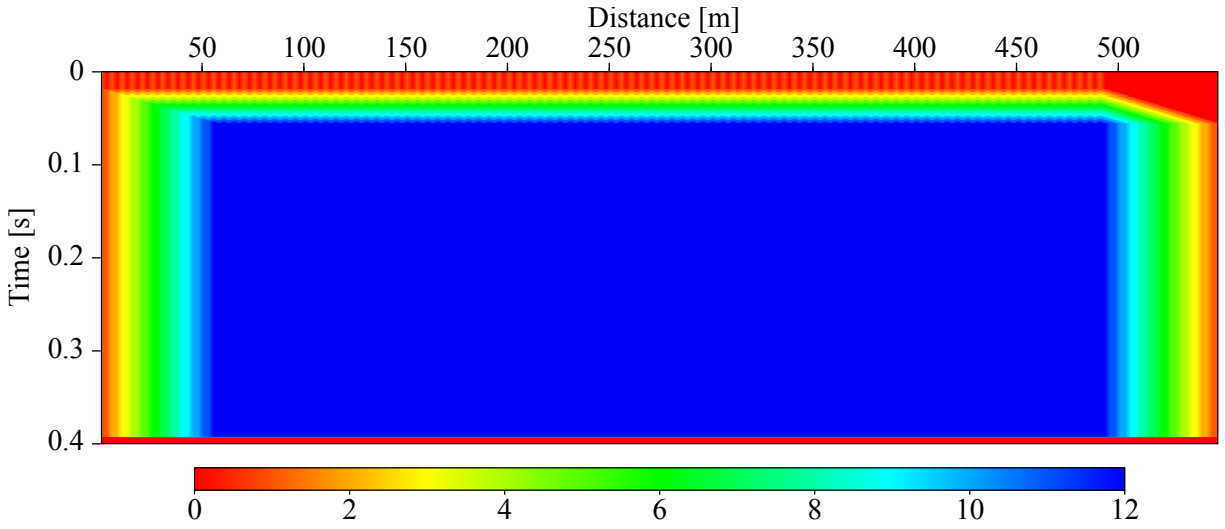

Figure 5.10: Time-variant CMP fold diagram.

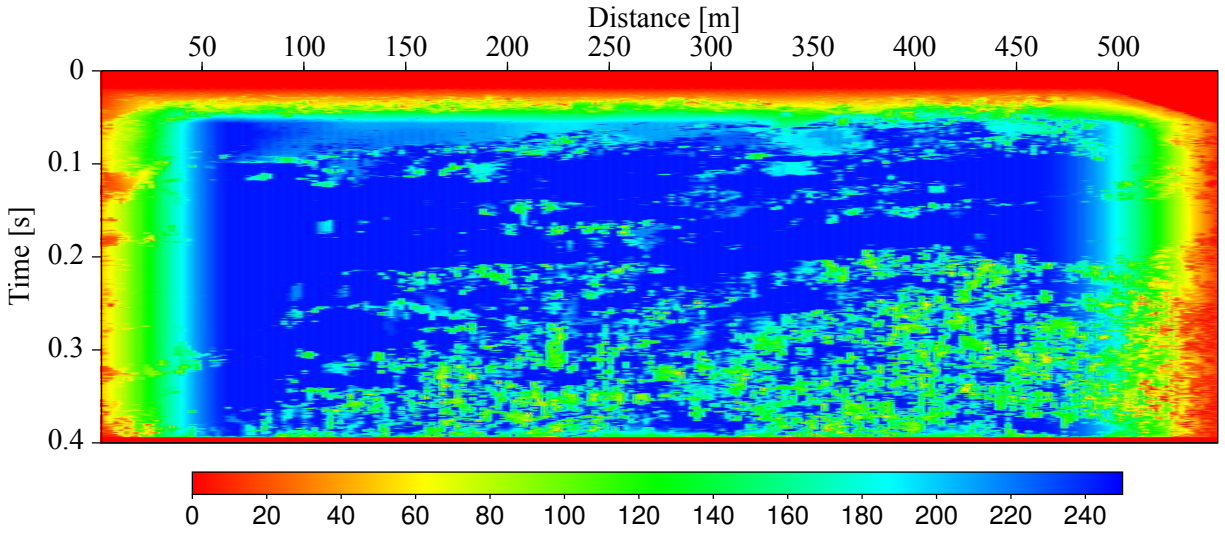

Figure 5.11: Time-variant CRS fold diagram.

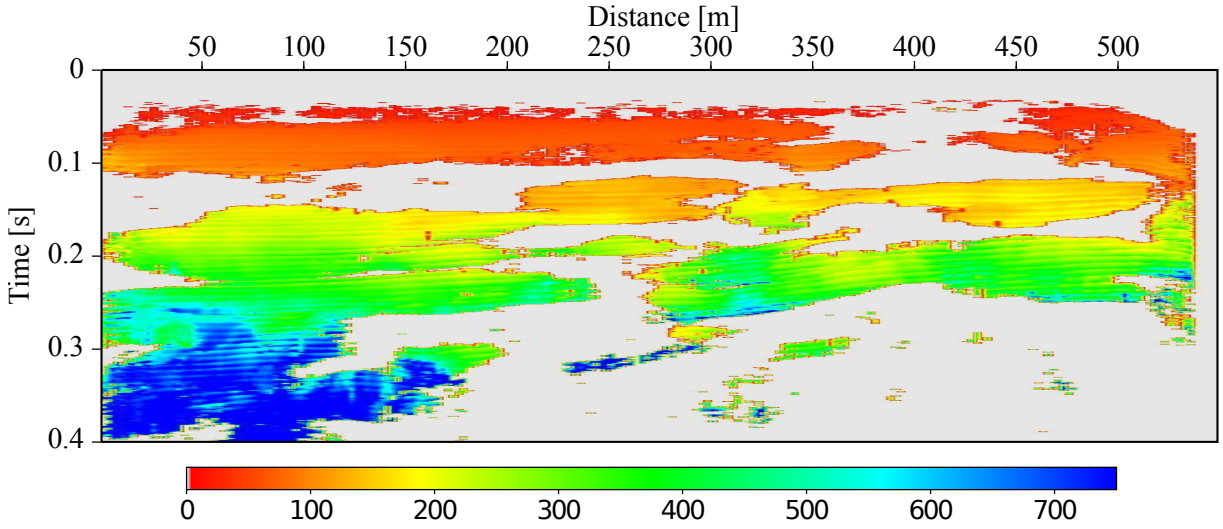

Figure 5.12: Radius of the Normal-Incidence-Point (R_{NIP}) wavefront [m]. ZO samples with very low coherence value are masked out (gray), as they are not expected to be related to reliable attributes.

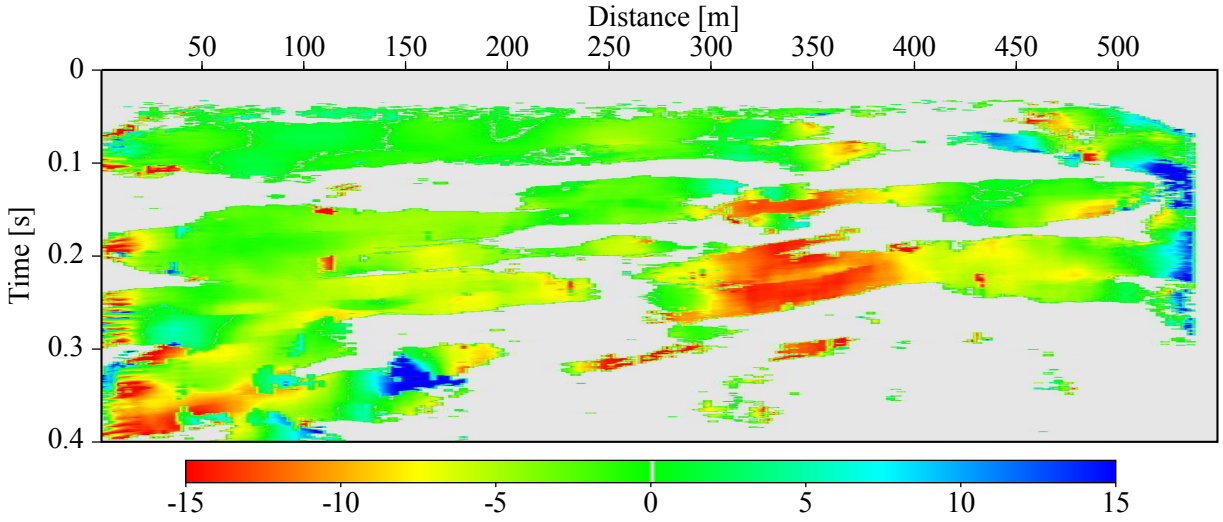

Figure 5.13: Emergence angle of the simulated ZO rays [deg]. ZO samples with very low coherence value are masked out (gray), as they are not expected to be related to reliable attributes.

the reflectors depths (see Figure 5.12) indicate the presence of shallow nearly planar reflectors. Likewise, the small values assumed by the angle of emergence α (Figure 5.13) and by the N-wave curvatures $1/R_N$ (Figure 5.14), which represent a measure of the curvature of the reflectors, agree with the presence of planar reflectors. The emergence angle α increases significantly up to $-14\,^\circ$ only in the central part of the section, at 0.15-0.3 s twt and 270-400 m along the seismic line, i.e. where the CRS code imaged dipping reflectors.

Despite the overall improvement in S/N ratio, the large number of stacked traces produced also bogus alignments of seismic energy which hinder the interpretation of the

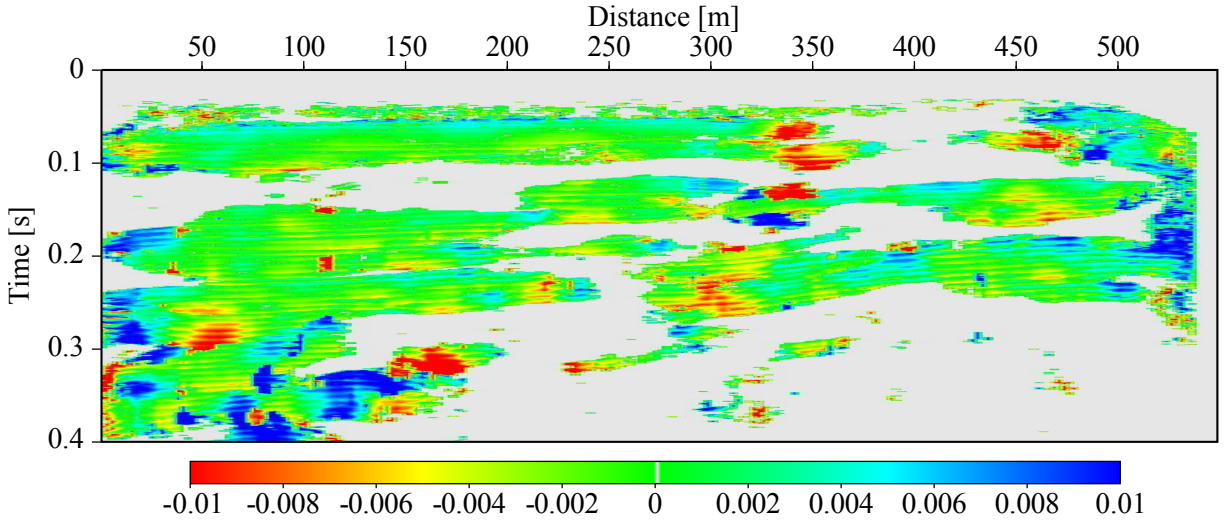

Figure 5.14: Curvature of the normal wave [1/m]. ZO samples with very low coherence value are masked out (gray), as they are not expected to be related to reliable attributes.

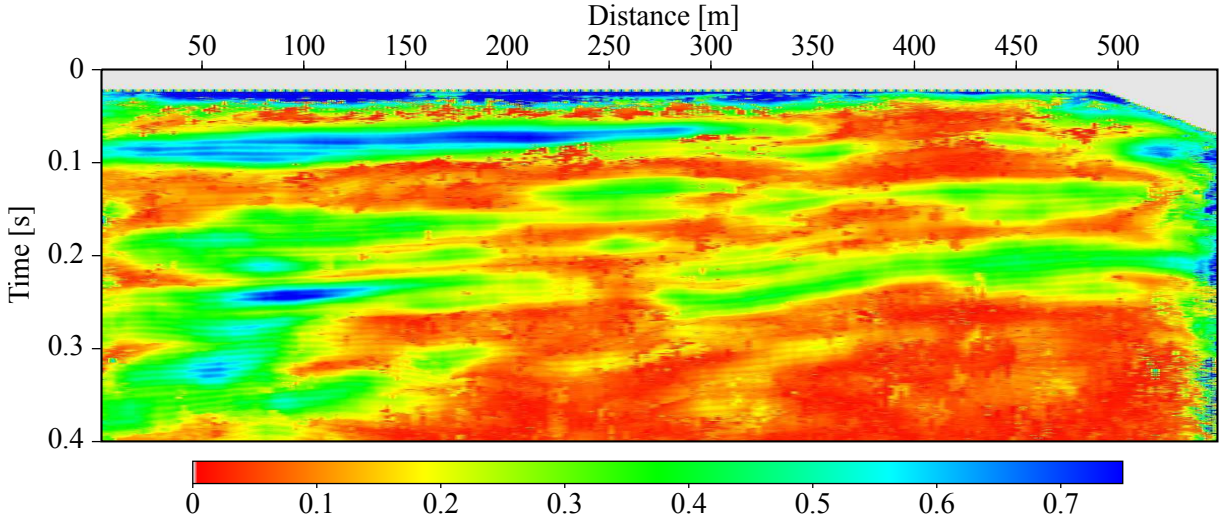

Figure 5.15: Coherence, associated with the optimized CRS stack.

CRS stacked section. Since most of these alignments are hardly noticeable in corresponding CMP gathers and CRS-coherence section (Figure 5.15), they should not be considered as genuine reflections. Indeed the real reflections have coherence values much higher than those of surrounding noise. Even at large traveltimes where the midpoint aperture includes more traces and thus more noise, the coherence values still clearly separate the reflection events from the noise. Therefore, I tried to overcome this drawback by weighting each sample of the CRS stacked section with the corresponding value of coherence and of number of stacked traces. This procedure is fully consistent within the CRS processing chain, which is entirely based on coherence measures. The resulting weighted section (Figure 5.16) shows a remarkable S/N ratio improvement compared to the CMP stacked section, and although the weights destroy the original amplitude information it appears more appropriate than the CRS stacked section in delineating the aquifer and its confining units.

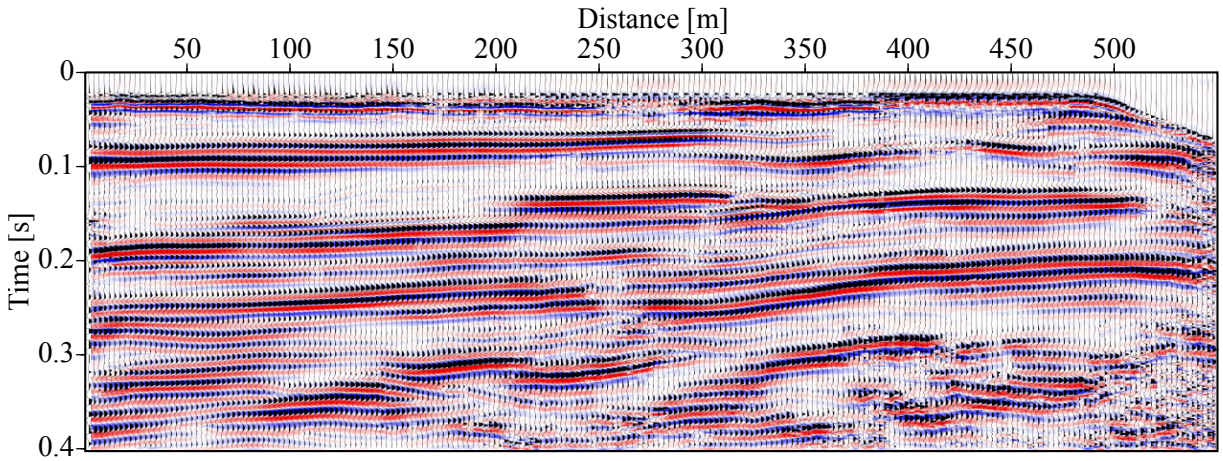

Figure 5.16: Weighted optimized CRS stacked section.

5.4 NIP tomography

Although the CRS stack is able to produce stacked sections without any preliminary explicit velocity analysis, interval velocities are usually required to characterize and interpret the subsurface. Therefore, in order to make a more exhaustive comparison between the two approaches, I completed the CRS processing chain using the tomographic inversion approach proposed by Duveneck [2004] to estimate the interval velocities field.

As a input for the tomographic inversion process I used 1,335 traveltime values picked by hand directly on the CRS stacked section along the most prominent primary reflections, together with their associated values of p and M_{NIP} which were automatically extracted from the corresponding attribute sections. Since the quality of the ZO input points heavily impacts on the tomography results, before using them I identified and I removed the excessively noisy data by plotting the parameter M_{NIP} against the traveltime t_0 (Figure 5.17a). After that, keeping in mind that the R_{NIP} parameter increases with the reflector depth, I considered as noise and thus I removed from the inversion process the picks that departed significantly from the main trend of M_{NIP} which, as a result of the R_{NIP} trend, should decrease with increasing t_0 (see Figure 5.17a). Likewise, I removed from the inversion process the data with too low or too high stacking velocities at distinct traveltimes (see Figure 5.17b). After this regularization process 694 points remained. Their locations are displayed in Figure 5.18 over the CRS stacked section.

After having determined the input data, I started to derive the NIP-wave tomography model using a grid consisting of 29 nodes in lateral and 51 nodes in vertical direction, with grid spacing respectively of 20 m and 10 m. As initial model I used a velocity model with near surface velocity of 1800 m/s and a constant velocity gradient of 1.5 s^{-1} (see Figure 5.20). To reduce the misfit between the forward-modelled attributes and the picked kinematic wavefield attributes I carried out the least-squares minimization process using the inversion parameters listed in Table 5.4. With these parameters, the the cost function S decreased rapidly up to the seventh iteration, after which remained nearly unchanged (see Figure 5.19). The interval velocity models resulting at some representative iteration steps are shown in Figure 5.20. Given these results, I considered as

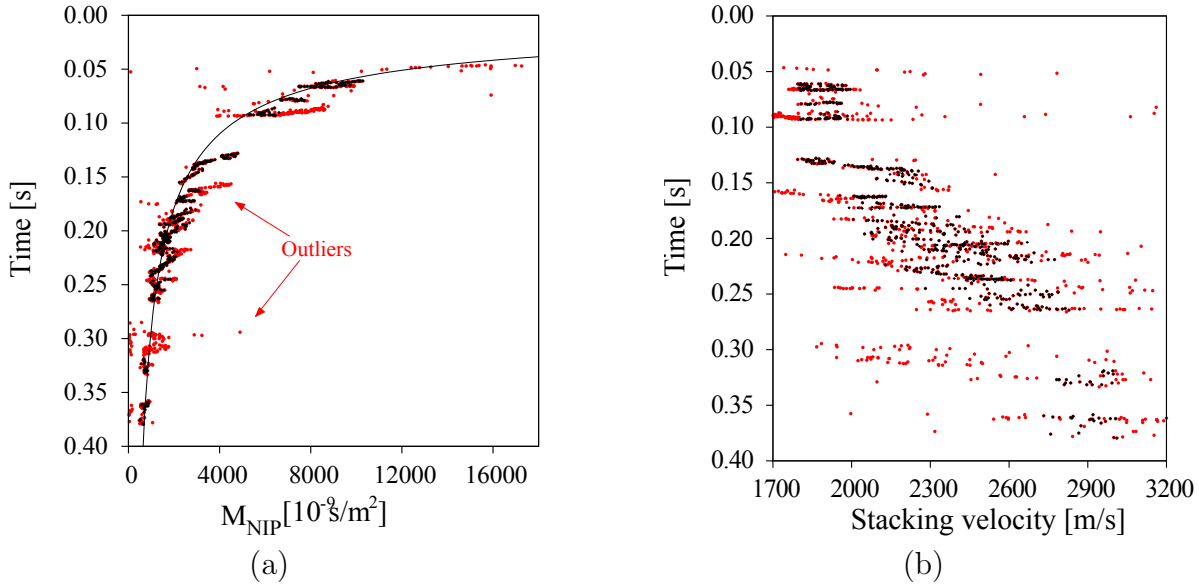

Figure 5.17: Quality control of input picks for NIP-wave tomography through the parameter M_{NIP} (a) and the stacking velocities computed for each picked ZO point (b). All input not meeting the QC requirements (in red) have been removed.

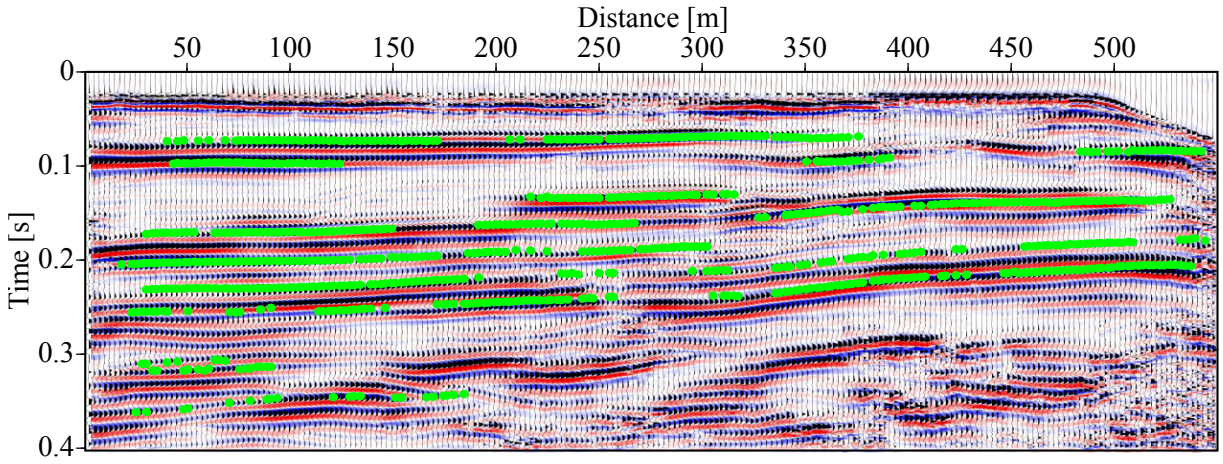

Figure 5.18: Picked traveltimes (green dots) remained after the QC described in Figure 5.17

final result of tomographic inversion process the interval velocity model obtained after seven iterations. This is shown in Figure 5.21a and in Figure 5.21b with the corresponding back-propagated picks. Compared to the interval velocity field (Figure 5.22) obtained through the Dix [1955] equations, the interval velocity field derived using the NIP-wave tomography process shows velocities changing in a wider range, which reaches higher values in the shallowest portion of the section, and it is more laterally structured. The interval velocity field obtained applying the Dix [1955] equations appears to be more accurate and better related to the data than the NIP-wave tomography model. Probably, the small moveout of these P-wave prevented the estimation of sufficiently accurate interval velocity models from the derived M_{NIP} parameter.

Processing parameter	**Setting**
Lateral grid spacing	20 m
Depth grid spacing	10 m
Number of nodes in lateral direction	29
Number of nodes in depth direction	51
Assumed error for time measurement	5 ms
Assumed error for measurement of M_{NIP}	250 10^{-9} s/m^2
Assumed error for horizontal slowness p	25 10^{-6} s/m
Assumed error for surface position	2 m
Initial model:	
surface velocity	1800 m/s
gradient	1.5 s^{-1}
Number of iterations	12

Table 5.4: Parameters used for the NIP-wave tomographic inversion.

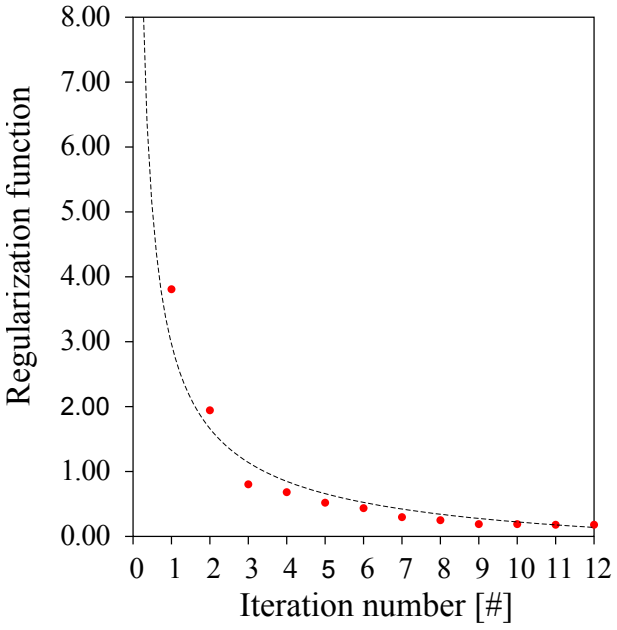

Figure 5.19: Value of the cost function S computed after every tomographic iteration.

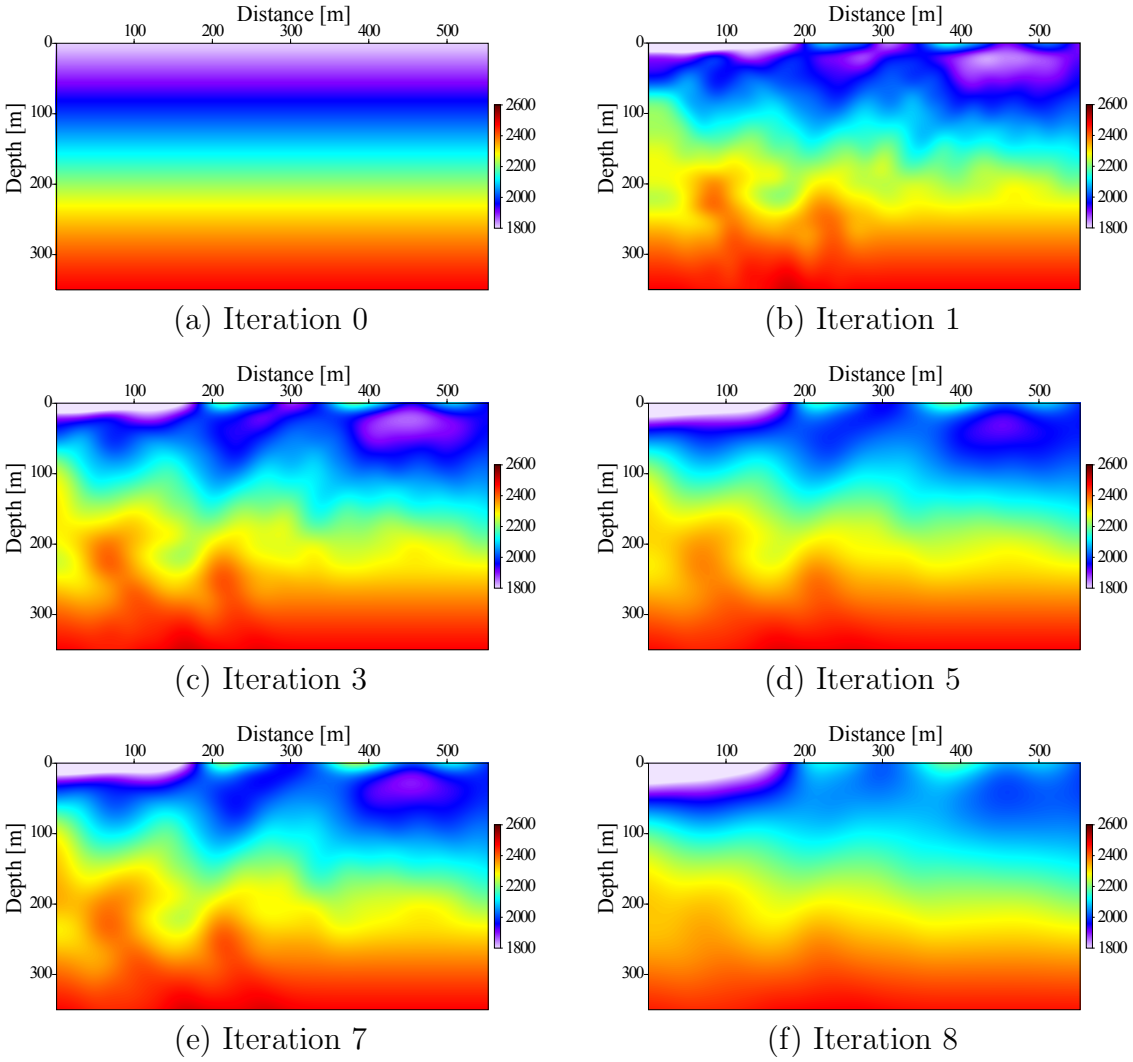

(a) Iteration 0

(b) Iteration 1

(c) Iteration 3

(d) Iteration 5

(e) Iteration 7

(f) Iteration 8

Figure 5.20: Interval velocity models after exemplarily chosen iteration steps. Starting from the initial gradient (a), the model is continuously updated. After iteration 7 the velocity model did not change. Given these results, I considered as final result the model obtained after seven iterations (model e). This is enlarged in Figure 5.21.

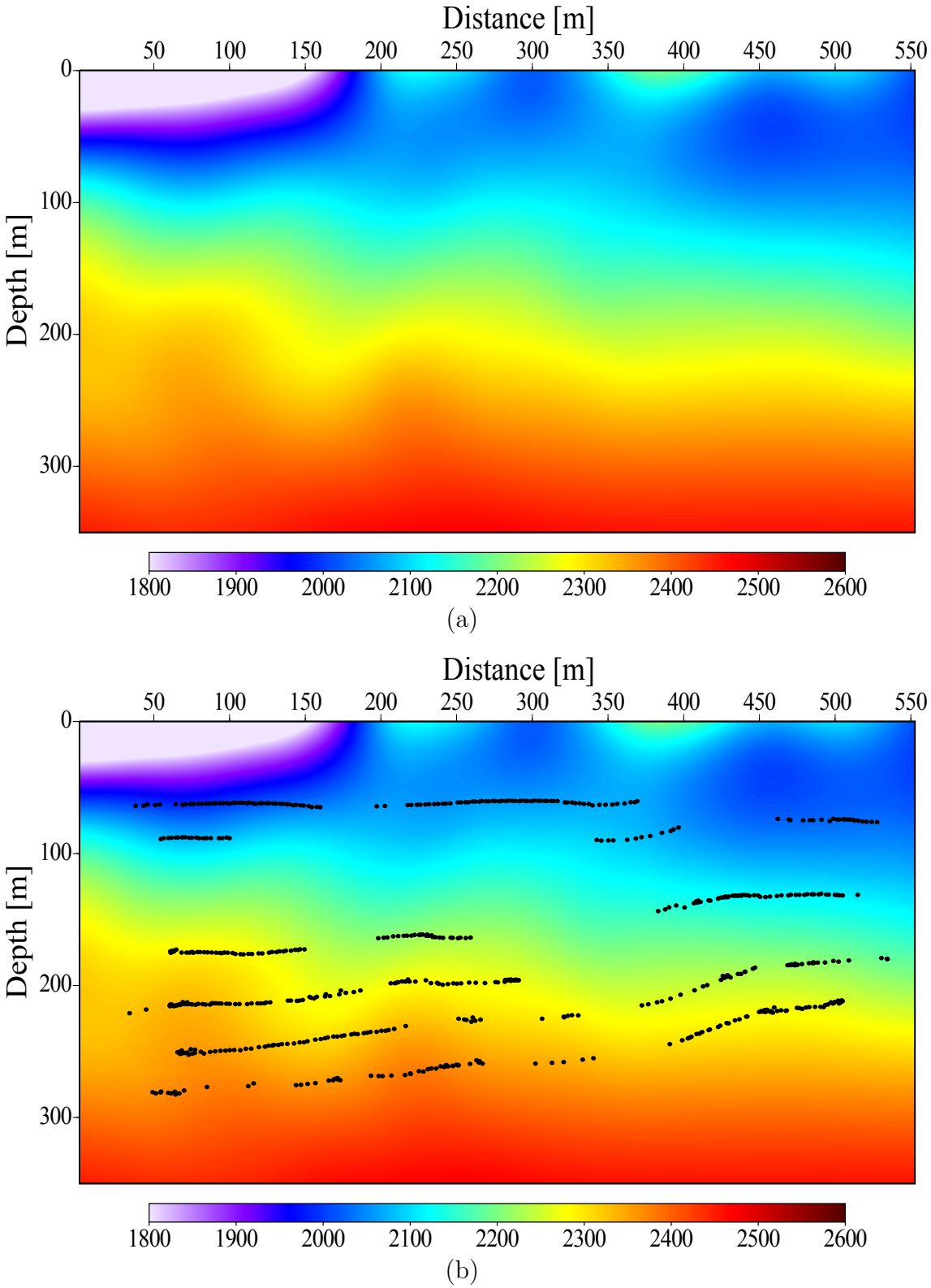

Figure 5.21: Reconstructed depth velocity model (a) with back propagated picks (b) after seven NIP-wave tomographic iterations.

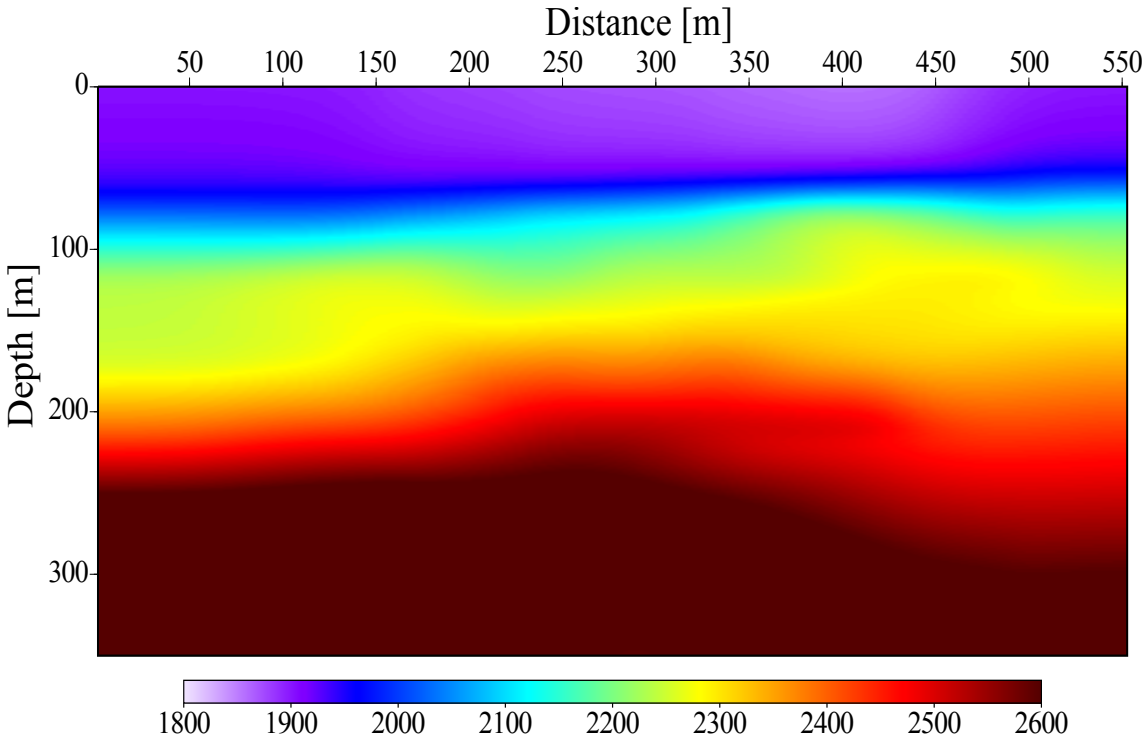

Figure 5.22: Interval velocity model obtained applying the Dix [1955] equations to the stacking velocity field computed by the standard CMP velocity analysis. The colour velocity scale is the same used for Figure 5.21, to allow an easier comparison between the velocity fields.

Chapter 6

Second example: SH-wave dataset*

The second dataset that I will present was collected in a ultra-shallow SH-wave reflection survey conducted on the construction site for a dry bridge located in Southern Sardinia (Italy). The primary intent of the survey was to delineate the bedrock topography to a depth of about 10-15 m, including any possible reflectors within the overburden. The secondary intent was to accurately outline the shear-wave velocities field in order to estimate the geotechnical properties of the site.

The quality and resolution of this dataset are very high, as both the local geology conditions of the site and the equipment available proved to be favourable to the survey. The shear-wave velocities of the unconsolidated materials were indeed relatively low to the order of 70-130 m/s. In addition, the shear-wave energy generated using the sledgehammer, whose efficiency in general is very site-dependent, had a dominant frequency of 70-80 Hz. Low velocities and high frequencies produced SH-waves with dominant wavelengths between 0.9 and 1.5 m. Using the one-fourth wavelength minimum criterion of Widess [1973], the resulting data provided a potential vertical resolution limit of about 30 cm. Furthermore, the reflections were free from Love-wave distortion, probably because the ratio between the predominant wavelength and the thickness of the superficial layer that acted as a waveguide was sufficiently small so as to produce only minimal dispersion of Love waves [see e.g. Deidda and Ranieri, 2001]. Finally, the special horizontal receivers used during this survey enabled the acquisition of high-quality SH-wave records without the need of opposite shots, thus avoiding any possible processing degradation related to the stacking of opposite shots. All these favourable conditions resulted in a ultrashallow seismic reflection dataset with several clear reflection events which produced a very detailed CMP image of the subsurface. This dataset thus provide an excellent opportunity to test the efficiency of the CRS stack processes in preserving the vertical and lateral seismic resolution for ultrashallow and high-resolution seismic reflection dataset.

*This example has been published under the following citation: Deidda G.P., Battaglia E., Heilmann Z., 2012, Common-reflection-surface imaging of shallow and ultrashallow reflectors: Geophysics, 77, B177-B185.

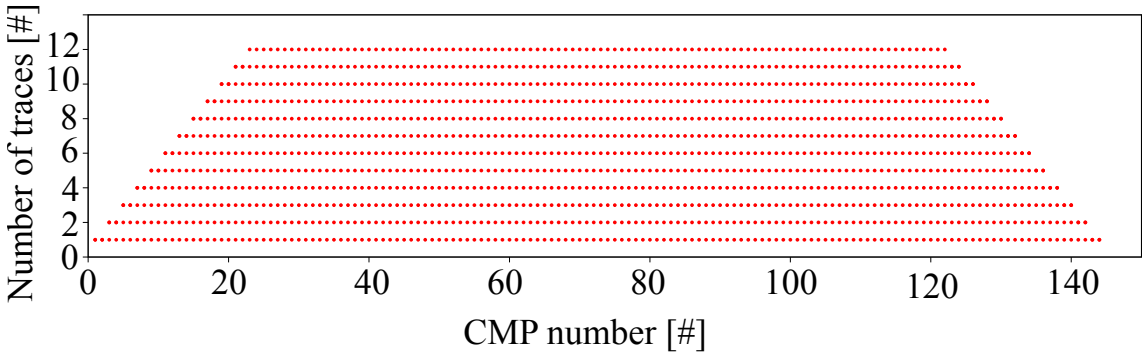

Figure 6.1: CMP fold diagram.

Seismograph	24-ch. ABEM Mark VI
Energy source	10-kg sledge-hammer
Receivers	24 100-Hz natural-frequency "Swyphone" detectors
Receiver spacing	0.5 m
Shot spacing	0.5 m
Spread geometry	off-end
Number of shots	61
Minimum offset	1 m
Maximum offset	12.5 m
Record length	400 ms
Sampling interval	0.25 ms
Number of CMPs	144
CMP spacing	0.25 m
Maximum CMP fold	12
Line length	42 m

Table 6.1: Equipment and parameters used during the acquisition.

6.1 Data acquisition and preprocessing

The data was recorded using an ABEM Mark VI 24-channel digital seismograph equipped with 18-bit A/D conversion and an array of 24 100-Hz natural-frequency "Swyphone" detectors [Sambuelli et al., 2001]. The SH-wave energy was generated by striking a 10-kg sledgehammer along a single direction perpendicular to the seismic line against a 70-kg steel plate coupled to the ground by grippers. Prior to planting geophones or firing shots the ground surface was carefully prepared to ensure sufficiently firm coupling of sources and receivers with the ground. The acquisition geometry was a conventional off-end configuration with receiver offsets ranging from 1 m to 12.5 m and source intervals of 0.5 m. The record length was 400 ms with a 0.25-ms sampling interval. The 61 shots recorded once sorted resulted in 144 CMP gathers 0.25-m spaced with nominal twelve-fold CMP coverage (Figure 6.1). All acquisition and equipment parameters are listed in Table 6.1.

Four representative shot gathers are shown in Figure 6.2. Reflections are evident above 200 ms. In the shot gathers of the first part of the line, up to record 20, five reflections

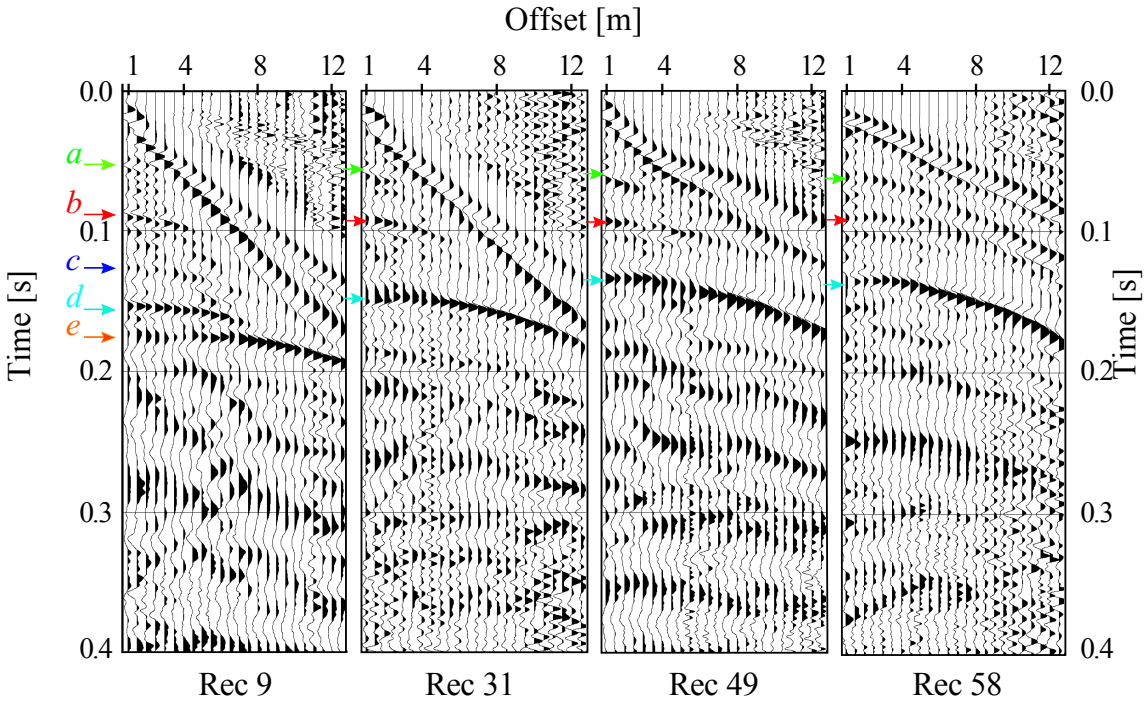

Figure 6.2: Raw shot gathers from four locations along the line. For display purposes, AGC scaling with a 60-ms window has been applied.

(events *a*, *b*, *c*, *d*, and *e*) are evident while in the others only three events (*a*, *b*, and *e*) are present. The event with zero-offset intercept time of about 170 ms marked as event *e* has the strongest S/N ratio and trace-to-trace continuity, and has been interpreted as the one originating from the top of the bedrock. The events marked *a*, *b*, *c* and *d* are instead reflections from the geological interfaces within the overburden materials. Compared to event *e* these appear much weaker and less continuous. Particularly, in the first part of the seismic line the shallowest reflection marked as event *a* appears very close to the direct wave and it is visible only in few near offsets traces. Beyond record 20 the reflections *c* and *d* disappear and only the events *a*, *b*, and *e* remain visible. No reflections events appear below the bedrock reflection. The variation of the slope of the first arrivals in the shot gathers along the line gives clear evidence of strong near-surface velocity changes. The spectral content of the records ranges from about 50 to 70 Hz at far offsets, and up to 90 Hz at near offsets. The peak-to-peak period of bedrock reflection slightly less than 20 ms indicates a dominant frequency of about 50 Hz.

The data was generally of high quality, so it required a minimal preprocessing sequence. This included assignment of field geometry, trace editing, first-arrival mute, and Butterworth filtering (60–200 Hz, 24 dB/octave), mainly aimed at attenuating Love waves and high-frequency noises. The topography at this site was flat so accordingly I applied neither elevation nor refraction statics. As any misalignment introduced by small changes in elevation had wavelengths shorter than the spread length I considered them as residual statics.

6.2 CMP processing

I accomplished the CMP imaging through a conventional CMP processing sequence based on velocity analysis, NMO corrections, NMO-stretch muting, residual static corrections and CMP stacking, without any post-stack processing step. I didn't perform the data migration because previously conducted tests had not produced significant improvements [e.g. Black et al., 1994]. As often occurs the velocity analysis and the residual static corrections proved to be the most important and time-consuming processing steps of the conventional CMP stack method.

I derived the stacking velocities CMP-by-CMP through several different velocity analysis algorithms using a velocity resolution of only 2 m/s. As can be easily seen in NMO-corrected CMP gathers displayed in Figure 6.3, velocity variations of only 2-4 m/s, corresponding to about a 3% of the correct stacking velocity value, could distort significantly the stack result. Hand-picked first arrivals supplied additional information on near-surface velocities. To compensate for the misalignments visible along the line, I applied a surface-consistent cross-correlation routine using a maximum allowable time shift of 2 ms. This small shift, about 1/5 of the dominant period of the reflected signals, prevented cycle-skipping errors, which would have arisen from larger time shifts. I iteratively perform together both the stacking velocity analysis and residual static corrections until the improvements in the data became negligible. To minimize the detrimental effects of the stretching process, e.g., reduction of the dominant frequency bandwidth and distortion of the amplitude of the reflection wavelet, I performed the NMO corrections with a stretch mute, limiting the allowable stretch to 25%.

The final stacking velocity field is displayed in Figure 6.4b. The stacking velocities range from 88 to 130 m/s exhibiting pronounced lateral changes, especially at 20-25 m along the seismic line. The resulting CMP stacked section (Figure 6.4a) provides very good images of all the reflections previously highlighted on the shot gathers displayed in Figure 6.2. The strongest and deepest bedrock reflection (event e) dips from 127 ms at the eastern end of the section to 170 ms at the western. Above, the other four events are imaged as almost flat-lying reflector at 150 ms (event d), 125 ms (event c), 88 ms (event b) and at 50 ms (event a). Particularly, events c and d show a very well-defined pinch-out with the bedrock. The shallowest reflection, event a at 50 ms two-way traveltime, appears better visible through the troughs (red) of the wavelet, although not along the entire line. Probably this is because very few traces per record contain the signal which, in addition, was partially muted performing the first-arrival (due to their closeness) and/or the stretch muting. The alignments appearing below the bed-rock do not have any matching with the corresponding pre-stack data therefore must be considered as not genuine reflections. The dipping event below 200 ms (see Figure 6.5a) is neither a reflection produced by a dipping interface nor the effect of spatial aliasing of Love waves. In fact, prudently assuming a Love-wave velocity of 80 m/s and a maximum frequency of 60 Hz, the 0.5 m geophone spacing used is sufficient to meet the sampling theorem condition to record data without spatial aliasing:

$$\Delta x \leq \frac{1}{2k_N} = \frac{V_{min}}{2f_{max}} = \frac{80}{120} = 0.67\,\mathrm{m} \tag{6.1}$$

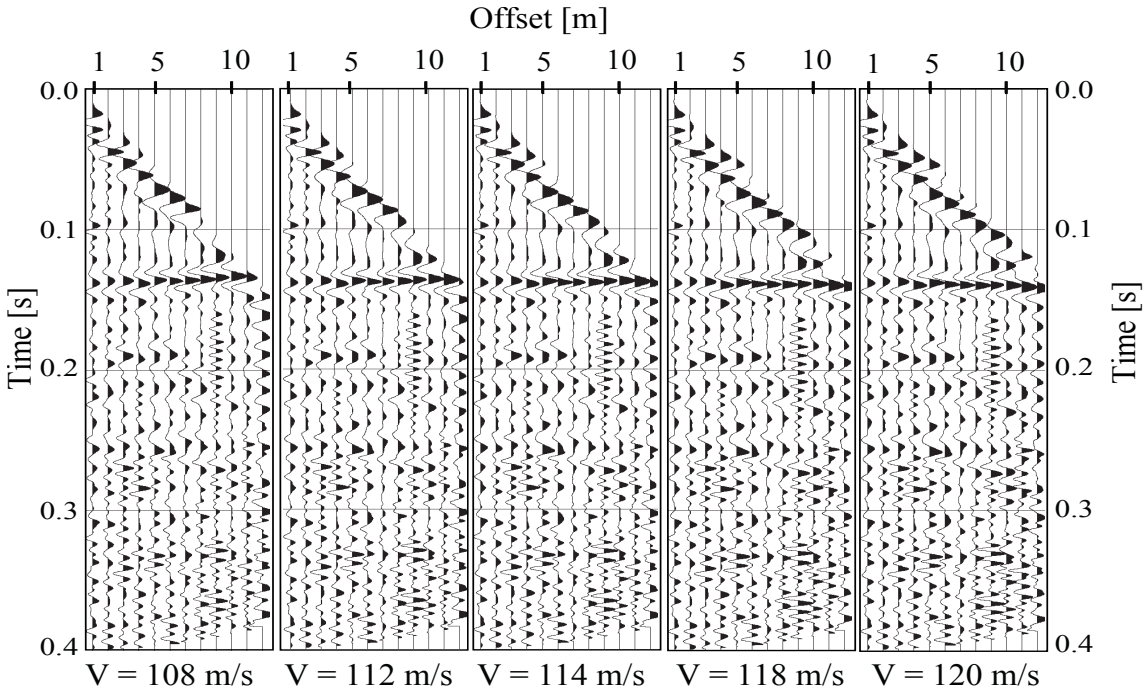

Figure 6.3: Constant velocity scan (velocity analysis) of CMP gather 92; it has been dynamically corrected using five different velocities to show the precision necessary during the velocity analysis stage of the processing flow. Stacking velocity of 114 m/s appears the best stacking velocity for the bedrock reflection (event *e* in Figure 6.2).

This event is actually the direct wave reflected by a structure placed towards the end of the seismic line (see the sketch of Figure 6.5b). Compared to the direct wave it has the same velocity (i.e. 92 m/s) but reversed moveout (see Figure 6.5c).

6.3 CRS processing

I performed the CRS processing inputing the same pre-processed data as used for the standard CMP procedure, supplying only minimal a priori information and avoiding any interactive procedure on the pre-stack data. The mean value (80 m/s) of near-surface velocities above the shallower reflector and the dominant frequency (80 Hz) of the reflected signals was the only a-priori information that I had to provide. However I found that the quality of the final CRS stacked section was very sensitive also to the stacking velocity range, which I set between 70-150 m/s, and to the coherence-analysis bandwidth that I set as being equal to the dominant period of the reflections (i.e. 15 ms).

I simply set the CRS aperture along the offset axis to vary between 1 m at 0.01ms to 12.5 m at 0.08 ms twt, in order to avoid the reduction on the number of available traces for the automatic coherence analysis. To evaluate the optimum CRS apertures along the midpoint direction I made several tests. Finally, I chose a midpoint aperture that increased with time from 1 m at 0.01 ms to 5 m at 0.4 ms twt. I checked that these values were smaller than the predicted size of the first Fresnel zone. I set the other CRS

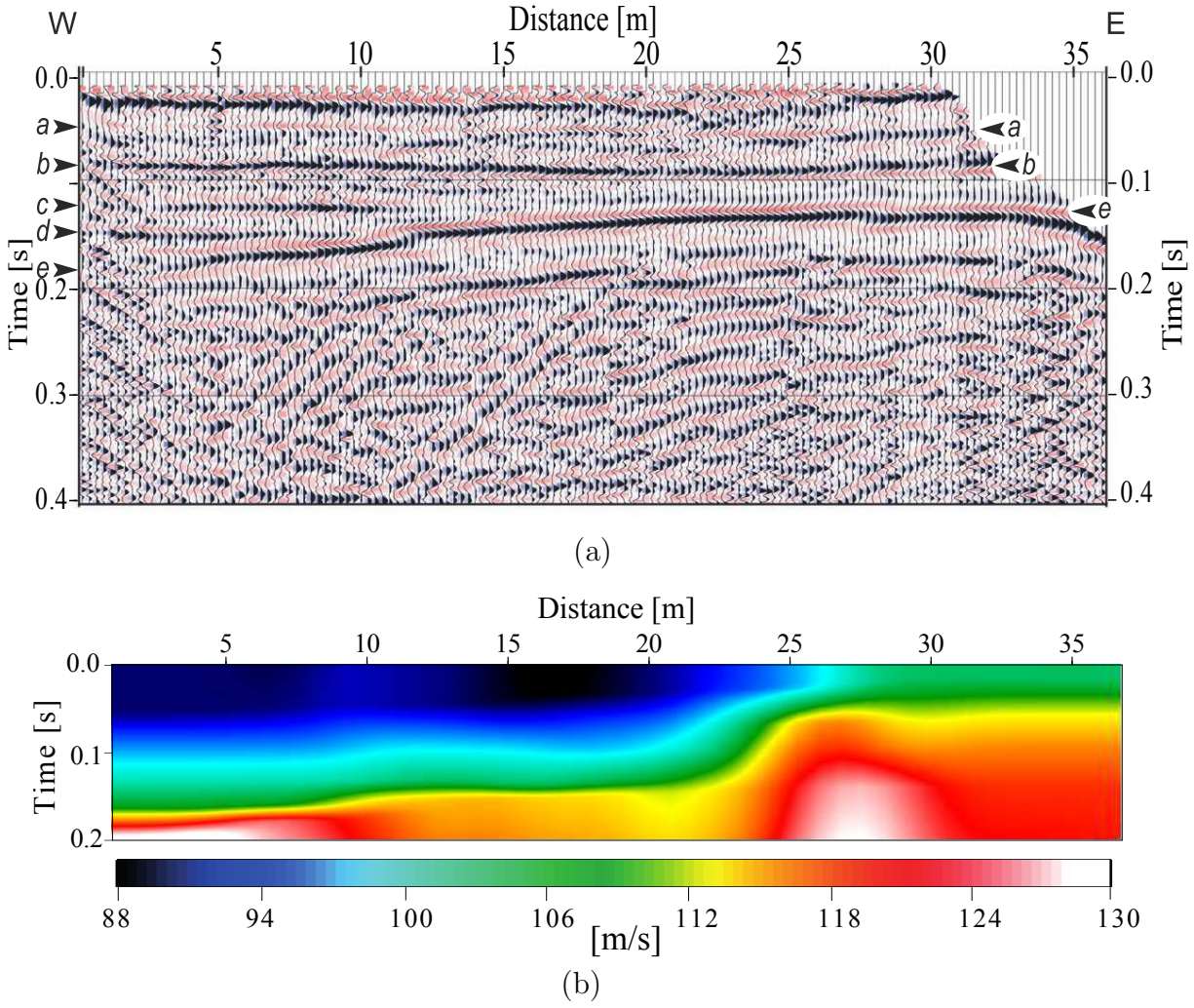

Figure 6.4: (a) CMP-stacked time section. All reflections appear resolved well throughout the section, and two of them show a very well-defined pinch-out with the bedrock. The shallowest reflection, however, is less clear: only the troughs (red) of the wavelet are clearly visible. (b) Velocity field used to apply the moveout correction to the time section.

processing parameters listed in Table 6.2 on the base of simple considerations similar to those reported for the P-wave data example in Chapter 5. In this case too many of them had only minimal influence on the quality of the final results and, therefore, are not analysed in detail.

In Figure 6.6 is displayed the comparison between the conventional NMO correction and the data-driven CRS moveout correction. It illustrates well, that the CRS stack process has achieved automatically and in a completely data-driven way, the same degree of accuracy obtained by the hand-picked velocity analysis. In other words, the CRS process determined automatically the stacking velocities with an accuracy of about 2 m/s. The lack of distortions due to the NMO-correction and the more contrasted amplitudes of the CRS-stacked trace than its CMP-stacked trace counterpart are also visible. I completed the CRS stack process applying the event-consistent smoothing of the CRS attributes

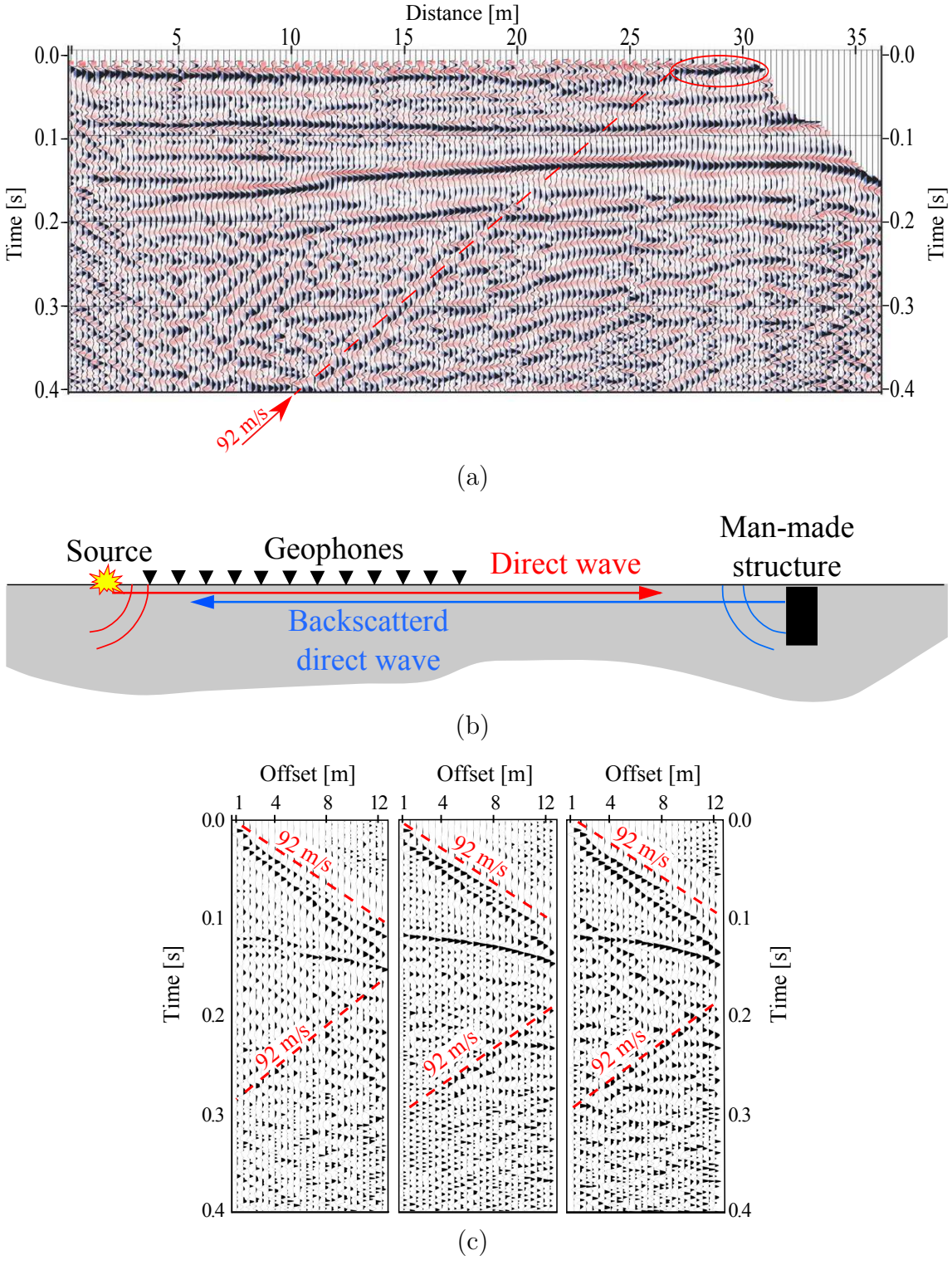

Figure 6.5: (a) the dipping event imaged on the stacked section; (b) a sketch to explain the linear event below 0.2 s; (c) Some shot records showing the event with the reversed moveout.

Context	Processing parameter	Setting
General Parameters	Dominant frequency	80 Hz
	Coherence measure	Semblance
	Data used for coherence analysis	Normalized traces
	Temporal width of coherence band	15 ms
Velocities	Near surface velocity	80 m/s
	Stacking velocities	70-150 m/s
Apertures and taper	Minimum midpoint aperture	0.5 m @ 0.01 s
	Maximum midpoint aperture	12.5 m @ 0.08 s
	Minimum ZO aperture	1 m @ 0.01 s
	Maximum ZO aperture	5 m @ 0.4 s
	Relative taper size	30 %
Automatic CMP stack	Number of refinement iterations	3
Linear ZO stack	Tested emergence angles	$-10\,^\circ \ldots 10\,^\circ$
	Initial emergence angle increment	$1\,^\circ$
	Number of refinement iterations	3
Hyperbolic ZO stack	Number of refinement iterations	3
Local optimization	Coherence threshold for smallest traveltime	0.0
	Coherence threshold for largest traveltime	0.0
	Maximum number of iterations	100

Table 6.2: Processing parameters used for the CRS stack process.

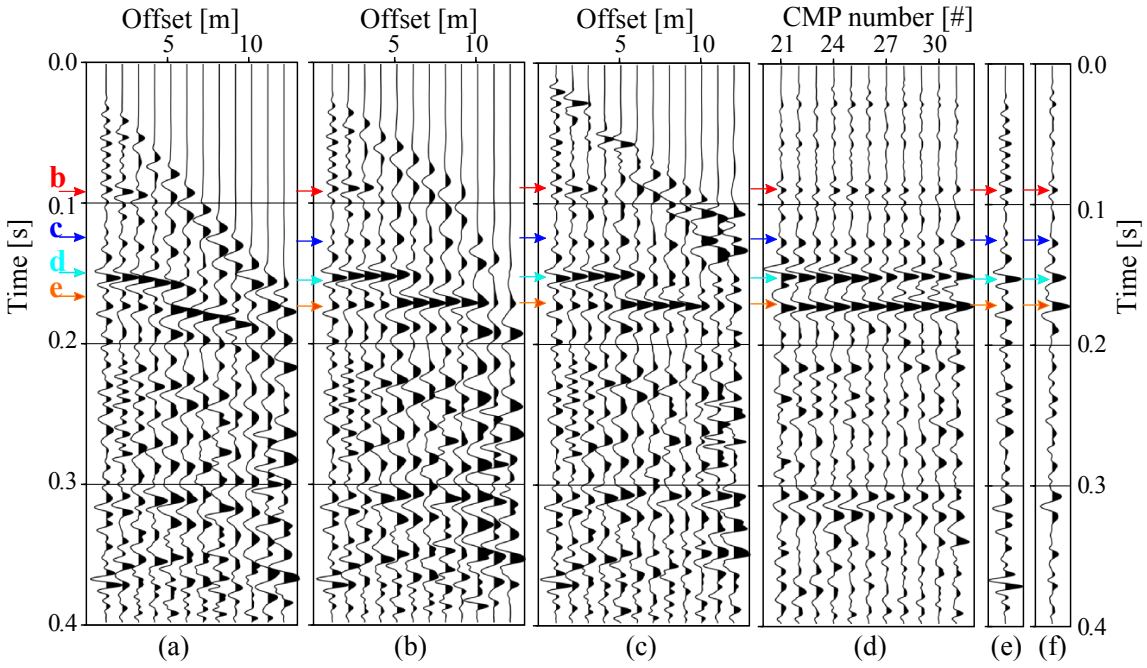

Figure 6.6: (a) CMP gather 26; (b) moved out gather using the conventional velocity analysis; (c) moved out gather using the NMO correction automatically performed by the CRS process; (d) subset of traces of the CRS supergather; (e) stacked trace at CMP 26; (f) CRS stacked traces at CMP 26.

Context	Processing parameter	Setting
Input	Data used for moveout correction	Original traces
	Moveout correction performed by	Optimized CRS attributes
	ZO section used as pilot traces	Optimized CRS stack
Cross correlation	Maximum correlation shift	2 ms
	ZO time used for cross correlation	0.08-0.18 ms
	Correlation weight	CRS semblance
	Minimum number of 'live' samples per traces	0
Estimation of Static Corrections	Data used for static correction estimation	Original correlation results
	Method applied	Center of area around local maximum
	Minimum number of contributions	sources:1, receivers:1

Table 6.3: Processing parameters used for the CRS-based residual static corrections.

[Mann and Duveneck, 2004] and the CRS-stack-based surface-consistent residual static corrections [Koglin et al., 2006].

Using a parallelogram shaped smoothing window with a spatial half-width of 1.5 m and a temporal half-width of 15 ms, I applied the smoothing process to all the ZO samples that exceeded a time-dependent coherence threshold linearly decreasing from 0.5, at twt = 0 ms, to 0.2 for twt = t_{max}. I set this threshold using the coherence section (not displayed) obtained after the first CRS iteration.

Afterwards, I used the resulting smoothed CRS parameter as input for the CRS-stack-based surface-consistent residual static corrections, which I estimated using the same maximum allowable static shift (2 ms) and cross-correlation traveltime window as used during the standard CMP processing (see Table 6.3). After each residual static correction iteration I applied to the updated, i.e. residual static corrected, data set a new CRS stack process, consisting of CMP stack, initial stack, optimized stack and event-consistent smoothing. The time shifts associated with the 61 source positions and the 85 receivers locations estimated after five loops of CRS-stack, event-consistent smoothing and CRS-based surface-consistent residual static corrections are displayed in Figure 6.7 together with the residual static corrections estimated during the CMP processing. A representative improvement on the continuity of the reflections obtained after this procedure is shown in Figure 6.8.

The final CRS stacked section is shown in Figure 6.9. All reflection events previously pointed out in Figure 6.2 are well imaged too. The events appear coherent and continuous and the shallowest reflection (event *a*) in particular has a greater continuity here than in the CMP stacked section. In addition, they appear quite consistent with the kinematic wavefield attributes evaluated by the CRS processing.

As expected the radius of curvature of the NIP-wave, R_{NIP}, increases smoothly with increasing recording time (i.e. of the depth) reaching up to the values of 10 m at 150

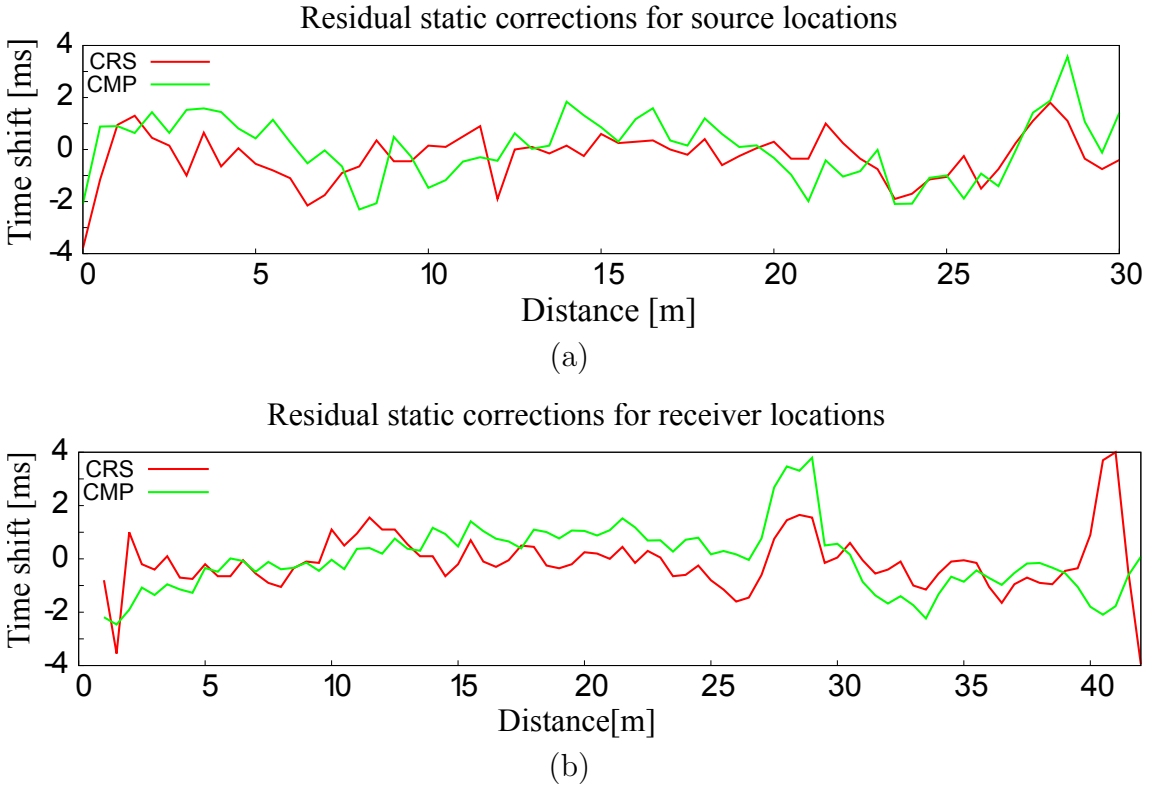

Figure 6.7: Accumulated static time shifts for the individual source (a) and receiver locations (b) after five iterations of the conventional (green) and the CRS-based (red) residual static corrections.

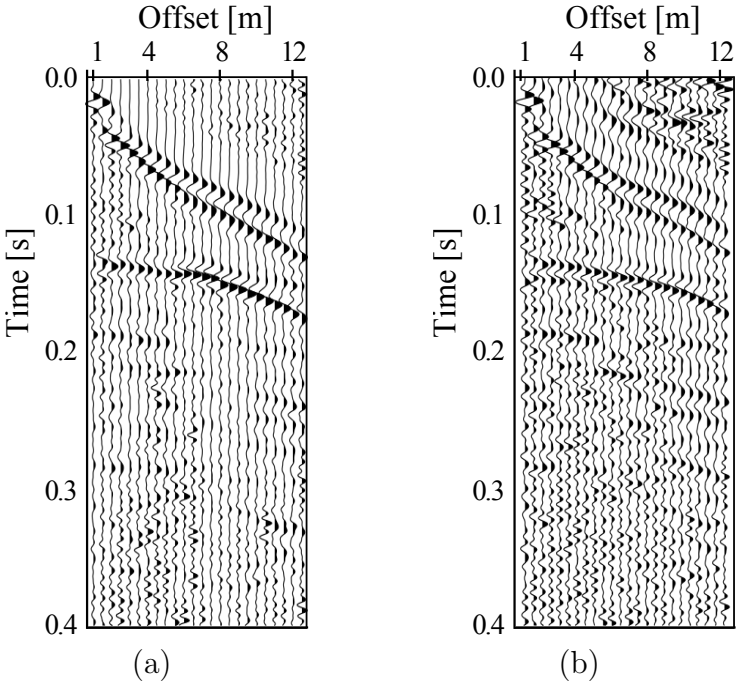

Figure 6.8: Shot gather #40 before (a) and after (b) the CRS-based residual static corrections. Note the significant improvement on the trace-to-trace continuity of the bedrock reflection.

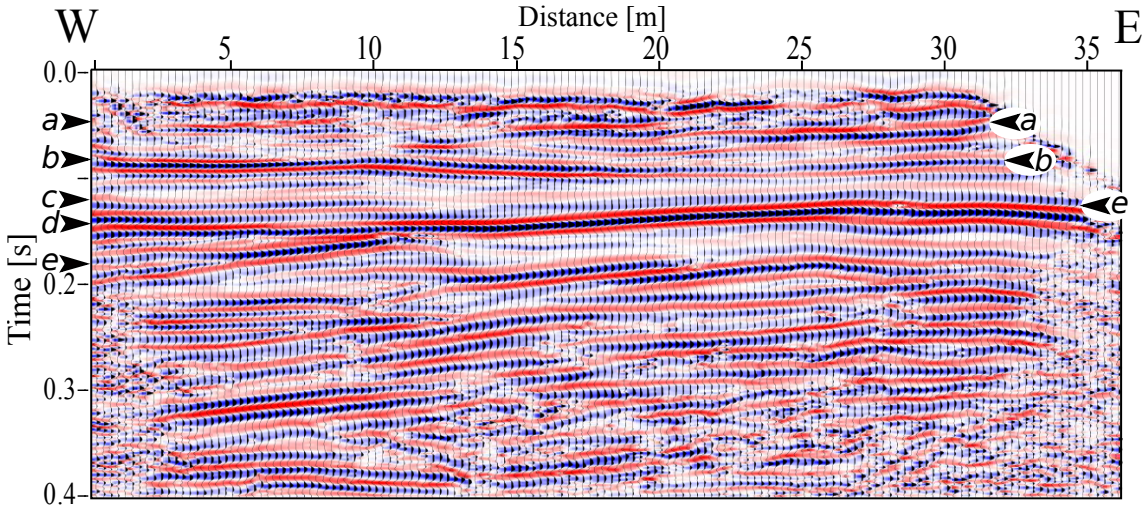

Figure 6.9: Optimized CRS stacked section.

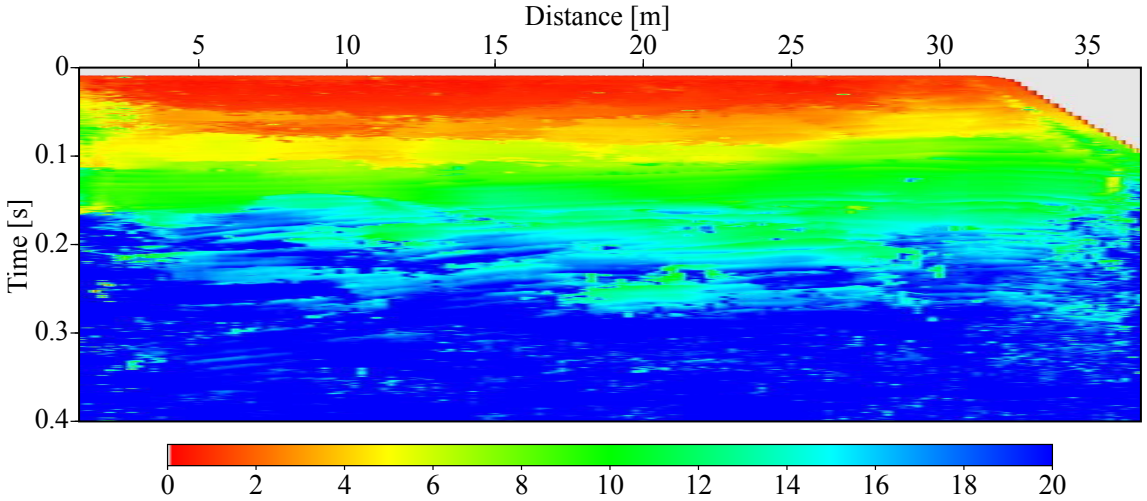

Figure 6.10: Radius of curvature for the NIP-wave, R_{NIP} [m].

ms twt (Figure 6.10). Likewise in the upper part of the section where the reflectors are almost flat the angle of emergence α, which is directly related to the slopes of the ZO events, assumes values around 0 ° while it reaches higher values at greater twt between 5 and 12 m along the seismic line, where the bedrock dips (see Figure 6.11). The presence of nearly planar reflectors is also clearly indicated by the small curvatures of the N-wave, $1/R_N$ (see Figure 6.12), which, being directly related to the curvature of the ZO events permits an easier interpretation than that of of the radius R_N itself. The reliability of the detected events as well as the associated wavefield attributes can be verified through the coherence section shown in Figure 6.13.

By analyzing both the CRS and CMP stacked sections it appears clear that for this high-resolution dataset the CRS process acted as a spatial high-cut filter which lowered the resolution of some parts of the stacked section. Due to this unwanted effect, the CRS stacked section appears more smoothed than the standard CMP section, as if it was the result of a post-stack mixing-trace processing step. Events *c* and *d*, for example, are not well resolved as in the CMP stacked section, and the pinch-out at the distance of about

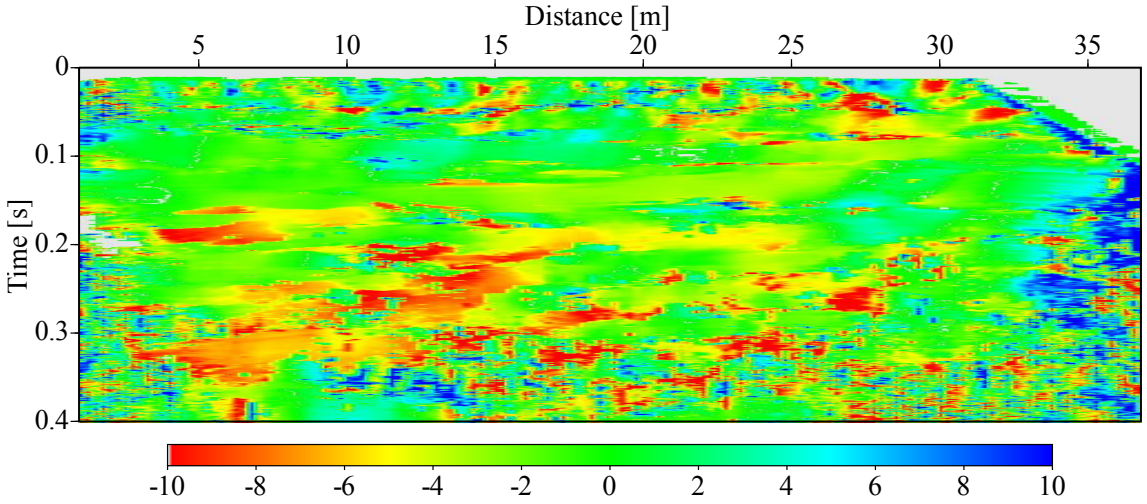

Figure 6.11: Angle of emergence α [deg] displayed from $-10\,^\circ$ to $+10\,^\circ$.

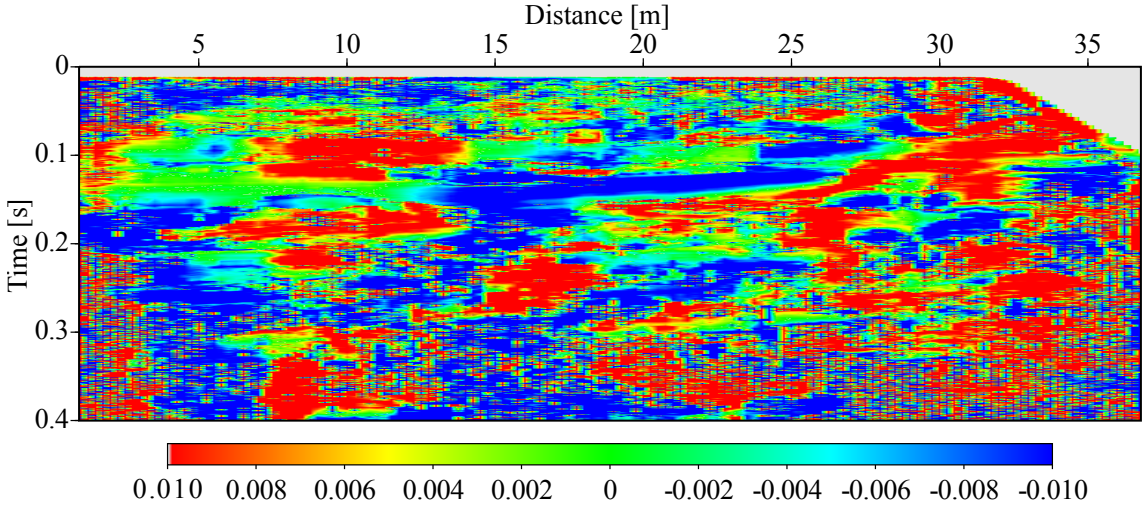

Figure 6.12: Curvature of the N-wave $1/R_N$ [m^{-1}] clipped from -0.01 to 0.01 m^{-1} to emphasise the small values.

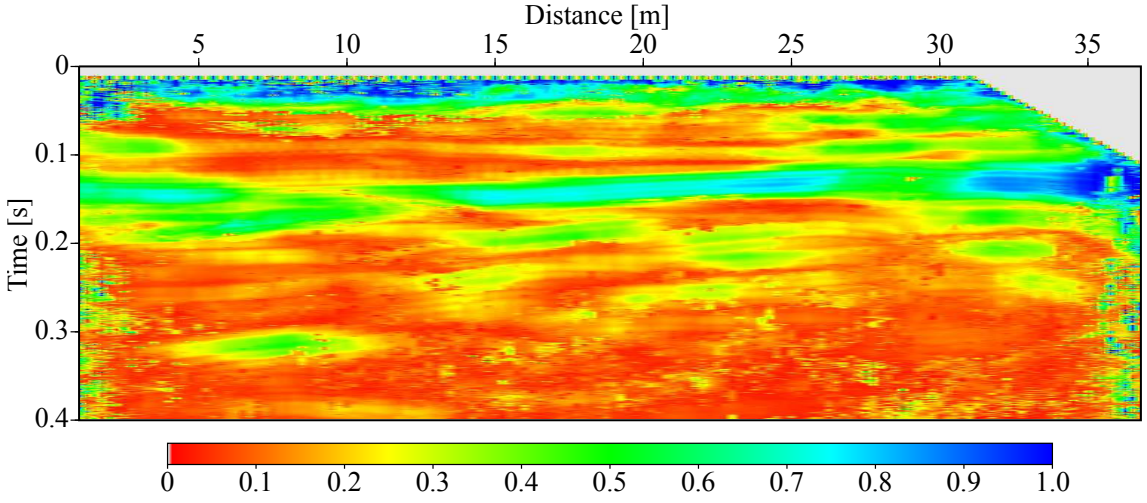

Figure 6.13: CRS coherence (semblance) section.

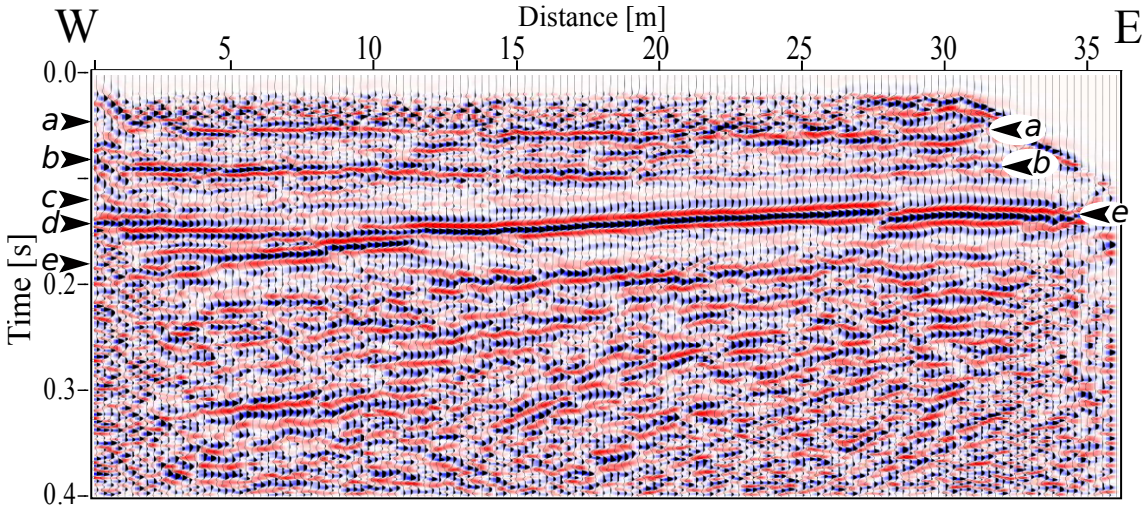

Figure 6.14: Automatic CMP stacked section.

11 m along the line is not imaged so well as in the CMP-stacked section (Figure 6.9 and Figure 6.4a respectively). In addition, compared to the standard CMP stack method the CRS processing also produced an enhancement of the bogus alignments of seismic energy below the bedrock, which as previously pointed out do not have match with the prestack data. Smaller midpoint apertures definitely would reduce both the smearing effect and the bogus alignments of seismic energy, but also the resolution with which the kinematic wave field attributes will be determined. This effect is well known from conventional stacking velocity analysis where large far offsets allow high resolution in stacking velocity estimation and, vice versa, small far offsets decrease the resolution with which stacking velocities can be estimated.

The CRS stack tries to find optimal midpoint apertures for every ZO sample using stacking parameters to estimate the projected Fresnel zone. However this is only a rough estimation, one which is not independent from the user-defined aperture and in addition neglects the dependency of the Fresnel zone on the dip of reflectors and from the change in frequency content of the signal with increasing of the twt. In practice the choice of the midpoint aperture must be considered as a trade-off between the best quality seismic resolution and the best obtainable reliability with which the kinematic wavefield attributes are estimated (that is, the highest S/N obtainable). This appears clear in the stacked section that I derived from the automatic CMP stack process (Figure 6.14). This is the first step of the CRS stack processing flow that operates on single CMP gathers through a one-parameter stacking operator basically identical to the conventional CMP stack process. Limiting the searching of the stacking parameters and the following stack process only to traces of single CMP gathers increases lateral resolution, but it lowers the signal-to-noise ratio. Note indeed, as in the resulting automatic CMP stacked section, the reflection events are not well imaged as in the CMP and CRS stacked sections. Conversely, limiting the stack process only to the traces belonging to single CMP gathers I obtained the section shown in Figure 6.15. It is worth noting that although it was obtained in an automatic way without any user interaction on the pre-stack data, this section appears very similar to the one derived through the conventional CMP stack process performed by hand.

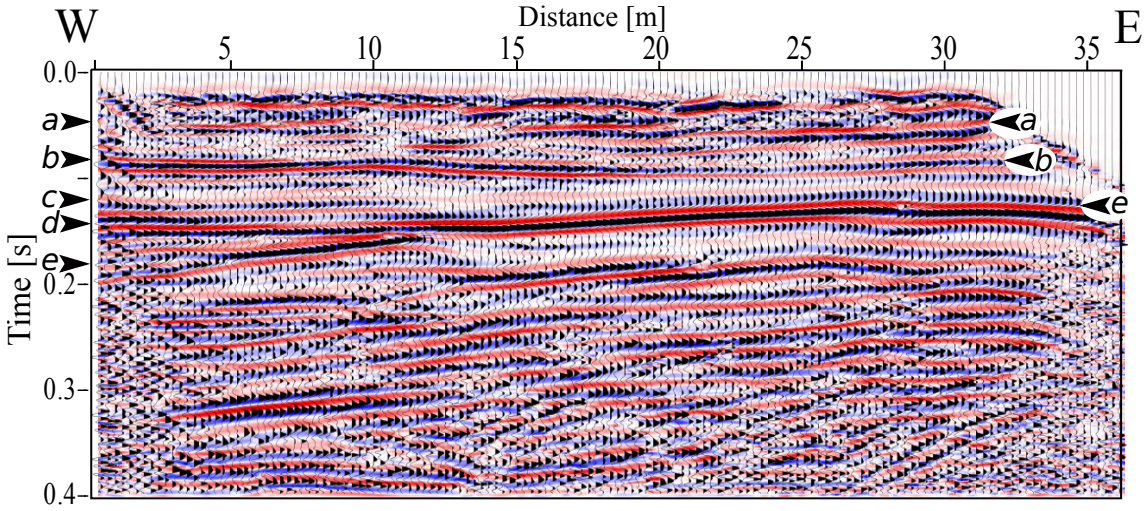

Figure 6.15: Stacked section obtained by limiting the stack to the traces of single CMP gathers.

From this latter section it also appears evident that the reduced number of stacked traces did not lead to a better defined pinch-out of events *d* with the bedrock. Probably, the highest semblance values found by the automatic coherence analysis do not coincide with the optimal stacking trajectories for a well-defined pinch-out. During the conventional velocity analysis instead, being completely user-driven, I could adjust visually the stacking in order to best focus the pinch-out. Therefore, to get similar results through the CRS processing, theoretically it would be sufficient finding the gain function that force the automatic search to detect the best stacking trajectories for a well defined pinch-out. Some tests carried out specifically to this purpose proved that various gain functions may help the CRS process to better resolve the pinch-out. This however comes at the cost of an overall decreasing in S/N ratio and resolution of all the other reflection events. This is probably because in near-surface seismic reflection datasets the amplitudes are generally subject to great changes along the seismic line, so that applying the same gain functions to the entire dataset is an ineffective way to improve the S/N ratio of some events without loosing that of the others. As for the midpoint aperture within the CRS processing the choice of the gain function to apply to the input dataset is a trade-off between wanted and unwanted effects.

6.3.1 CRS stacking velocities

Unlike the conventional CMP processing, the CRS process seeks to achieve optimal stacking parameters (α, R_{NIP}, R_N) for each time samples and all CMPs. This leads not to one velocity estimation for a given reflection event but rather to a set of velocity estimations for all time samples that constitute the ZO traces. The resulting velocity profile shows high-frequency variations with unreliable and unphysical results that render its use an impossibility [see e.g. Perroud and Tygel, 2005]. This appears clear when comparing the hand-picked velocities for the classical CMP velocity analysis with the one automatically determined with the CRS (Figure 6.16). To retrieve a meaningful stacking velocity field therefore it is necessary to perform a regularization process.

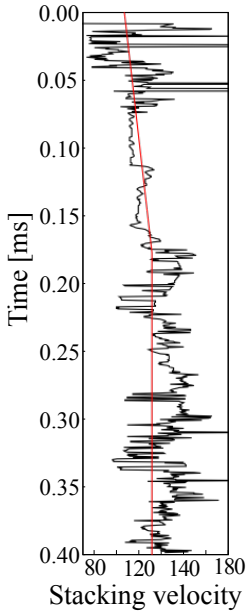

Figure 6.16: (a) V_{NMO} estimated picking by hand the velocity values of few selected events (red line). (b) V_{NMO} automatically estimated by the CRS code for all ZO sample of the considered trace (blue line).

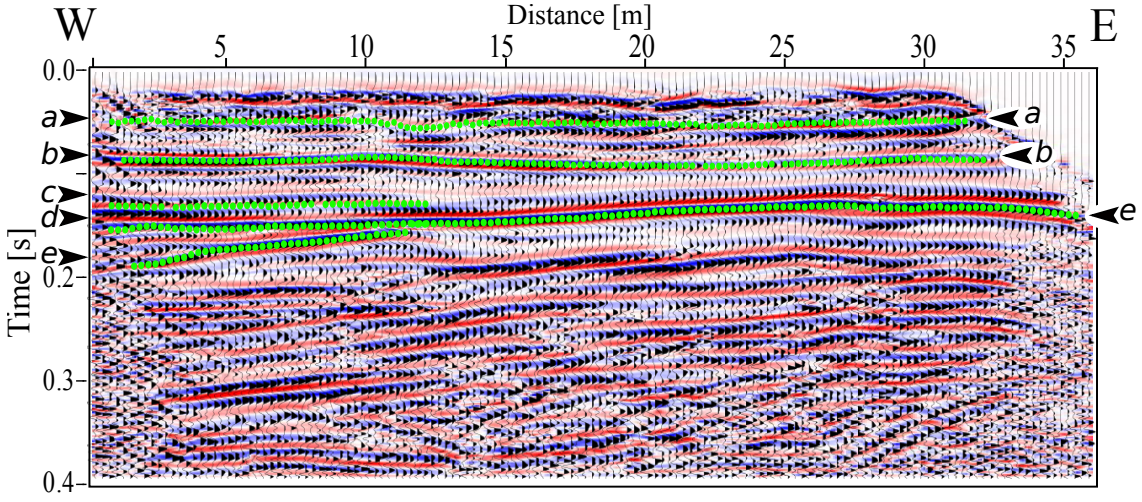

Figure 6.17: Input picks (green dots) for CRS stacking velocity estimation. The CRS stacked section was used for manual picking of reflection events.

For this data set I accomplished this by picking the twts and related CRS parameters (α, R_{NIP}) associated to actual reflection events directly on the CRS stacked section (see Figure 6.17). By doing this, the high S/N of the CRS stacked section better helped identify the actual reflections, while the coherence section was used to identify and to remove the outliers. Afterwards I used the picked CRS stacking parameters to calculate through Equation 4.37 the corresponding stacking velocity values, which were then linearly interpolated along time and midpoint directions via "smooth2", seismic processing routines provided by the Seismic Un*x (SU) package [Stockwell, 1997]. The obtained CRS velocity field (Figure 6.18) appears very similar to the one shown in (Figure 6.4a), it has approximately the same range of values, going from 88 to 130 m/s.

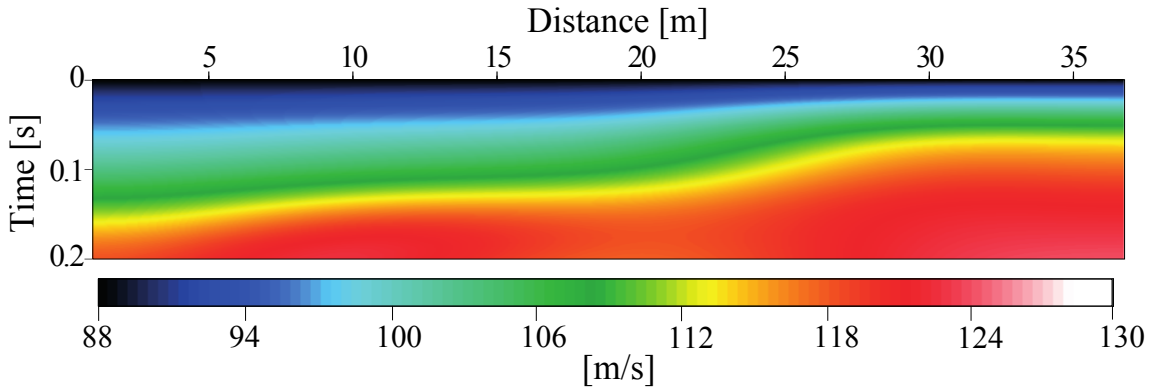

Figure 6.18: Final velocity field obtained from the CRS attributes after regularization. The colour velocity scale is the same used for Figure 6.4a, to allow an easier comparison between the velocity fields.

Chapter 7

Third example: crossing reflection events*

One of the difficulties that may be encountered during the processing of near-surface seismic reflection data is the presence of velocity gradients much greater than those observed in conventional deeper seismic surveys. These may occur at the transition between the unconsolidated sediments and the bedrock as well as across the water table as a direct consequence of the saturation [Elliott and Wiley, 1975; Miller and Xia, 1998]. In these near-surface scenarios the seismic velocities may range from as low as 200–300 m/s to 1600 m/s or more in the span of one or two seismic wavelengths [see e.g. Birkelo et al., 1987; Goforth and Hayward, 1992; Miller et al., 1989]. These dramatic velocity changes may lead to reflection hyperbolas that intersect each other at relative small offsets, which cannot be accurately CMP processed using the conventional NMO correction. Their NMO correction generates distortions and artefacts which appear on the NMO-corrected CMP gather as distinct events with characteristic linear and curved trajectories. To reduce these unwanted effects, which have always been regarded as a cause of reduction in the S/N ratio and temporal resolution of the stacked traces, some alternative NMO correction procedures aimed at maximizing the accuracy and the resolution of the stacked section have been proposed [see e.g. Brouwer, 2002; Masoomzadeh et al., 2010; Sloan et al., 2009]. Most of them proved to be quite effective but also rather complex to implement and/or very time-consuming.

Below, after a brief overview on these processing-related artefacts, I will show the results obtained using the CRS stack to process synthetic data with strong velocity gradients typically found in near-surface surveys.

*The results from this study together with the results from a real data set are going to be submitted for publication.

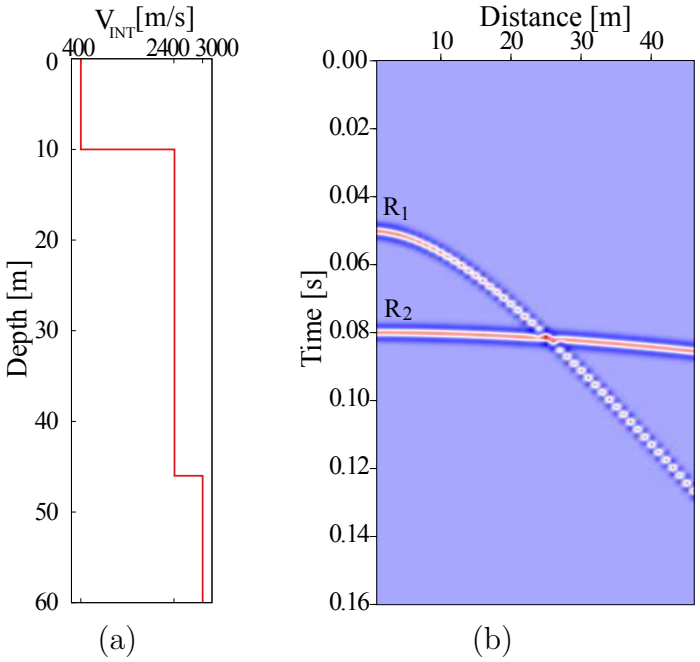

Figure 7.1: A three layer velocity model (a) and a synthetic CMP gather (b) simulated using the parameters in Table 7.1

7.1 Origin of the artefacts

To examine the fundamental reasons behind the apperance of artefacts from the NMO-correction of crossing reflections, I referred to a synthetic velocity model composed of a 10 m thick horizontal layer with an interval velocity of 400 m/s which overlays a second horizontal layer 50 m deeper, with interval velocity of 2400 m/s, placed above a homogeneous half space (Figure 7.1a). Figure 7.1b shows the simulated CMP gather, which I obtained from the previous model using a ray-tracing routine from the Seismic Un*x (SU) package [Stockwell, 1997] with the modelling parameters listed in Table 7.1. The reflections from the first and second interface, respectively R_1 and R_2, have zero-offset intercept time of 50 ms and 80 ms, with V_{NMO} of 400 m/s and 1500 m/s respectively. Because of the dramatic increase in interval velocity between the two layers, the reflection R_1 intersects the reflection R_2 at offset:

$$x_{int} = \sqrt{V_1^2 V_2^2 (t_{02}^2 - t_{01}^2)/(V_2^2 - V_1^2)} = 26\,\text{m} \tag{7.1}$$

The NMO velocity function that I obtained from the two reflection events is shown in Figure 7.2a, while the resulting unmuted NMO-corrected CMP gather is displayed in Figure 7.2b. New events, originally not present on the CMP gather, appear before, after and between the correctly flattened reflection events R_1 and R_2. The root of these "ghost" events is easily understood looking at the technique of the NMO correction process. This acts through the hyperbolic traveltimes calculated for each normal incidence ZO times t_0 using Equation 3.1, which for the NMO velocity displayed in Figure 7.2a are arranged as schematically displayed in Figure 7.2c. The relocation of the seismic energy from t_h to zero offset traveltime t_0 occurs by shifting along the time axis the samples

Modelling parameter	Setting
Receivers number	92
Receiver spacing	0.5 m
Record length	150 ms
Sampling interval	0.5 ms
Spread geometry	off-end
Minimum offset	0.5 m
Maximum offset	46 m
Dominant frequency	70 Hz

Table 7.1: Parameters used to model the data in Figure 7.1b.

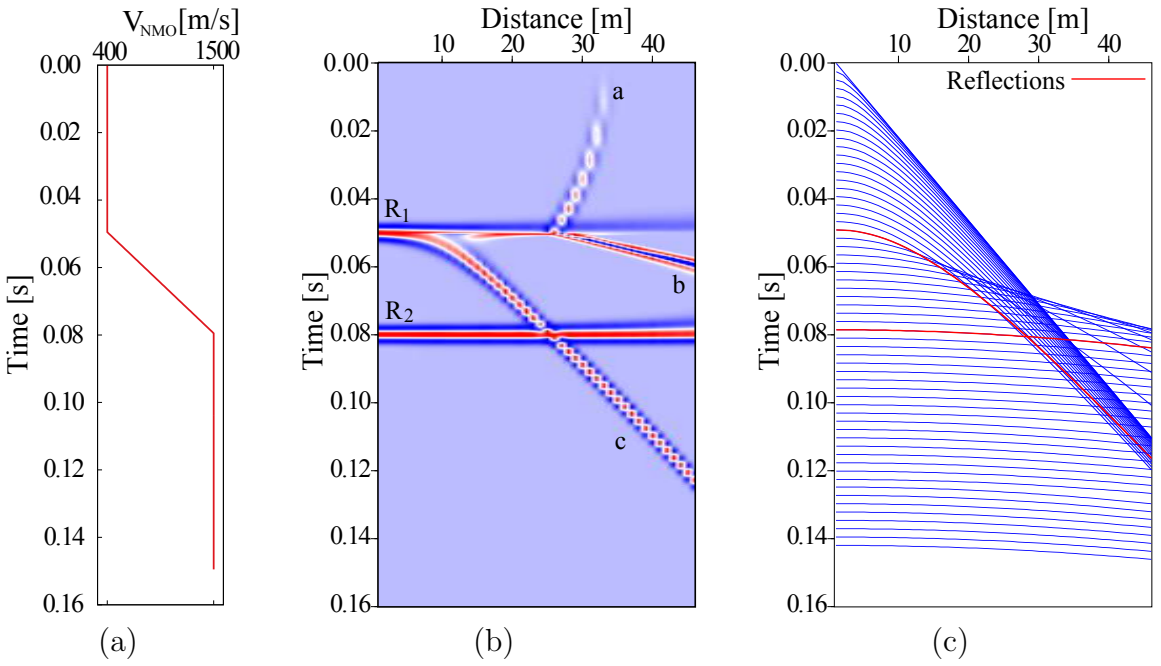

Figure 7.2: (a) NMO velocity function derived by the reflections R_1 and R_2. (b) CMP gather of Figure 7.1b after the NMO correction with the velocity function shown in Figure 7.2a. (c) Hyperbolic traveltimes (blue line) calculated every 0.004 s through Equation 3.1 using the V_{NMO} velocity function shown in Figure 7.2a.

lying along the NMO hyperbolas of $\Delta t_{NMO} = t_h - t_0$, i.e. of a time shift consistent with the assumed NMO velocity function. For the synthetic CMP gather with the crossing reflection events shown in Figure 7.1b, besides to align events R_1 and R_2, the NMO correction gives rise also to a number of artificial events marked in Figure 7.4 as *a*, *b* and *c*. Since the seismic energy was originally present only along the reflection hyperbolas, these new events are necessarily the reflected energy which has been wrongly re-mapped along coherent trajectories. Notably the energy recorded at offset $x_{int} < x < 36$ m with $V_{NMO} = 1500$ m/s along event R_2 is wrongly re-mapped along event *a* by the NMO curves calculated for traveltimes $t_0 < t_{01}$ with $V_{NMO} = 400$ m/s. Event *b* originates instead from the seismic energy originally recorded along the reflection event R_1 with $V_{NMO} = 400$ m/s, wrongly re-mapped by the NMO curves calculated with $V_{NMO} = 1500$

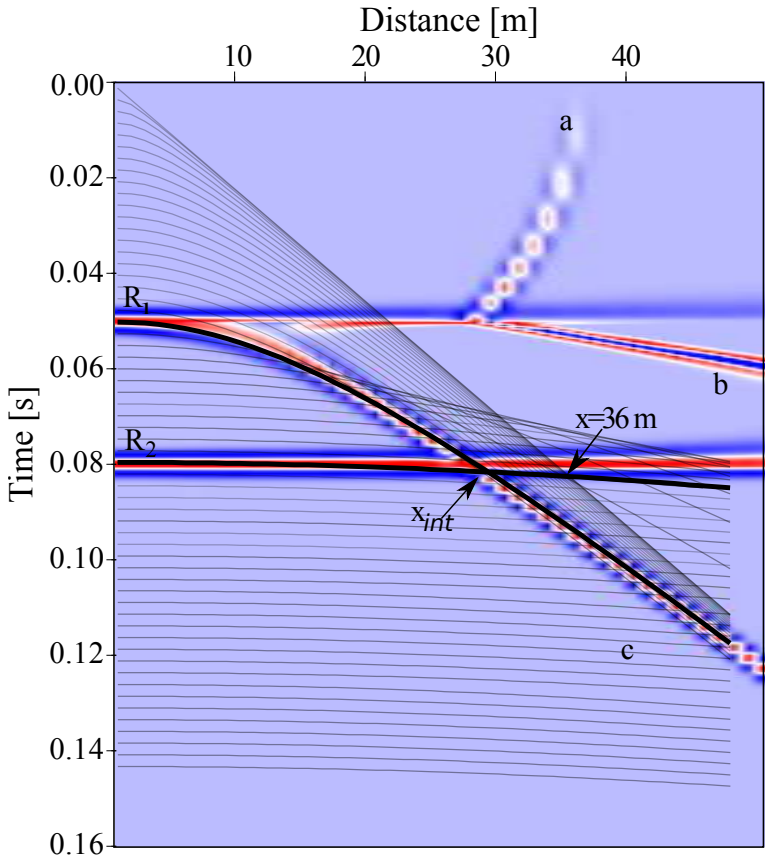

Figure 7.3: Technique of the NMO correction process. R_1 and R_2 are the reflections of Figure 7.1b after their NMO correction; a, b and c are instead the artefacts that the NMO correction has produced. The black lines displayed every 0.004 s are the hyperbolic traveltimes through which the NMO correction acts, while the original reflections are indicated as black bold lines

m/s for traveltimes $t_0 > t_{01}$. In other words, event a is the over-corrected part of event R_2 while event b is the under-correction of event R_1 (note indeed as it deviates only slightly from the reflection R_1). The high-frequency linear artefact is instead caused by the abrupt change in NMO velocities occurring at $t_{01} < t_0 < t_{02}$, which squeeze and the reverse along event c the wavelets originally recorded along event R_2 at offset $x > x_{int}$. The reversion and compression phenomena occur whenever the rate of change in V_{NMO} between two adjacent samples t_{0i} and t_{0i+1} violates the relationship:

$$v_{i+1} \leq \sqrt{\frac{x^2}{\frac{x^2}{v_i^2} + t_{0i}^2 - t_{0i+1}^2}} \tag{7.2}$$

Figure 7.2b shows also the stretching effect induced by the NMO correction within single wavelets, as well as the smearing effects produced by the intersection between reflections and artefacts. Further details and numerical examples concerning the above mentioned artefacts can be found in Miller and Xia [1998].

From this example it is easy to understand why the artefacts that arise from the NMO

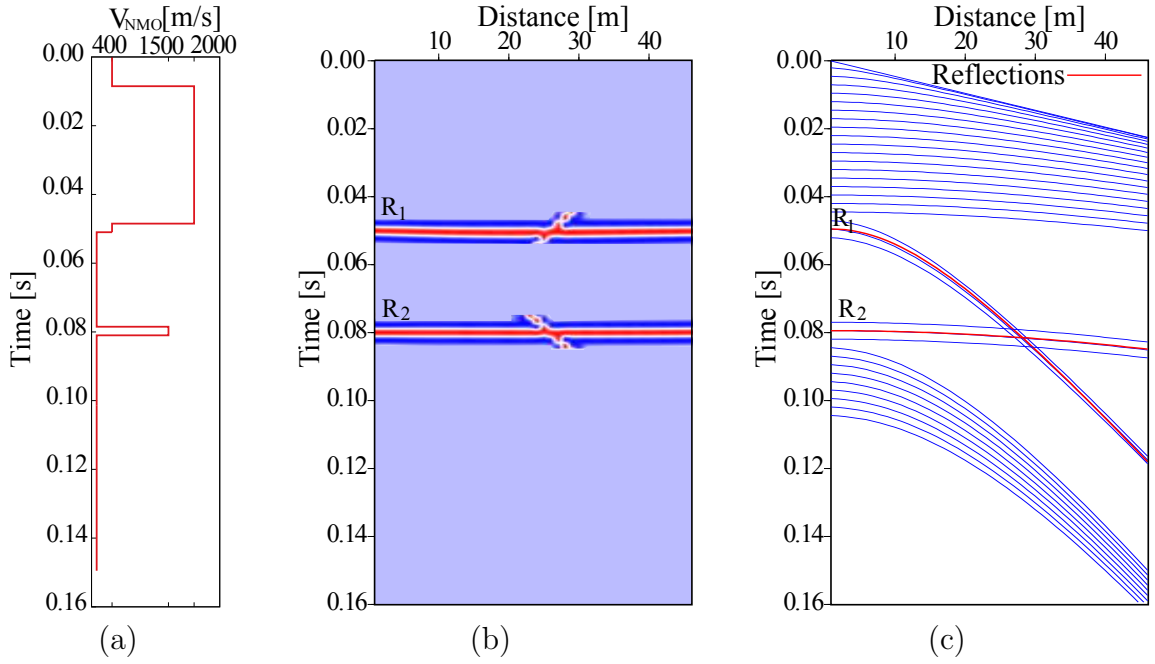

Figure 7.4: (a) V_{NMO} function expressly built to avoid the artefacts; (b) moved out reflections from the CMP gather in Figure 7.1b using the V_{NMO} depicted in 7.2b; corresponding NMO hyperbolas (c)

t_0	V_{NMO}
$t_0 < t_{01}$	$V_{NMO} > V_{R_2}$
$t_0 > t_{02}$	$V_{NMO} < V_{R_1}$
$t_{01} < t_0 < t_{02}$	$V_{NMO} = 0$

Table 7.2: Velocity values of the V_{NMO} function dispalyed in Figure 7.4a.

correction of crossing reflection events are mainly related to the V_{NMO} function rather than to the crossing reflection events themselves. It is a matter of fact that using the NMO velocity function of Figure 7.2a for the NMO correction of the two separate events similar results are obtained. To avoid this it is necessary to operate on the NMO velocity function rather than on the data itself. For the synthetic CMP gather previously considered, a possible V_{NMO} function suited to this purpose could be like one described on Table 7.2 and displayed in Figure 7.4a. Note, as the resulting NMO-corrected CMP gather (see Figure 7.4b) is completely free from artefacts. The reason clearly lays in corresponding NMO curves, the majority of which do not intersect the reflection events, thus avoiding the wrong re-mapping of the reflected energy (see Figure 7.4c).

Therefore, the optimum function for the NMO correction of reflection events that cross each other cannot be the one obtained by linear interpolation of the values picked from few selected events, as the resulting smoothness over the reflections gives rise to the artefacts previously described.

7.2 CRS stack of crossing reflection events

Data-oriented imaging methods like the CRS stack avoid the smoothed parameterization of the V_{NMO} as they perform a sample-by-sample data-driven velocity analysis without imposing any regularity constrain. The resulting V_{NMO} function may therefore allows more accurate NMO correction for data with large vertical velocity gradients.

To analyze this possibility, I input the synthetic CMP gather of Figure 7.1b to the automatic CMP stack process. This operates on single CMP gathers through a one-parameter stacking operator basically identical to the conventional CMP stack operator. However, unlike the conventional CMP stack method, the automatic CMP stack process evaluates the V_{NMO} separately for each normal incidence twt t_0 in a completely data-driven way, without imposing any degree of smoothness. The result of this process is shown on Figure 7.5. Compared to the conventional NMO correction, the automatic CMP stack process created less coherent artefacts, almost all of them confined between the two events, avoided event c, which is totally absent, and greatly reduced the smearing effects. The reason for this result can be easily understood looking at the NMO hyperbolas resulting from the NMO velocity function evaluated by the automatic CMP stack process (Figure 7.5c).

The data-driven implementation did not avoid the emergence of other artefacts which, however, appear different from those generated using the conventional V_{NMO}. Their origin lies in the hyperbolas by which the NMO correction is performed, which caused the over-correction of event R_1 and the under-correction of event R_2 (see Figure 7.6). How many hyperbolas will cause these artefacts depends on the extent of coherence bandwidth used during the coherence analysis. Compared to the artefacts produced by the NMO correction performed after the conventional velocity analysis, those generated by the CRS stack process are however less continuous and have high frequency. This makes them much easier to remove by the subsequent stack process.

7.3 Application to synthetic data

To test in a more comprehensive way the CRS stack method for near-surface data with strong velocity gradients like those that may be encounter in engineering and environmental investigations, I considered the subsurface ground model described by Deidda and Balia [2001]. The model consists of a cast-in-place concrete body lying at the bottom of a custom-dug trench in a clay-rich soil and below an overburden made up of filling material. It reproduces thus a three-layer case with a stiff layer trapped between two softer ones which is a target typically found in engineering, geotechnical and archaeological investigations. As reported by the authors in their case history, at the overburden/concrete interface the SH-wave velocity abruptly changes from 72 m/s to 400 m/s, exhibiting a velocity increase of about 500 %. According to the geometry of the model this strong velocity gradient leads to the intersection of the reflections from the top and the bottom of the concrete body. The originally recorded data, however, did not show such intersection, as the reflection events from the bottom of the concrete

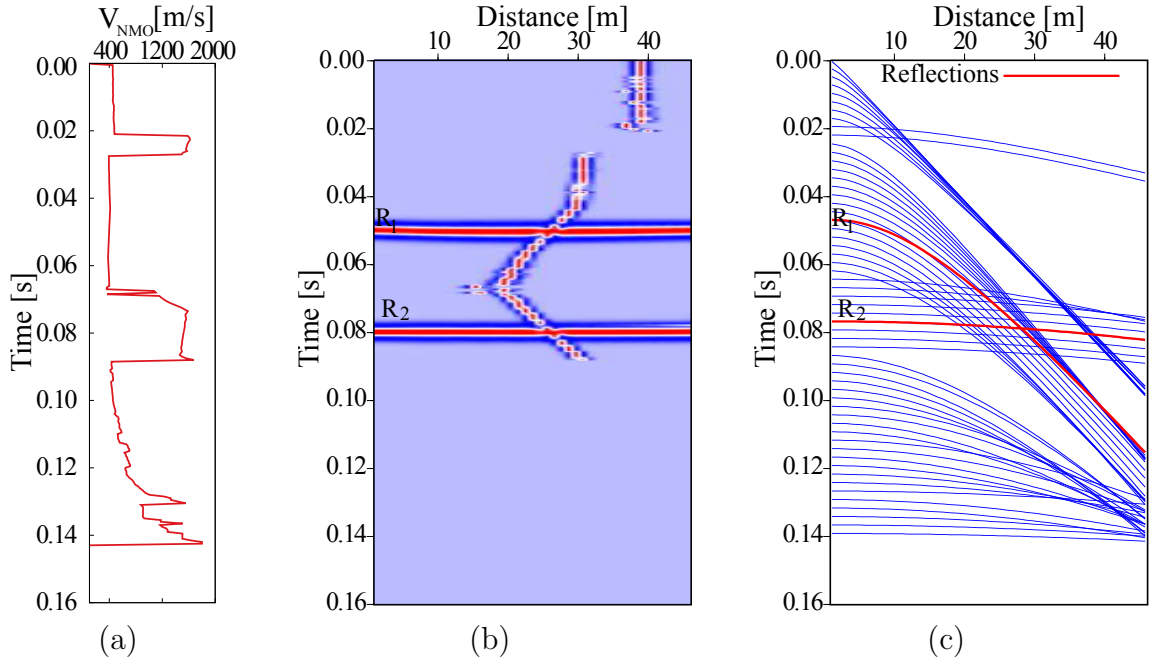

Figure 7.5: (a) The irregular V_{NMO} function as evaluated by the automatic CMP stack process; (b) same CMP gather of Figure 7.1b moved out with the irregular V_{NMO} evaluated by the automatic CMP stack process; hyperbolic traveltimes every 0.004 s resulting from the NMO velocity function depicted in Figure 7.5a.

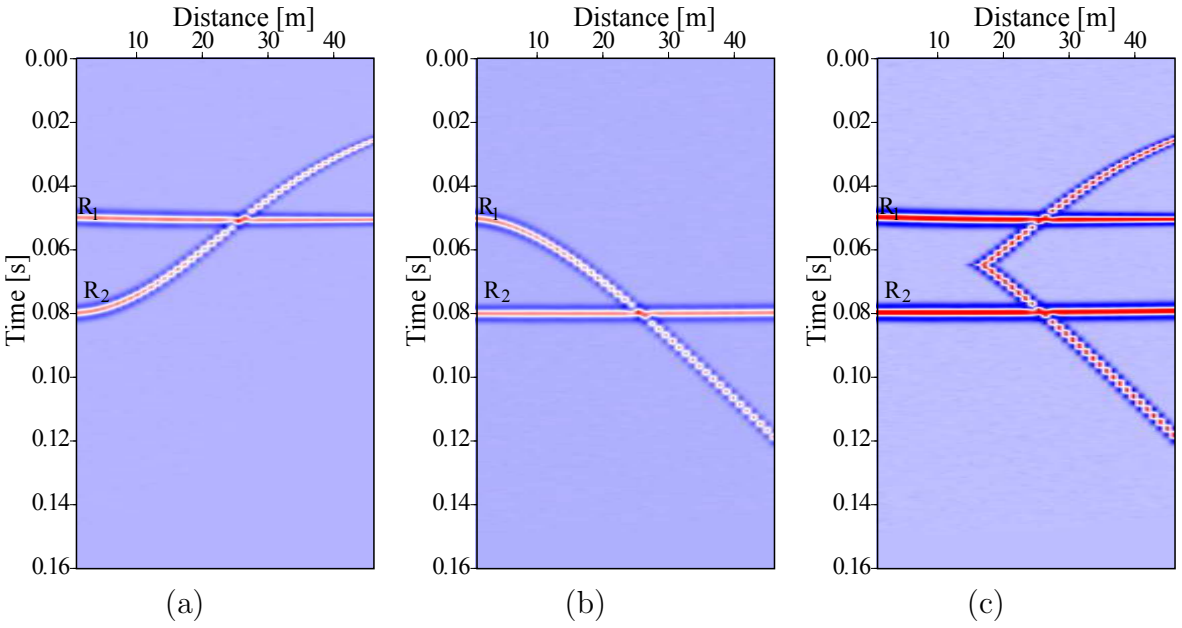

Figure 7.6: Moved out CMP gather of Figure 7.1b with $V_{NMO} = V_{NMO\,R_1} = 400$ m/s (a), with $V_{NMO} = V_{NMO\,R_2} = 1500$ m/s (b), and with $= V_{NMO} = V_{NMO\,R_1} = 400$ for $t_0 \leq 0.065$ s and $V_{NMO} = V_{NMO\,R_2} = 1500$ for $t_0 > 0.065$ s (c). The artefacts depends on how the stacking velocity function is before, between and after the intersecting events.

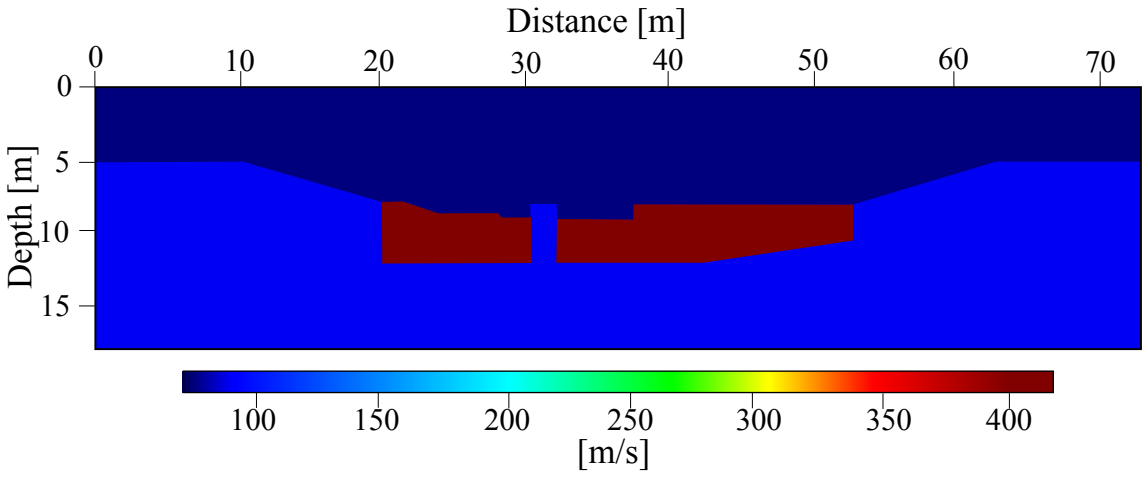

Figure 7.7: Synthetic SH-wave velocity model reproducing the ground model described by Deidda and Balia [2001]. Compared to the original one the thickness of the concrete body is increased of 2 m to better separate the reflections from the top and the bottom of the concrete body.

body were not recorded due to a lack of sufficiently high frequency content. The high attenuation properties of filling materials, as well as the inability of the sledgehammer to generate sufficient energy content in high frequency, resulted in a dominant frequency not exceeding 150 Hz [Deidda and Balia, 2001]. Conversely, a well-resolved reflection from the bottom interface of the model would have required dominant frequency content higher than 200 Hz. To overcome this intrinsic limitation of the originally recorded data, I built a synthetic data set with dominant frequency of 400 Hz.

For the synthetic modelling I used the acoustic/visco-elastic finite difference wavefield modelling code, freely available from the website of Jan Thorbecke (`http://janth.home.xs4all.nl`). I simulated the SH-wave propagation by implementing an acoustic scheme without imposing any attenuation. To avoid placing the sources and the receivers at the edge of the modelling grid, I shifted the model and the data acquisition plan to a depth of 5 m. In addition, within the first 5 m I set an absorbing boundary of 500 grid point with an exponential damping factor to minimize reflections from the edges as far as possible. Similar absorbing boundaries were also placed both at the flanks and at the bottom of the model. The resulting idealized velocity model is depicted in Figure 7.7. Compared to the original subsurface ground model, the thickness of the concrete body is increased of 2 m to better separate the reflections from the top and the bottom of the concrete body. To model the data I used a Ricker wavelet with a centre frequency of 400 Hz and maximum frequency approximately of 900 Hz. Being the maximum phase velocity $c_{max} = 400$ m/s, the minimum wavelength resulted $\lambda_{min} = 2.25$ m^{-1}. Therefore, in order to meet the stability and dispersion conditions expressed by Equations 7.3 and 7.4 I set the grid spacing $\Delta h = \Delta x = \Delta z = 0.01$ m and the time step $\Delta t = 1510^{-3}$ ms.

$$\Delta t \leq \frac{0.606 \Delta h}{c_{max}} \tag{7.3}$$

$$\Delta h \leq \frac{\lambda_{min}}{5} \tag{7.4}$$

Model parameters	Setting
Minimum velocity	72 m/s
Maximum velocity	400 m/s
Dominant source frequency	400 Hz
Maximum source frequency	900 Hz
Spatial discretization step	0.01 m
Time discretization step	1510^{-3} ms

Data parameters	Setting
Shot spacing	0.15 m
Receivers #	48
Receiver spacing	0.15 m
Spread geometry	off-end
Minimum offset	0.45 m
Maximum offset	7.5 m
Record length	250 ms
Sampling interval	0.5 ms
CMP #	646
Max fold	2400%

Table 7.3: Modelling parameters used to simulate the synthetic SH-wave velocity model and data.

To simulate the acquisition I modelled 300 shots with the same acquisition geometry of the original dataset, with a doubled number of receivers and halved distances between the source positions in order to obtain a 2400% nominal CMP-fold coverage twice that of the original dataset. In this way, besides avoiding the spatial aliasing, I improved the trace-to-trace continuity of both reflections and artefacts to better evaluate the performance of the CRS stack. The record length was 250 ms with a 0.5 ms sampling interval. The computation took about one and a half hour per shot. All the modelling parameters are listed in Table 7.3.

A representative modelled shot gather is shown in Figure 7.8. The reflection from the top of the concrete body arrives at 86 ms twt, intersecting at $x_{int} = 4.2$ m the reflected event with twt $t_0 = 105$ ms from the bottom of the concrete body. The direct wave with phase velocity of 72 m/s and the head-wave from the top of the concrete body with phase velocity of 400 m/s are also clearly visible. The several diffractions with reversal moveout, as well as the many non-primary events, are caused by the lack of attenuation in the modelling.

I performed the CRS processing using the processing parameters listed in Table 7.4, which were set on the base of similar considerations to those I reported for the CRS processing of the P- and SH-wave datasets. In Figure 7.9 the comparison between the CMP gather 450 (Figure 7.9a) after conventional NMO correction (Figure 7.9b) and after the data-driven moveout correction performed by the CRS stack process (Figure 7.9c) is shown. The improvement brought about by CRS is very noticeable. The obtained CRS stacked section is shown in Figure 7.10. Both the top and the bottom of the concrete body are imaged with high S/N ratio and reflection continuity. The image appears corrupted only by the diffractions, while the events artefacts produced by the CRS stack are completely removed.

The CRS stack, therefore, can be considered an alternative for processing of data exhibiting crossing reflection events, more easy to implement than the construction of complicated velocity function [e.g. Masoomzadeh et al., 2010] and/or the processing of separated events [e.g. Miller and Xia, 1998; Sloan et al., 2009]. Obviously being a

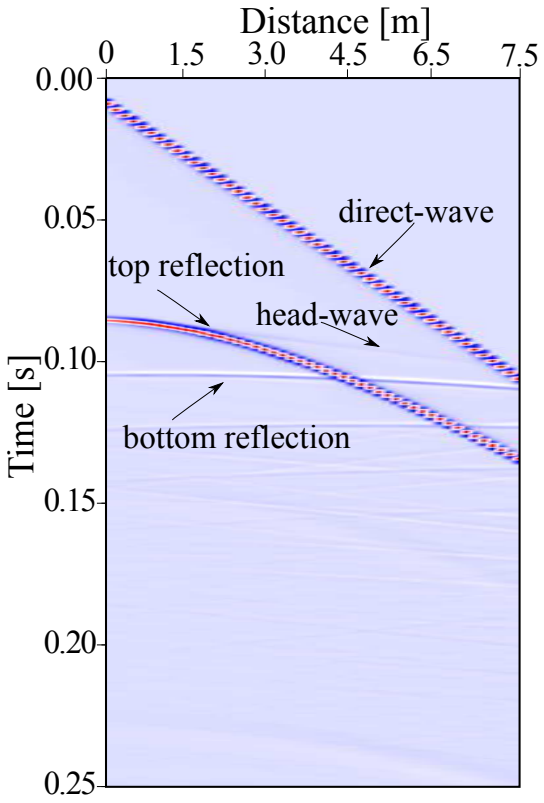

Figure 7.8: Representative shot gather obtained through the modelling.

Context	Processing parameter	Setting
General Parameters	Dominant frequency	400 Hz
	Coherence measure	Semblance
	Data used for coherence analysis	Normalized traces
	Temporal width of coherence band	5 ms
Velocities	Near surface velocity	70 m/s
	Stacking velocities	50-300 m/s
Apertures and taper	Minimum midpoint aperture	0.45 m @ 0.0 s
	Maximum midpoint aperture	7.5 m @ 0.0 s
	Minimum ZO aperture	0.05 m @ 0.0 s
	Maximum ZO aperture	0.375 m @ 0.2 s
	Relative taper size	30 %
Automatic CMP stack	Number of refinement iterations	3
Linear ZO stack	Tested emergence angles	$-55\,^\circ \ldots 55\,^\circ$
	Initial emergence angle increment	$1\,^\circ$
	Number of refinement iterations	3
Hyperbolic ZO stack	Number of refinement iterations	3
Local optimization	Coherence threshold for smallest traveltime	0.0
	Coherence threshold for largest traveltime	0.0
	Maximum number of iterations	100

Table 7.4: CRS processing parameters used to simulate the ZO stacked section.

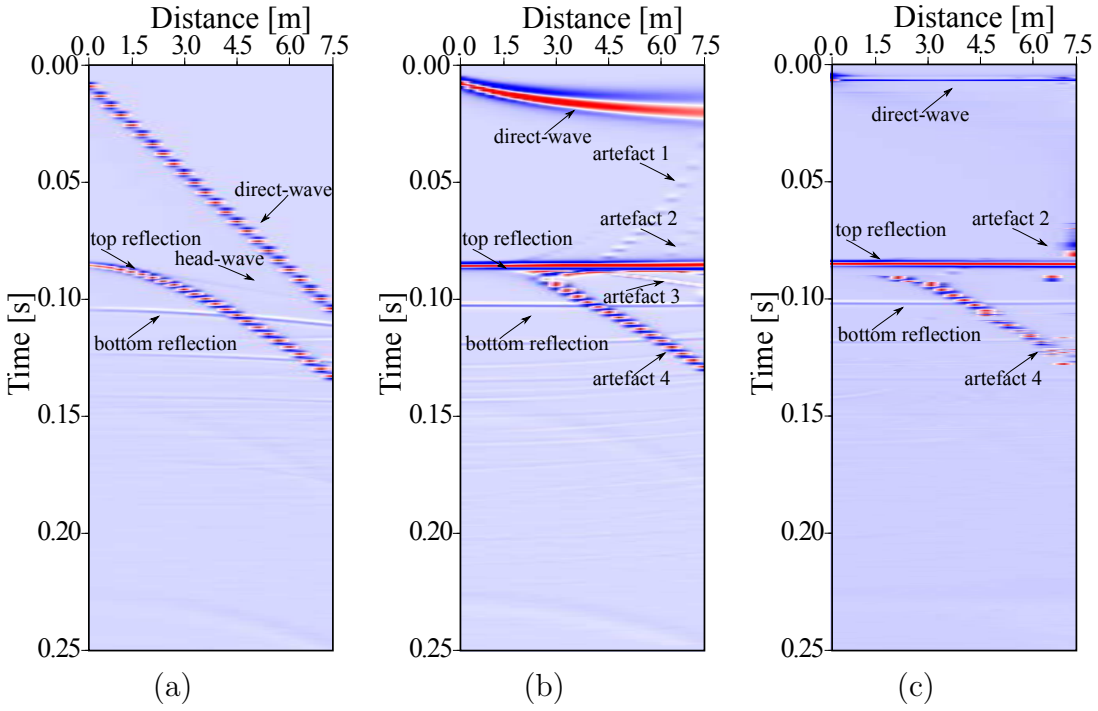

Figure 7.9: (a) CMP gather # 450. (b) CMP gather # 450 displayed without any stretch mute function after the NMO correction performed through the conventional velocity analysis. (c) CMP gather # 450 displayed without any stretch mute function after the automatic moveout correction performed by the CRS stack.

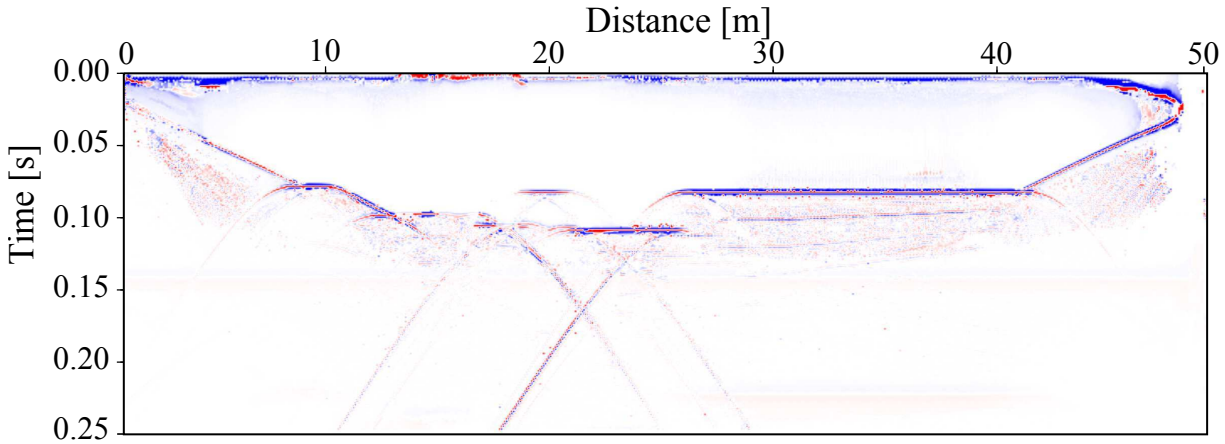

Figure 7.10: CRS stacked section obtained from the modelled data.

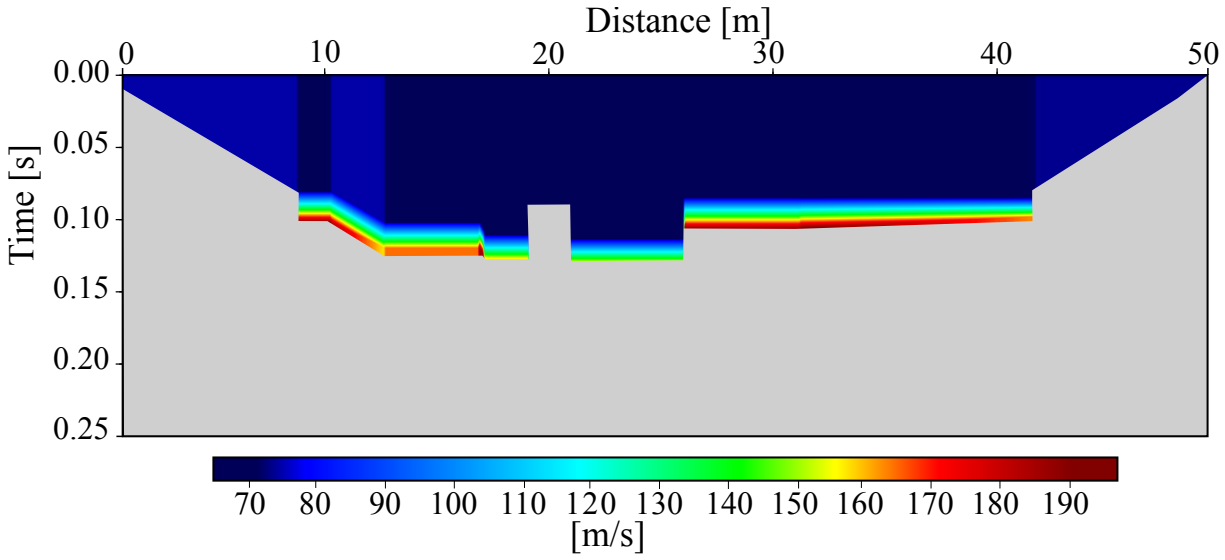

Figure 7.11: Stacking velocity field.Gray indicates absence of velocity information.

data-driven procedure, the artefacts generated by the CRS stack method will strongly depend on the properties of the dataset.

For the sake of thoroughness I also evaluated the performance of the conventional CMP stack method for the same set of synthetic data. Starting from the available information concerning the interval velocities and the geometry of the concrete body, I built the stacking velocity field of the data (see Figure 7.11). The resulting CMP stacked section obtained using a standard allowable stretch mute of 50 % is shown in Figure 7.12. It is easy to see that the CMP stacked section is not affected by artefacts produced by the NMO correction (see Figure 7.9b). Both the top and the bottom of the concrete body are well imaged with sufficiently accurate resolution. In fact in this case the stack of the CMP traces proved to be successful in removal of the artefacts produced by the NMO correction of reflection events that cross each other. Therefore, it is also likely that in other datasets the presence of crossing reflection events actually does not affect the S/N ratio and temporal resolution of the stacked section. If this were to happen however, the CRS represents a reliable method to avoid, or at least to reduce, these effects.

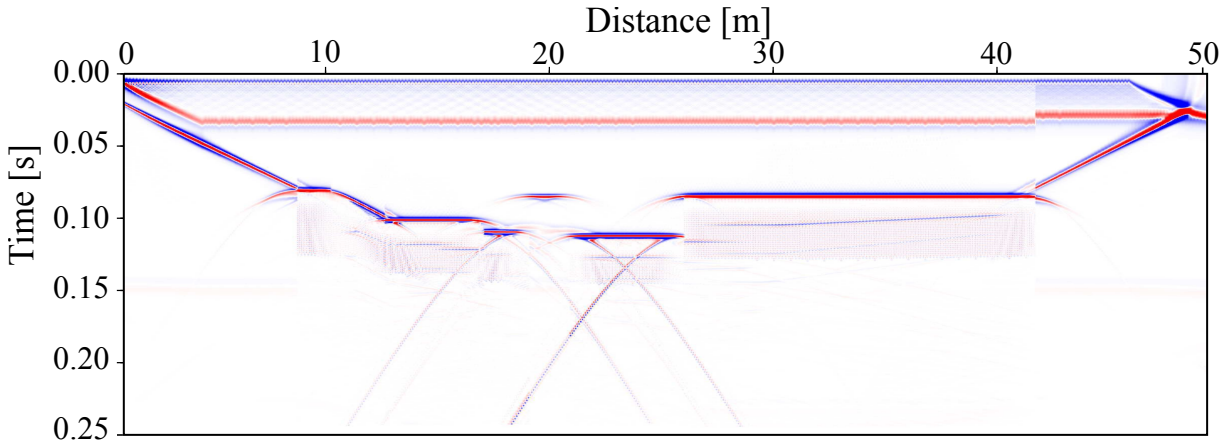

Figure 7.12: CMP stacked section obtained with the stacking velocity field shown in Figure 7.11.

Chapter 8

Conclusion and perspectives

8.1 Conclusion

The purpose of this PhD work was evaluate the possibilities of succesfully exporting the CRS stack from the exploration field to the shallow and ultrashallow field as means of reducing the cost for data processing, without sacrificing the quality and the resolution of the results.

The CRS stack has the advantage of producing a stacked section using more traces than the conventional CMP stack processing. In fact, it has a multiple-CMP fold along the midpoint direction as it stacks traces from multiple CMP gathers and it preserves higher-CMP fold along the offset direction, this because its data-driven implementation avoids the detrimental effects of the stretching process on shallow reflections at larger offsets. Additionally, it considerably restricts the generation of artifacts on data with strong velocity gradients. In this way, the CRS stack can achieve stacked sections with better S/N and reflection continuity than a CMP stack, without manual picking in velocity spectra or a priori information concerning the unknown macrovelocity model. Consequenlty, since the CRS-based surface consistent residual static corrections and the event-consistent smoothing of the stacking parameters can be also integrated into it, the CRS process achieves a high degree of automatization and lowers the costs for data processing.

In high-resolution shallow seismic reflection surveys however, stacking many traces from multiple CMP gathers could partially turn into a drawback. Near-surface materials often exhibit large horizontal and vertical velocity gradients as well as strong anelastic attenuation. As source-to-receiver offset increases, shallow and ultrashallow reflected traveltimes may exhibit distortions, rapid changes of amplitude and phase of signals and residual statics partially non surface-consistent. Moreover, since reflections from shallow and ultrashallow interfaces are often super-critical reflections, reflection coefficients become complex and induce other phase changes in reflected signals, making the solution of residual statics more complicated and not completely achievable. Therefore when summing many traces, reflected signals can undergo a high-cut filtering, which necessarily brings down seismic resolution, negatively affecting CRS parameters and as

a consequence the velocity field as well. Small geological discontinuities such as faults and/or pinch-outs may also lead the traces within a CRS-supergathers to mix together the different reflection events. The CRS stack tries to find optimal midpoint apertures for every ZO sample estimating the projected Fresnel zone. However, this is only a rough estimation that is not independent from the user-defined aperture and in addition, neglects the dependency of the Fresnel zone from the dip of the reflectors and that of the frequency from the increase of the time (depth). Poor S/N ratio and low fold coverage data may also give rise to bogus alignments of seismic energy which hinder the interpretation of the CRS stacked section. Smaller apertures should reduce these drawbacks but unfortunately they also lower the reliability of the stacking parameters and consequently the S/N of the stacked section. These drawbacks instead can be partially avoided by taking advantage of some of the information provided by CRS processing.

The results that I obtained applying the CRS stack process both to field data and to synthetic data clearly illustrate the benefits, drawbacks and solutions previously described.

The CRS stacked section, obtained from a P-wave dataset collected to delineate the hydrogeological framework of a paleolake environment, shows greater coherency and lateral continuity than the CMP section, but also a large number of false alignments, probably related to the high number of stacked traces, which hinder its interpretation. Weighting each sample of the CRS stacked section with the values of CRS coherence and number of CRS stacked traces proved to be a valuable solution. The resulting weighted section shows a remarkable S/N ratio improvement when compared to the CMP and stacked section and a considerable reduction in spurious alignments compared to the CRS stacked section. Therefore, although the weighting destroyed the original amplitude information, the weighted CRS stacked section appears to be more appropriate than the CRS and CMP stacked section in delineating the aquifer and its confining units.

The stacked section I obtained applying the CRS stack process to an ultrashallow high-resolution SH-wave dataset collected to support a geotechnical study, also clearly shows the smearing effect brought about by the CRS process. In fact, compared to the CMP stacked section, the CRS stacked section resulted excessively smoothed (i.e. smeared) with some reflector portions unresolved and not well defined pinch-outs. Conversely, the CRS stacked section obtained by restricting the stack process to only the traces within single CMP gathers, while preserving the use of the CRS-supergather for the search of stacking parameters, appears very similar to the very-detailed time section obtained through the conventional CMP process. Additionally, it was obtained in a few minutes without any processing efforts, unlike the CMP section, which required a very time-consuming stacking velocity analysis. Despite the reduced number of stacked traces the data-driven CRS imaging process did not find the optimal stacking trajectories that allow to well resolve, as in the CMP stack section, the pinch-out between the deepest overburden reflectors and the bedrock. These instead were found through the conventional velocity analysis process, which I drove (by-hand) to best focus the pinch-out. The CRS stack imaging process performed on datasets with specific gain functions provided a better-defined pinch-out, but at the cost of an overall decrease in S/N ratio and resolution of all the other reflection events. Probably, data with CMP gathers more

densely spaced and with higher fold of coverage would better drive the automatic CRS imaging process to a well-defined pinch-out.

Stacking and interval velocity fields were reconstructed as well, by inverting the kinematic wavefield attributes determined for each CRS stacking operation. The resulting velocity fields, which fit the velocities fields I had estimated in the CMP processing, however required more efforts than those required to produce the stacked sections, specifically in the P-wave case, for which I used the NIP-wave tomographic approach.

Using synthetic datasets with large vertical velocity gradients, like those often found in near-surface surveys, I tested the CRS stack method for data with reflection traveltimes that intersect each other at relatively small offsets. Unlike the conventional CMP processing, which cannot process accurately such crossing reflection events without generating distortions and artefacts, the data-driven CRS stack imaging process considerably restricted the generation of artefacts, thus avoiding any reduction of the S/N ratio and temporal resolution of the stacked traces. The CRS stack is therefore a reliable technique in order to avoid, or at least to reduce, the artefacts arising from the presence of crossing reflection events, definitely easier and faster than the construction of complicated velocity function and/or the processing of separated events.

On the basis of these results, I can certainly affirm that the greater cost efficiency of the CRS stack makes it a valuable alternative to the CMP stack, even if it entails losing a little resolution, for example when the aim is detecting small scale structures and/or when residual statics cannot be completely resolved. Nevertheless, as a result of increasing computing power availability, it is very likely that the CRS stack and/or new data-driven seismic processing methods developed for exploration data [see e.g. Bonomi et al., 2012; Fomel and Kazinnik, 2013] will quickly spread in the field of near-surface geophysics as well. This will substantially increase the cost-effectiveness of shallow seismic reflection methods and therefore their acceptance by engineers, geotechnicians, and hydrogeologists as a routine investigation tools.

8.2 Perspectives

To further validate the results and the remarks of this research work it would be helpful apply the CRS processing to datasets of better quality, namely with higher fold coverage and lower CMP spacings than those of the datasets presented in this work. This possibility is easily achievable with the high production rate data acquisition systems now available, and it is expected to further increase the performance of the CRS in overcoming some of the issues encountered with the datasets of this work.

Another practical future development would be the possibility of testing the CRS stack for real time processing of near-surface data. The real time processing is such an important objective that geophysicists as far back as 15 years ago had already hoped for achieving it [see e.g. Steeples et al., 1997]. This is particularly important in shallow surveys because efficient data acquisition can require dynamic adjustments. Recently, Heilmann et al. [2013] presented a cloud-computing solution combining the powerful

computational capabilities of a cloud infrastructure with a subsurface imaging workflow based on a parallelized grid version of the CRS stack. However, they have only simulated this possibility, while a real in-field data processing has not yet been accomplished and it is thus still expected.

From a theorectical point of view, possible expected future developments concern a better parametrizations of the CRS imaging algorithm to the processing of shallow seismic data, and the regularization and enhancing of the signal-to-noise ratio of prestack data by means of CRS-based tools. This point, however, needs further investigations.

Another possible topic of future research might also be the study of the influence of the search aperture in the CRS kinematic wavefield attributes, i.e. the so called spread-length bias, especially for data acquired in area characterized by strong P- and/or S-wave velocity contrasts. This is a mandatory requirement to validate the use of processing routines based on these quantities, such as poststack and/or prestack time or depth migration and time-to-depth conversion.

Appendix A

Used software

Preprocessing and CMP processing of the seismic data were carried out on a laptop using the Parallel Geoscience Corp.'s SPW seismic package.

The Wave Inversion Technology (WIT) consortium provided the softwares for CRS processing:

- 2D ZO CRS stack version 5.1.3 (implemented by Jürgen Mann);
- 2D NIP-wave tomography (by Duveneck [2004]);
- CRS-based residual static corrections (by Koglin et al. [2006]);
- event-consistent smoothing of CRS parameters (implemented by Eric Duveneck and modified by Markus von Steht and Zeno Heilmann (zeno@crs4.it);

For simple processing and visualisation of the data, the free Seismic Un*x (SU) package was used [Stockwell, 1997].

Additional figures were generated using the freely available programs gnuplot and inkscape.

The thesis was written using the typesetting system LaTeX on a PC with a free Debian-based Linux operating system.

List of Figures

List of Tables

References

Al-Chalabi, M., 1973, Series approximation in velocity and traveltime computations: Geophysical Prospecting, **21**, 783–795.

Ali, J. W., and I. A. Hill, 1991, Reflection seismics for shallow geological investigations: a case study from Central England: Journal of the Geological Society, **148**, 219–222.

Bachrach, R., J. Dvorkin, and A. Nur, 1998, High-resolution shallow-seismic experiments in sand, Part Ii: Velocities in shallow unconsolidated sand: Geophysics, **63**, 1234–1240.

Bachrach, R., and A. Nur, 1998, High-resolution shallow-seismic experiments in sand, Part I: Water table, fluid flow, and saturation: Geophysics, **63**, 1225–1233.

Baker, G. S., 1999, Processing near-surface seismic-reflection data: A Primer: Society of Exploration Geophysicists.

Baker, G. S., C. Schemeissner, D. W. Steeples, and G. R. Plumb, 1999, Seismic reflection from depth less than two meters: Geophysical Research Letters, **26**, 279–282.

Baykulov, M., S. Dümmong, and D. Gajewesky, 2011, From time to depth with crs attributes: Geophysics, **76**, S151–S155.

Benjumea, B., J. A. Hunter, J. M. Aylsworth, and S. E. Pullan, 2003, Application of high-resolution seismic techniques in the evaluation of earthquake site response, Ottawa Valley, Canada: Tectonophysics, **368**, 193–209.

Birkelo, B. A., D. W. Steeples, R. D. Miller, and M. S. Sophocleous, 1987, Seismic-reflection study of a shallow aquifer during a pumping test: Ground Water, **25**, 703–709.

Black, R. A., D. W. Steeples, and R. D. Miller, 1994, Migration of shallow seismic reflection data: Geophysics, **59**, 402–410.

Bonomi, E., G. Caddeo, A. M. Cristini, and P. Marchetti, 2012, Data-driven time imaging of 2D acoustic media without a velocity model: 82th Annual International Meeting, SEG, Expanded Abstracts, 1–5.

Bradford, J. H., 2002, Depth characterization of shallow aquifers with seismic reflection, Part I–The failure of NMO velocity analysis and quantitative error prediction: Geophysics, **67**, 89–97.

Bradford, J. H., L. M. Liberty, M. W. Lyle, W. P. Clement, and S. Hess, 2006, Imaging complex structure in shallow seismic-reflection data using prestack depth migration: Geophysics, **71**, B175–B181.

Bradford, J. H., and D. Sawyer, 2002, Depth characterization of shallow aquifers with seismic reflection, Part–I Prestack depth migration and field examples: Geophysics, **67**, 98–109.

Branham, K. L., and D. W. Steeples, 1988, Cavity detection using high-resolution seismic reflection methods: Mining Engineering, **40**, 115–119.

Brice, T., and J. Deere, 2008, An introduction to this special section: Seismic acquisition: The Leading Edge, **27**, 807–871.

Brouwer, J., 2002, Improved NMO correction with a specific application to shallow-seismic data: Geophysical Prospecting, **50**, 225–237.

Brouwer, J., R. Ghose, K. Helbig, and V. Nijhof, 1997, The improvement of geotechnical subsurface models through the application of S-wave reflection seismic exploration: 3rd EEGS Meeting, 103–106.

Bruno, P. P., A. Castiello, and L. Impronta, 2010, Ultrashallow seismic imaging of the causative fault of the 1980, M6.9, southern Italy earthquake by pre-stack depth migration of dense wide-aperture data: Geophysical Research Letters, **37**, L19302.

Büker, F., A. G. Green, and H. Horstmeyer, 2000, 3-D high-resolution reflection seismic imaging of unconsolidated glacial and glaciolacustrine sediments: processing and interpretations: Geophysics, **65**, 18–34.

Clague, J. L., J. L. Luternauer, S. E. Pullan, and J. A. Hunter, 1991, Postglacial deltaic sediments, southern Fraser River delta, British Columbia: Canadian Journal of Earth Science, **28**, 1386–1393.

Cox, M. J. G., 1999, Static Corrections for Seismic Reflection Surveys: Society of Exploration Geophysicists.

Deidda, G. P., and R. Balia, 2001, An ultrashallow SH-wave seismic reflection experiment on a subsurface ground model: Geophysics, **66**, 1097–1104.

Deidda, G. P., E. Battaglia, and Z. Heilmann, 2012, Common-reflection-surface imaging of shallow and ultrashallow reflectors: Geophysics, **77**, B177–B185.

Deidda, G. P., and G. Ranieri, 2001, Some SH-wave seismic reflections from depths of less than three meters: Geophysical Prospecting, **49**, 499–508.

Deidda, G. P., G. Ranieri, G. Uras, P. Cosentino, and R. Martorana, 2006, Geophysical investigation in the Flumendosa River Delta, Sardinia (Italy) – Seismic reflection imaging: Geophysics, **71**, B121–B128.

Deregowski, S. M., 1986, What is DMO?: First Break, **4**, 7–24.

Dix, C. H., 1955, Seismic velocities from surface measurements: Geophysics, **20**, 68–86.

Dolena, T. M., M. A. Speece, C. A. Link, and T. E. Duaime, 2008, A 3D seismic landstreamer system: Near Surface Geophysics, **6**, 21–29.

Dunkin, J. W., and F. K. Levin, 1973, Effect of normal moveout on a seismic pulse: Geophysics, **38**, 635–642.

Duveneck, E., 2004, Velocity model estimation with data-derived wavefront attributes: Geophysics, **69**, 265–274.

Elliott, S. E., and B. F. Wiley, 1975, Compressional velocities of partially saturated unconsolidated sands: Geophysics, **40**, 949–954.

Evison, F. F., 1952, The inadequacy of the standard seismic techniques for shallow surveying: Geophysics, **17**, 867–875.

First Break, 2011, Special topic - near surface geoscience: First Break, **29**, 68–100.

Fomel, S., and R. Kazinnik, 2013, Non-hyperbolic common reflection surface: Geophysical Prospecting, **61**, 21–27.

Geophysics, 1998, Special section - shallow seismic reflection papers: Geophysics, **63**, 1210–1450.

Ghose, R., J. Carvalho, and A. Loureiro, 2013, Signature of fault zone deformation in near-surface soil visible in shear wave seismic reflections: Geophysical Research Letters, **40**, 1074–1078.

Ghose, R., V. Nijhof, J. Brouwer, Y. Matsubara, Y. Kaida, and T. Takahashi, 1998, Shallow to very shallow, high-resolution reflection seismic using a portable vibrator system: Geophysics, **63**, 1295–1309.

Gierse, G., H. Trappe, J. Pruessmann, and G. Eisenberg-Klein, 2009, Enhanced velocity analysis, binning, gap infill, and imaging of sparse 2D/3D seismic data by CRS techniques: 79th Annual International Meeting, SEG, Expanded Abstracts, 3279–3283.

Goforth, T., and C. Hayward, 1992, Seismic reflection investigations of a bedrock surface buried under alluvium: Geophysics, **57**, 1217–1227.

Green, A. G., and J. A. Mair, 1983, Subhorizontal fractures in a granitic pluton - Their detection and implications for radioactive waste disposal: Geophysics, **48**, 1428–1449.

Green, A. G., and N. Soonawala, 1982, Detection of fracture zones in granites by geophysical logging and seismic reflection surveys, *in* of the OECD, N. E. A., ed., Geophysical Investigations in Connection with Geological Disposal of Radioactive Waste: Nuclear Energy Agency of the OECD, 21–28.

Guy, E. D., R. C. Nolen-Hoeksema, J. J. Daniels, and T. Lefchik, 2003, High-resolution SH-wave seismic reflection investigations near a coal mine-related roadway collapse feature: Journal of Applied Geophysics, **54**, 51–70.

Haeni, F. P., 1986, Application of continuous seismic reflection methods to hydrologic studies: Ground Water, **24**, 23–31.

Haines, S. S., 2006, Design and Application of an Electromagnetic Vibrator Seismic Source: Journal of Environmental and Engineering Geophysics, **11**, 9–15.

Hale, D., 1991, Dip Moveout Processing, Course Notes Series, Vol. 4: Society of Exploration Geophysicists.

Hasbrouck, W. P., 1991, Four shallow-depth, shear-wave feasibility studies: Geophysics, **56**, 1875–1885.

Hasbrouck, W. P., and N. Padget, 1982, Use of shear-wave seismic in evaluation of strippable coal resources: Utah Geological and Mineral Survey Bulletin, **118**, 203–210.

Hawman, R. B., and H. O. Ahmed, 1995, Shallow seismic reflection profiling over a mylonitic shear zone, Ruby Mountains-East Humboldt Range metamorphic core complex, NE Nevada: Geophysical Research Letters, **22**, 1545–1548.

Heilmann, Z., G. P. Deidda, G. Satta, and E. Bonomi, 2013, Real-time imaging and data analysis for shallow seismic data using a cloud-computing portal: Near Surface Geophysic, **11**, 407–421.

Helbig, K., 1987, Shear-waves - what they are and how they can be used, *in* Danbom, S. H., and S. N. Domenico, eds., Shear-wave exploration: Society of Exploration Geophysicists, Geophysical Development Series No 1, 19–36.

Herber, M. A., D. J. Runia, and K. Helbig, 1981, The shallow structure of the roggeplaat (The Netherlands) as deduced from high-resolution multi-channel profiling: Geology en Mijnbouw, **60**, 225–236.

Hertweck, T., J. Schleicher, and J. Mann, 2007, Data stacking beyond CMP: The Leading Edge, **26**, 818–827.

Hileman, J. A., P. Embree, and J. C. Pflueger, 1968, Automated static corrections: Geophysical Prospecting, **16**, 326–358.

House, J. R., T. M. Boyd, and F. P. Haeni, 1995, A case study for the acquisition, processing, and relevance of the 3-D seismic method as applied to near-surface concerns: 65th Annual International Meeting, SEG, Expanded Abstracts, 411–414.

Hubral, P., 1983, Computing true amplitude reflections in a laterally inhomogeneous earth: Geophysics, **48**, 1051–1062.

Hubral, P., and T. Krey, 1980, Interval velocities from seismic reflection time measurements: Society of Exploration Geophysicists.

Hunter, J. A., S. E. Pullan, R. A. Burns, R. M. Gagne, and R. L. Good, 1984, Shallow seismic reflection mapping of the overburden-bedrock interface with the engineering seismograph - Some simple techniques: Geophysics, **49**, 1381–1385.

Höcht, G., 2002, Traveltime approximations for 2D and 3D media and kinematic wavefield attributes: PhD thesis, University of Karlsruhe.

Höcht, G., E. de Bazelaire, P. Majer, and P. Hubral, 1999, Seismics and optics: hyperbolae and curvatures: Journal of Applied Geophysics, **42**, 261–281.

Inazaki, T., 1999, Land Streamer: A New System for High-Resolution S-Wave Shallow Reflection Surveys: 12th Annual Symposium on the Application of Geophysics to Engineering and Environmental Problems, SAGEEP, 207–216.

———, 2004, High resolution reflection surveying at paved areas using S-wave type land streamer: Exploration Geophysics, **35**, 1 – 6.

Jefferson, R. D., D. W. Steeples, R. A. Black, and T. Carr, 1998, Effects of soil-moisture content on shallow-seismic data: Geophysics, **63**, 1357–1362.

Jäger, R., J. Mann, G. Höcht, and P. Hubral, 2001, Common-reflection-surface stack: Image and attributes: Geophysics, **66**, 97–109.

Koglin, I., J. Mann, and Z. Heilmann, 2006, CRS-stack-based residual static correction: Geophysics, **54**, 697–707.

Kourkafas, P., and N. R. Goulty, 1996, Seismic reflection imaging of gypsum mine workings at Sherburn-in-Elmet, Yorkshire, England: European Journal of Environmental and Engineering Geophysics, **1**, 53–63.

Kozyrev, V., A. Zhukov, I. Korotkov, and A. Zhukov, 2004, An interactive solution for resolving mid-wavelength statics anomalies: The Leading Edge, **23**, 270–274.

Kurahashi, T., and T. Inazaki, 2006, A seismic reflection survey using S-wave vibrator for an active fault: Civil Engineering Journal, **91**, 52 – 57.

Lanz, E., A. J. M. Pugin, A. G. Green, and H. Horstmeyer, 1996, Results of 2- and 3-D high-resolution seismic reflection surveying of surficial sediments: Geophysical Research Letters, **23**, 927–938.

Levin, F. K., 1971, Apparent velocity from dipping interface reflections: Geophysics, **36**, 510–516.

Liberty, L., 1998, Seismic reflection imaging of a geothermal aquifer in an urban setting: Geophysics, **63**, 1285–1294.

Liner, C. L., 1999, Concepts of normal and dip moveout: Geophysics, **64**, 1637–1647.

Mair, J. A., and A. G. Green, 1981, High-resolution seismic reflection profiles reveal fracture zones within a "homogeneous" granite batholith: Nature, **294**, 439–442.

Mann, J., 2002, Extension and application of the Common Reflection Surface Stack method: PhD thesis, University of Karlsruhe.

Mann, J., and E. Duveneck, 2004, Event-consistent smoothing in generalized high-density velocity analysis: 74th Ann. Internat. Mtg., Soc. of Expl. Geophys., 2176–2179.

Mann, J., and G. Höcht, 2003, Event-consistent smoothing in generalized high-density velocity: 65th Exhibition and Conference, EAGE, Session P007.

Mann, J., J. Rainer, T. Müller, G. Höcht, and P. Hubral, 1999, Common reflection-surface stack – a real data example: Journal of Applied Geophysics, **42**, 301–318.

Marsden, D., 1993a, Static corrections-a review, part 1: The Leading Edge, **12**, 43–49.

———, 1993b, Static corrections-a review, part 2: The Leading Edge, **12**, 115–120.

Masoomzadeh, H., P. J. Barton, and S. C. Singh, 2010, Nonstretch moveout correction of long-offset multichannel seismic data for subbasalt imaging, Example North Atlantic: Geophysics, **75**, R83–R91.

Mayne, W. H., 1962, Common reflection point horizontal data stacking techniques: Geophysics, **27**, 927–938.

McCormack, M. D., and R. H. Tatham, 1986, Shear-wave exploration seismology: Society of Exploration Geophysicists, Continuing Education Program, Course Notes.

Miller, R. D., 1992, Normal moveout stretch mute on shallow-reflection data: Geophysics, **57**, 1502–1507.

Miller, R. D., S. E. Pullan, D. W. Steeples, and F. J. W. Hunter, 1994, Field comparison of shallow P-wave seismic sources near Huston, Texas: Geophysics, **59**, 1713–1728.

Miller, R. D., and D. W. Steeples, 1986, Shallow structure from a seismic-reflection profile across Borah Peak, Idaho, fault scarp: Geophysical Research Letters, **13**, 927–938.

———, 1991, Detecting voids in a 0.6-m coal seam, 7 m deep, using seismic reflection: Geoexploration, **28**, 109–119.

Miller, R. D., D. W. Steeples, and M. Brannan, 1989, Mapping a bedrock surface under dry alluvium with shallow seismic reflections: Geophysics, **54**, 1528–1534.

Miller, R. D., and J. Xia, 1998, Large near-surface velocity gradients on shallow seismic reflection data: Geophysics, **63**, 1348–1356.

Miller, R. D., J. Xia, R. S. Harding, J. T. N. nad J[] W[] Fairborn, and D. W. Steeples, 1995, Seismic investigation of a surface collapse feature at Weeks Island Salt Dome, Louisiana: Geosciences, **2**, 104–112.

Müller, T., 1999, The Common Reflection Surface Stack Method – Seismic imaging without explicit knowledge of the velocity model: PhD thesis, University of Karlsruhe.

Near Surface Geophysics, 2009, Special topic: Hydrogeophysics - methods and processes: Near Surface Geophysics, **7**, 303–659.

Neidell, N. S., and M. T. Taner, 1971, Semblance and other coherency measures for multichannel data: Geophysics, **36**, 482–497.

Pakiser, L. C., and D. R. Mabey, 1954, Mapping shallow horizons with reflection seismograph: Science, **119**, 740.

Pakiser, L. C., and R. E. Warrick, 1956, A preliminary evaluation of the shallow reflection seismograph: Geophysics, **21**, 388–405.

Pasasa, L., F. Wenzel, and P. Zhao, 1998, Prestack Kirchhoff depth migration of shallow seismic data: Geophysics, **63**, 1241–1247.

Perroud, H., and M. Tygel, 2004, Nonstretch NMO: Geophysics, **69**, 599–607.

———, 2005, Velocity estimation by the common-reflection-surface (CRS) method: Using ground-penetrating radar data: Geophysics, **70**, B43–B52.

Polom, U., L. Hansen, G. Sauvin, J. S. L'Heureux, I. Lecomte, C. M. Krawczyk, M. Vanneste, and O. Longva, 2010, High resolution SH-wave seismic reflection for characterization of onshore ground conditions in the Trondheim harbor, central Norway, *in* Miller, R. D., J. D. Bradford, and K. Holliger, eds., Advances in Near-Surface

Seismology and Ground-Penetrating Radar: Society of Exploration Geophysicists, 75–92.

Pugin, A. J. M., J. A. Hunter, D. Motazedian, and K. K. Banab, 2007, An Application of Shear Wave Reflection Landstreamer Technology to Soil Response Evaluation of Earthquake Shaking in an Urban Area, Ottawa, Ontario: 20th Annual Symposium on the Application of Geophysics to Engineering and Environmental Problems, SAGEEP, 885–896.

Pugin, A. J. M., T. H. Larson, S. L. Sargent, J. H. McBride, and C. E. Bexfield, 2004, Near-surface mapping using SH-wave and P-wave seismic land-streamer data acquisition in Illinois, U.S.: The Leading Edge, **23**, 677–682.

Pugin, A. J. M., S. E. Pullan, J. A. Hunter, and G. A. Oldenborger, 2009, Hydrogeological prospecting using P- and S-wave landstreamer seismic reflection methods: Near Surface Geophysics, **7**, 315–327.

Pugin, A. J. M., S. L. Sargent, and L. Hunt, 2006, SH- and P- Wave Seismic Reflection Using Landstreamers to Map Shallow Features and Porosity Characteristics in Illinois: 19th Annual Symposium on the Application of Geophysics to Engineering and Environmental Problems, SAGEEP, 1094–1109.

Pullan, S. E., and J. A. Hunter, 1990, Delineation of buried bedrock valleys using the optimum-offset shallow seismic reflection technique, *in* Ward, S., ed., Geotechnical and Environmental Geophysics, Volume III: Geotechnical: Society of Exploration Geophysicists, 89–97.

Robertsson, J. O. A., K. Holliger, and A. G. Green, 1996a, Source-generated noise in shallow seismic data: European Journal of Environment Engineering Geophysics, **1**, 107–124.

Robertsson, J. O. A., K. Holliger, A. G. Green, A. J. M. Pugin, and R. D. Iaco, 1996b, Effects of near-surface waveguides on shallow high-resolution seismic refraction and reflection data: Geophysical Research Letters, **23**, 495–498.

Ronen, J., and J. F. Claerbout, 1985, Surface-consistent residual statics estimation by stack-power maximization: Geophysics, **50**, 2759–2767.

Roth, M., K. Holliger, and A. G. Green, 1996, Guided waves in near-surface seismic surveys: Geophysical Research Letters, **25**, 1071–1074.

Rothman, D. H., 1986, Automatic estimation of large residual statics corrections: Geophysics, **51**, 332–346.

Ruskey, F., 1981, High-resolution seismic methods for hard-rock mining: Information Circular 8891, U.S. Bureau of Mines, 4–28.

Sambuelli, L., G. P. Deidda, G. Albis, E. Giorcelli, and G. Tristano, 2001, Comparison of standard horizontal geophones and newly designed horizontal detectors: Geophysics, **66**, 1827–1837.

Schepers, R., 1975, A seismic reflection method for solving engineering problems: Journal of Geophysics, **41**, 367–384.

Schmeissner, C., K. T. Spikes, and D. W. Steeples, 2001, Recording seismic reflections using rigidly interconnected geophones: Geophysics, **66**, 1838–1842.

Sheriff, R. E., 2002, Encyclopedic Dictionary of Applied Geophysics: Society of Exploration Geophysicists, Fourth Edition.

Sloan, S. D., D. W. Steeples, and G. P. Tsoflias, 2009, Ultra-shallow imaging using 3D seismic reflection methods: Near Surface Geophysics, **7**, 307–314.

Steeples, D. W., 1984, High-resolution seismic reflections at 200 Hz: Oil and Gas Journal, **82**, 86–92.

———, 1998, Special Issue - Shallow seismic reflection section–Introduction: Geophysics, **63**, 1210–1212.

Steeples, D. W., G. S. Baker, and C. Schmiessner, 1999, Toward the autojuggie: Planting 72 geophones in 2 sec: Geophysical Research Letters, **26**, 1085–1088.

Steeples, D. W., A. G. Green, T. V. McEvilly, R. D. Miller, W. E. Doll, and J. W. Rector, 1997, A workshop examination of shallow seismic reflection surveying: The Leading Edge, **16**, 1641–1647.

Steeples, D. W., and R. W. Knapp, 1982, Reflections from 25 feet or less: 52th Annual International Meeting, SEG, Expanded Abstracts, 469–471.

Steeples, D. W., R. W. Knapp, and C. D. McElwee, 1986, Seismic reflection investigations of sinkholes beneath Interstate Highway 70 in Kansas: Geophysics, **51**, 295–301.

Steeples, D. W., B. MacY, C. Schmeissner, and R. D. Miller, 1995, Contrasting near-surface and classical seismology: The Leading Edge, **14**, 271–272.

Steeples, D. W., and R. D. Miller, 1998, Avoiding pitfalls in shallow seismic reflection surveys: Geophysics, **63**, 1213–1224.

———, 2007, Two Decades of Near-Surface Seismology Progress: 20th Annual Symposium on the Application of Geophysics to Engineering and Environmental Problems, SAGEEP, 299–309.

Stockwell, J. W., 1997, Free software in education: A case study of CWP/SU: Seismic Unix: The Leading Edge, **16**, 1045–1049.

Taner, M. T., and F. Koehler, 1969, Velocity spectra - Digital computer derivation and applications of velocity functions: Geophysics, **34**, 859–881.

Taner, M. T., F. Koehler, and K. A. Alhilali, 1974, Estimation and correction of near-surface time anomalies: Geophysics, **39**, 441–463.

The Leading Edge, 2009, Special section - hydrogeophysics: The Leading Edge, **28**, 1210–1265.

———, 2011, Special section - near-surface geophysics: The Leading Edge, **30**, 138–204.

———, 2012, Special section - near-surface measurements in exploration geophysics: The Leading Edge, **31**, 32–88.

———, 2013, Special section - urban geophysics: The Leading Edge, **32**, 248–322.

Treadway, J. A., D. W. Steeples, and R. D. Miller, 1988, Shallow seismic study of fault scarp near Borah Peak, Idaho: Journal of Geophysical Research, **93**, 6325–6337.

van der Veen, M., H. A. Buness, F. Büker, and A. G. Green, 2000, Field comparison of high-frequency seismic sources for imaging shallow (10-250 m) structures: Journal of Environmental and Engineering Geophysics, **5**, 39–56.

van der Veen, M., and A. G. Green, 1998, Land streamer for shallow seismic data acquisition: Evaluation of gimbal-mounted geophones: Geophysics, **63**, 1408–1413.

van der Veen, M., R. Spitzer, A. G. Green, and P. Wild, 2001, Design and application of a towed land-streamer system for cost-effective 2-D and pseudo 3-D shallow seismic data acquisition: Geophysics, **66**, 482–500.

Warrick, R. E., and J. D. Winslow, 1960, Application of seismic methods to a ground-water problem in northeastern Ohio: Geophysics, **25**, 505–519.

Widess, M. B., 1973, How thin is a thin bed: Geophysics, **38**, 1176–1254.

Wiggins, R. A., K. L. Larner, and R. D. Wisecup, 1976, Residual statics analysis as a general linear inverse problem: Geophysics, **41**, 922–938.

Woorely, E. W., R. L. Street, Z. Wang, and J. B. Harris, 1993, Near-surface deformation in the New Madrid seismic zone as imaged by high resolution SH-wave seismic methods: Geophysical Research Letters, **20**, 1615–1618.

Yilmaz, O., 1987, Seismic Data Analysis: Society of Exploration Geophysicists.

Zhang, B., K. Zhang, S. Guo, and K. Marfurt, 2013, Nonstretching NMO correction of prestack time-migrated gathers using a matching-pursuit algorithm: Geophysics, **78**, U9–U18.

Ziolkowski, A., and W. E. Lerwill, 1979, A simple approach to high resolution seismic profiling for coal: Geophysical Prospecting, **27**, 360–393.